Dynamic analysis of an optical MEMS device

Mark W. Carey

A thesis submitted in partial fulfilment
of the requirements for the degree of
Master of Engineering
in
Mechanical Engineering
at the
University of Canterbury,
Christchurch, New Zealand.

14 November 2003

Acknowledgements

When looking back over the year and a half of my life that this work (now consigned to this tome) has occupied I am compelled to stop, and thank those who have made this possible. Work, as part of life, cannot occur in a vacuum.

Firstly to Mother and Father, thank you for giving me the genes that make me a why child and as I grew fostering that attitude in me, I know I have subsequently referred to such children as "terror kiddies", I now see that life has spaces for such pesonalities, even though some of us never quite loose the "terror" bit. Thank you for your words of encouragment and wisdom. Thank you also for the financial support, through undergraduate studies and gaps in postgraduate life.

Hannah, as this stage in life draws to a close, another one dawns, I know you'll be there beside me whatever that means. Together on a journey, companions on the road. We'll reflect on this bit and what from it arose.

To my flatmates during my postgraduate years: Adrian, Amanda, Dave, Jayne, Kev, and Steve thank you for putting up with arrivals home late at night and departures (mostly) in the early hours of the morning and other associated weird antics. Special thanks to Dave for his insights into the world of structural engineering, the animal noises at the door and for sharing the load of everyday life.

Carmen, Jonathan and Kate, thank you for being awesome office buddies, for the birthday surprises, trips to the pub and conversations on obscure topics. Carmen and Kate thank you especially for the use of your computers, you will get the disk space back shortly.

Athol, thank you for introducing me to Geir, Hybrids and Newmark, without them I would still be writing code. Thank you also for supplying some of the inner workings of RUAUMOKO and your other insights into the world of finite element analysis, both static and dynamic.

Geoff, another stand of fit healthy red pens laid bare, another thesis to add

to the collection of fodder for bright eyed newcomers. After all your waiting you finally get to see your plots, I hope they show enough interesting stuff. Thank you for not always telling me what I wanted to hear. Thank you for your patience through long periods of debugging as additional “features” were removed. Thank you for organising the research and the funding on which it operated.

Marek, John and Dick thank you for taking a gamble on me with this reserach, for the technical information and direction you have supplied. I hope you have found what it was you were looking for.

Contents

1. Introduction **1**
1.1. Why model MEMS 2
1.2. Optical switching micro-devices 4
1.2.1. Digital Micromirror Device 4
1.2.2. Grating Light Valve 5
1.3. Grating Electro Mechanical Systems 6
1.4. Modelling approach 9

2. Critical Dynamics, Finite Element Formulation and Numerical Solution **13**
2.1. System representation 13
2.1.1. Hybrid stress element formulation 14
2.1.2. Initial material stress 18
2.1.2.1. Additional bending stiffness 18
2.1.2.2. Initial membrane tensile forces 19
2.2. Modal analysis 20
2.3. Numerical Integration Method 21
2.3.1. Equilibrium 22
2.4. Large deflection 24
2.5. Electrostatic loading 25
2.5.1. Bifurcation 28
2.6. Contact 30
2.7. Opto–mechanical coupling 33

3. Implementation **35**
3.1. Multilayer approximation 35
3.1.1. Equivalent thickness 37
3.1.2. Equivalent density 38
3.1.3. Equivalent initial stress 38
3.2. Symmetric model reduction 38
3.3. Stress calculation 39

4. Model Verification **43**
4.1. Felippa cantilever 43
4.2. Model structure 45
4.3. Fixed-fixed beam comparison 46
4.4. Dynamics comparison 47
4.4.1. Modal analysis 47
4.4.2. Dynamic analysis 48
4.5. Quasi–static static limit comparison 50

5. Trade-off Analyses **53**
5.1. Reference ribbon unit configuration 54
5.2. Slew rate 63
5.3. Initial material stress 69
5.4. Ribbon thickness 74
5.5. Standoff design 81
5.5.1. Standoff layout 81
5.5.1.1. Variation across the ribbon width (s_y) 81
5.5.1.2. Variation along the ribbon length (s_x) 87
5.5.2. Standoff height 91

6. Conclusions **97**
6.1. Future work 99

References **100**

A. ANSYS validation code **105**
A.1. Modeshapes and frequencies 105
A.2. Dynamics 107

B. Simulation Process **111**
B.1. Simulation process 111
B.1.1. Running a simulation 111
B.2. Analysing results 112
B.2.1. Information 112
B.2.2. Plots 112
B.2.3. Movies 112

C. Simulation runtimes **113**

List of Figures

1.1. Device performance, indicating failure 2
1.2. Parameter variations on performance characteristics 4
1.3. Texas instruments DMD 5
1.4. Silicon light machines GLV 6
1.5. Schematic GEMS layout 7
1.6. Single GEMS ribbon unit 8

2.1. Degree of freedom definition 14
2.2. Complimentary energy definition 15
2.3. Linear system force deflection relationship 22
2.4. Non–linear system force deflection relationship 23
2.5. Problematic system force deflection relationships 24
2.6. Large deflection elemental transformations 25
2.7. Parallel plate capacitor definition 27
2.8. Parallel plate force (p_z) variation with applied voltage (V) and electrode deflection (v_z) 28
2.9. Finite element mesh of stable structural states 29

3.1. Implementation framework 36
3.2. Structural ribbon cross section approximation (exaggerated vertical scale) 37
3.3. Single layer structure stress distributions 40
3.4. Composite structure stress distributions 41

4.1. Deformed Felippa cantilever, illustrating bending stress contours 43
4.2. Model structure for code verification 45

4.3. Fixed-fixed beam deflection comparison 47
4.4. Model structure undamped dynamic mode shapes 1–8 49
4.5. Model structure dynamics comparisons ($\sigma_0 = 0$) 50
4.6. Model structure profile comparisons 51
4.7. Test structure, quasi-static hysteresis comparisons 51

5.1. Reference ribbon unit layout 54
5.2. GEMS ribbon unit model mesh densities, showing node numbers 56
5.3. Reference simulation electro-mechanical hysteresis trace 58
5.4. Reference simulation runtime profile 59
5.5. Reference simulation diffractive efficiencies 61
5.6. Reference simulation diffractive efficiency details 62
5.7. Slew rate simulation voltage profiles 63
5.8. Hysteresis curves for slew rate simulations 64
5.9. Slew rate simulation time deflection profiles (Legend as in Figure 5.8) 65
5.10. Slew rate simulation runtime profiles 67
5.11. Fundamental frequency variation with initial material stress 69
5.12. Hysteresis curves for initial material stress simulations 70
5.13. Initial material stress simulation runtime profiles 72
5.14. Fundamental frequency variation with silicon nitride thickness 75
5.15. Hysteresis curves for thickness simulations 76
5.16. 50nm Silicon Nitride thickness simulation ribbon unit positions showing substrate contact 77
5.17. Silicon nitride thickness runtime profiles 79
5.18. $t_{Si_3N_4} = 50$nm ribbon unit showing oxide contact 80
5.19. Ribbon profiles ($x = 15$µm) for s_y simulations 82
5.20. Hysteresis curves for s_y simulations 83
5.21. Standoff layout (s_y) simulation runtime profiles 85
5.22. $s_y = 0$µm ribbon unit showing oxide contact 86
5.23. Ribbon profiles ($y = 4$µm) for s_x simulations 88
5.24. Hysteresis curves for s_x simulations 89
5.25. Standoff layout (s_x) simulation runtime profiles 90

5.26. $s_x = 8\mu m$ deformed ribbon unit showing oxide layer contact, simulation step 32000 91

5.27. Hysteresis curves for standoff height simulations 92

5.28. Standoff height simulation runtime profiles 93

5.29. $t_{Standoffs} = 0.02\mu m (40\%)$ deformed ribbon showing oxide layer contact, simulation step 44000 94

B.1. Simulation control dialog 111

List of Tables

4.1. Fellipa Cantilever test deflection results 44

4.2. RUAUMOKO Fellipa Cantilever test deflection results 44

4.3. Model structure parameters 45

4.4. Fixed-fixed beam deflection results 46

4.5. Model structure and ANSYS natural frequencies 48

4.6. Critical voltage comparison 52

5.1. Reference ribbon unit parameters 55

5.2. Reference structure natural frequencies 57

5.3. Critical voltages for reference simulation 58

5.4. Critical voltages for slew rate simulations 66

5.5. Minimum electrode separations for slew rate simulations 68

5.6. Critical voltages for initial material stress simulations 71

5.7. Minimum electrode separations for initial stress simulations 73

5.8. Critical voltages for thickness simulations 76

5.9. Minimum electrode separations for thickness simulations 80

5.10. Critical voltages for s_y simulations 84

5.11. Minimum electrode separations for s_y simulations 86

5.12. Critical voltages for s_x simulations 88

5.13. Minimum electrode separations for s_x simulations 90

5.14. Critical voltages for standoff height simulations 93

5.15. Minimum electrode separations for standoff height simulations 94

C.1. Simulation computational requirements 114

Abstract

This thesis formulates, implements and validates an integrated framework for analysing Micro-Electro-Mechanical-Systems (MEMS) devices including non-linear electrostatic loading, large deflections, structural contact and dynamic behaviours. Utilizing the framework developed enables the simulation of electrostaticallly actuated thin film bifurcating MEMS devices, with specific application to Eastman Kodak's conformal Grating Electro Mechanical System (GEMS) device.

The resulting tool provides insight into the dynamic operation of MEMS devices allowing an assessment of the impact of variations in device design and fabrication on the dynamic response of such structures. The data obtained also allows the postponement of expensive prototype fabrication and provides a validated foundation upon which future studies can be conducted.

Simulating perturbations in key device parameters for the GEMS device illuminates the edges of the feasible design space for that device. The results obtained clearly illustrate the inadequacies of modelling techniques that neglect the distributed nature of the structural problem, or the dynamics of the system. The thesis concludes with a discussion of salient results noting future avenues for research and development.

Chapter 1

Introduction

This thesis concentrates on developing, implementing, testing and utilizing numerical models for the efficient simulation of Micro-Electro-Mechanical-Systems (MEMS), enabling enhancements in operating lifetime, diagnosis of fabrication problems and optimization of structural performance.

In particular the effects, of manufacturing process variability on device performance is crucial as arrays of such structures are batch fabricated. Variations in structural performance arising from process variability must be minimized to ensure consistent device operation across the elements of an array. Due to the size of such devices, typical dimensions on the order of 0.1-10μm, tiny variations in device parameters can cause significant changes in performance, easily accounting for order of magnitude changes in operating characteristics. Simulating variations in parameters allows an assessment of the sensitivity of device performance.

The device of interest is the Grating Electro Mechanical System (GEMS) device developed by the Eastman Kodak Company for high speed digital light switching applications. The models created must provide understanding of device performance beyond what is currently available through the inclusion of specific physical phenomena. The modelling approach adopted should also allow for future analysis of the interaction between material layers, the inclusion of non-linear damping and possible failure mechanisms.

The scope of the research is not limited to the development of a model for a single type of device. Instead, the development of a general framework for capturing the operating dynamics of MEMS structures subject to time varying electrostatic loads is presented. These structures are also under the influence of initial material stresses and contact other structural bodies during normal operation.

1.1. Why model MEMS

MEMS devices are typically designed around unique structural characteristics. The GEMS device exhibits classical electromechanical hysteresis, as illustrated in Figure 5 of Kowarz [2001] and Figure 4 of Furlani et al. [1998]. Electromechanical hysteresis is also observed in the response of other common MEMS devices [Artz and Cathey, 1992; Gilbert et al., 1996]. The reliability of the device is often inextricably linked to the consistent reproduction of such behaviours across all devices.

Figure 1.1 depicts an electro-mechanical hysteresis response. Where the voltage applied to the structure is increased, the structure deforms until the applied electrostatic load overwhelms the restoring ability of the structure and significant deflections are realised for small changes in voltage. Reducing the applied voltage has little immediate effect as the electrostatic force on the structure is proportional to the inverse of deflection squared. The structure remains in the deformed configuration until the electrostatic force is reduced enough to allow the stiffness of the device to snap the structure back toward the undeformed configuration.

PSfrag replacements

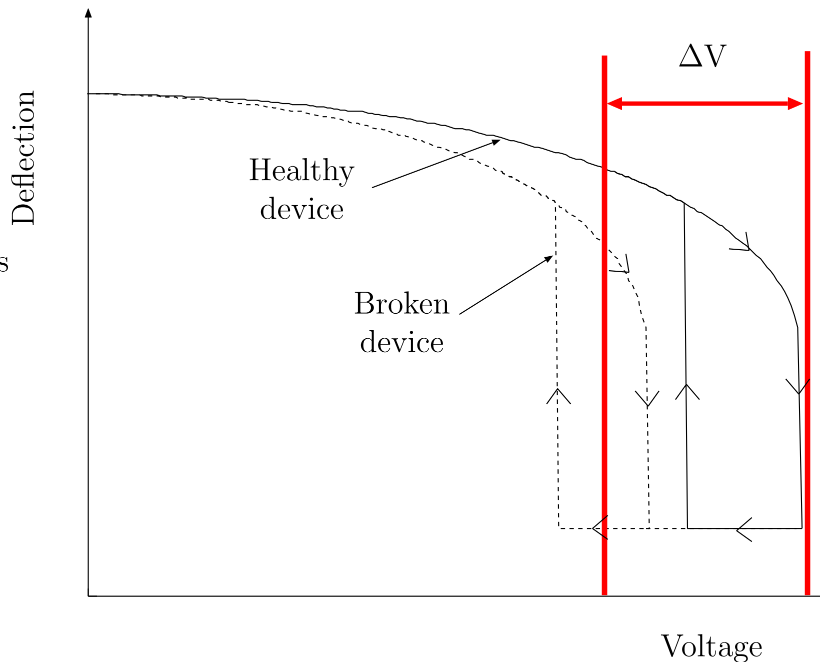

Figure 1.1. Device performance, indicating failure

Typically, such devices are held at a base voltage and a switching voltage (ΔV) is applied to drive the change of state. If a second device in the same

array exhibits the response illustrated by the dashed line in Figure 1.1, then applying the same base and switching voltages causes the second device to switch to the deformed configuration. However, this second device will not return to the undeformed configuration because the voltage is never low enough to allow the return change of state. Such inconsistencies across arrays of devices causes individual elements to function contrary to specification, appearing broken. This type of variation can occur due to fabrication process variations.

MEMS devices are manufactured (fabricated) using processes similar to those commonly used in the manufacture of integrated circuits and semi-conductors. These processes are characterised by the four fundamental steps: deposit, mask, expose and etch [Madou, 1997]. More specifically a layer of material is deposited on a substrate and masked according to the desired features. It is then exposed to an energy source changing the properties of the exposed regions, and then washed with chemical etchant to remove unexposed areas. Devices are fabricated in an additive fashion from the base upwards.

Due to the nature of the processes employed, arrays of devices are batch fabricated on wafers to reduce material handling and production costs. However, due to variations in the deposition, exposure and etching processes variations in dimensions may occur across an array of devices fabricated adjacent to each other. The observation of the resulting performance variations in manufactured devices has led to the cultivation of the concept that the mechanics of micro-devices differs from mechanics at larger scales.

It is important to ensure that the manufacturing processes employed in device fabrication are capable of producing devices that operate with the desired performance characteristics. Example of such an analysis is presented in Figure 6 of Douglass [2003] and Figures 5 & 6 of Meier [1998]. Figure 1.2 illustrates a generalization of the effect. The shaded region in Figure 1.2 depicts the desired performance region, the crosses represent the performance of fabricated devices as a function of some parameter of the manufacturing process. The figure indicates that the adopted manufacturing process produces devices that operate with undesirable performance characteristics, the thin oval line. Thus, tighter control over the manufacturing process is required to restrict the process variability to the thick, red oval, resulting in all fabricated devices performing as desired.

When such variations occur across the elements in an array, the resulting performance variability unnecessarily complicates control electronics, resulting in increased cost to the consumer, if not an infeasible design. Comparative modelling

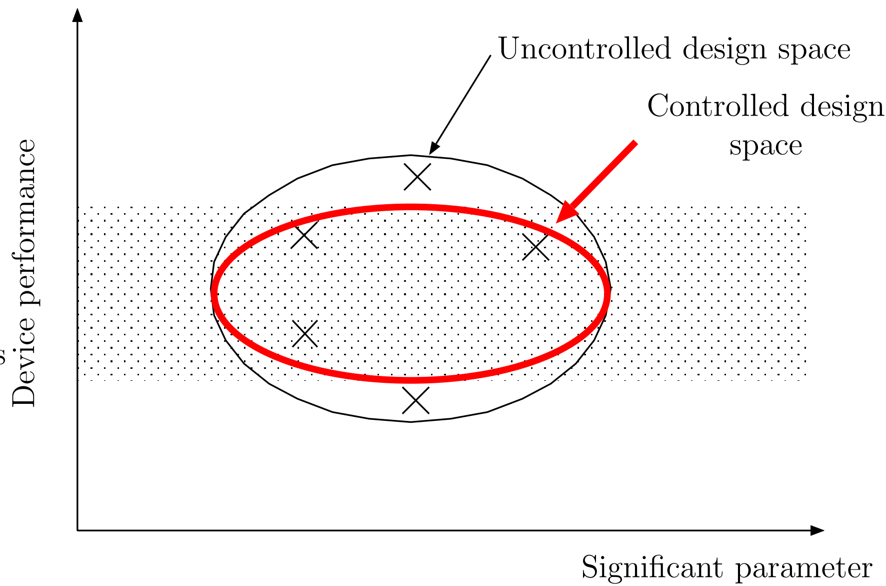

Figure 1.2. Parameter variations on performance characteristics

allows different device designs to be benchmarked, allowing the costly one off fabrication of prototypes to be delayed until a workable device has been throughly modelled and the complexities of the design space fully grasped. Delaying prototyping reduces device design costs and design time, lowering one of the barriers to broad adoption of MEMS technology.

1.2. Optical switching micro-devices

Currently two types of optical switching micro-devices have found application in off the shelf products: The two devices are the Texas Instruments Digital Micromirror Device and the Silicon Light Machines Grating Light Valve.

1.2.1. Digital Micromirror Device

Developed from the work of Dr. Larry J. Hornbeck in 1987 the Texas Instruments Digital Micromirror Device (DMD) was first demonstrated publicly in 1994 and consists of a planar reflective surface, which is rotated causing incident light to be reflected in a specified direction. Figure 1.3 illustrates two DMD pixels, one on and the other off. A notable feature of the DMD is the small spring tips placed at the outer edges of the rotational yokes, these spring tips limit the

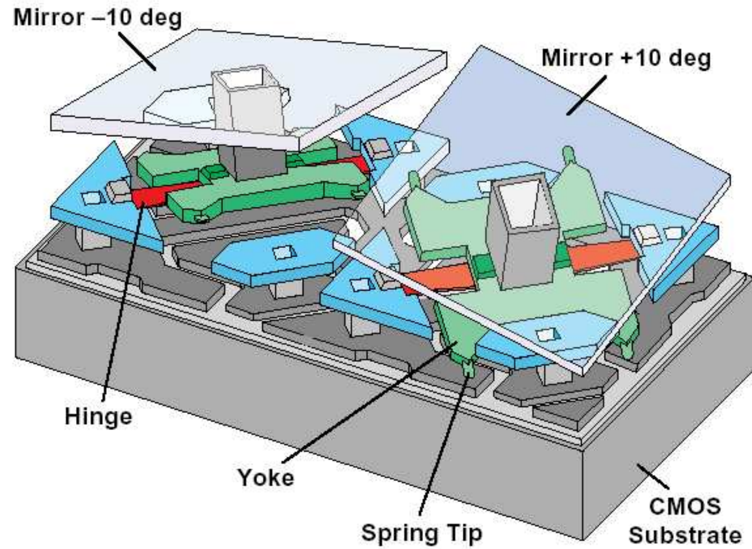

Figure 1.3. Texas instruments DMD

occurrence of structural contact, lessening the likelihood of device failure due to friction (stiction). DMD devices offer excellent contrast control as the mirror can be torsionally balanced if operated in an analogue fashion. The drawback of this feature is the devices operate slowly, enabling only kilohertz (kHz) switching speeds. Publicly available literature suggests current DMD devices operate in a digital fashion with pixel response time of 10µs [Younse, 1993], which controls the intensity of the light reflected by the pixel. The DMD device operates on the principal of reflection requiring large structural deformations, as Figure 1.3 indicates ±10°. The device layout also illustrates the complexity and many steps required in the manufacturing process.

1.2.2. Grating Light Valve

Descended from the work of Olav Solgaard, [Solgaard, 1992], the Grating Light Valve (GLV) [Bloom et al., 1994] shares a common ancestry with the Grating Electro Mechanical System. Consisting of beam like elements suspended above a subsurface cavity, a diffraction pattern is formed in the light reflected from the device when operated in an arrayed configuration [Bloom et al., 1994]. Reflection away from the light source is also possible when implemented in a torsional configuration as illustrated in Figure 8 of Bloom et al. [1994]. Figure 1.4 shows six

GLV beams in varying states, operating in a diffractive configuration. As with the DMD the GLV can be operated in a digital or analogue fashion depending on the desired application, but is currently utilized in an analogue fashion to output multiple shades of grey. Early GLV devices were 1-2μm in width and

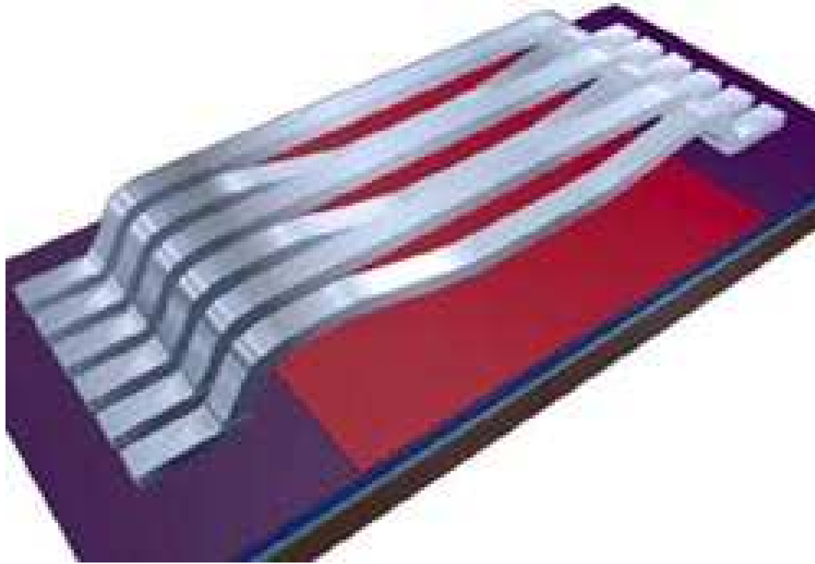

Figure 1.4. Silicon light machines GLV

approximately 220nm thick, consisting of an upper reflective Aluminium layer that provides the optical properties while the lower Silicon Nitride ceramic layer provides the structural characteristics of the device. This narrow cross section places tight tolerances on the location of related optical equipment.

GLV devices typically have natural frequencies in the range of 1 Megahertz (MHz) to approximately 6 MHz. The natural frequency of the device is controlled by altering the length of the device, from 120μm to 40μm for published data. Bloom et al. [1994] does not indicate a method for obviating the effects of stiction between the movable and stationary structural elements, however later patents by the same author indicate a method for adressing the effects of structural contact. The small width of the GLV makes it highly susceptible to fabrication variations.

1.3. Grating Electro Mechanical Systems

Grating Electro Mechanical Systems (GEMS) [Kowarz et al., 2002] are a Kodak patented [Jech et al., 2001; Kowarz, 2001] optical MEMS device containing an

array of electrostatically actuated diffraction gratings. Similar devices are presented by Apte [1994]; Solgaard [1992] and Solgaard et al. [1992]. The GEMS device is designed to be used in an arrayed configuration as a high speed digital light switch, with potential applications ranging from data projection to optical switching in telecommunications and networking, to digital printing.

The GEMS structure consists of composite ribbons suspended above a silicon substrate by a series of intermediate supports. The composite nature of the ribbon allows the use of ceramic materials which provide enhanced structural performance over the Aluminium electrode in addition to electrical isolation. When actuated, the ribbons conform to the underlying support structure or "standoffs" as shown in Figure 1.5, to produce a grating. The intermediate supports, have a periodic spacing (Λ), which is concealed beneath the ribbons. A single pixel in a linear array typically has one or more suspended ribbons, each attached to several intermediate supports. There is no requirement on the number of ribbons or intermediate supports per pixel. Figure 1.5, adapted from Jech et al. [2001], shows a schematic layout of a GEMS structure, where the vertical dimensions (z) have been scaled significantly for illustrative purposes.

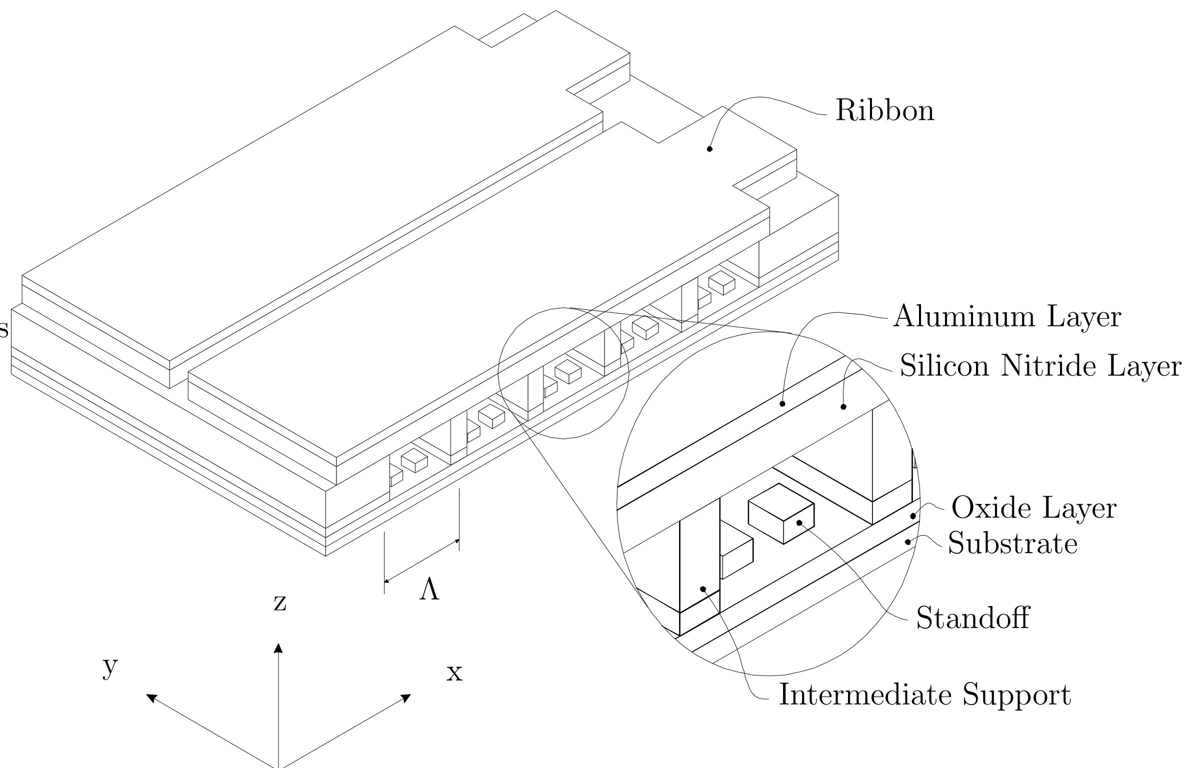

Figure 1.5. Schematic GEMS layout

Like the spring tips in the DMD, the standoffs beneath the GEMS ribbon are included to obviate stiction by minimizing the area of structural contact. Without such structures it is possible, when drying the devices after releasing the ribbon elements, that the ribbon conform to the underlying structural features, remaining held in place by Van der Waals forces [Solgaard, 1992]. However, Kodak addresses the stiction on release issue by adopting a dry etch process for the release step of fabrication. In addition, excessive structural contact during operation can cause device failure as frictional forces overcome the restoring ability of the device, resulting in a failed device. This group of failure mechanisms is losely termed “stiction” [Madou, 1997].

A representative GEMS ribbon unit is 30µm long (x) 6µm wide (y) and 150nm thick (z), wider and thinner than the GLV. The Silicon Nitride layer is 100nm thick and the Aluminium layer is 50nm thick. The natural frequency of such a device is 9MHz, greater than the 6.1MHz of the GLV. A switching speed of less than 50ns is therefore attained, which is three orders of magnitude faster than the DMD. The GEMS ribbon unit can be operated in either an analogue or digital manner.

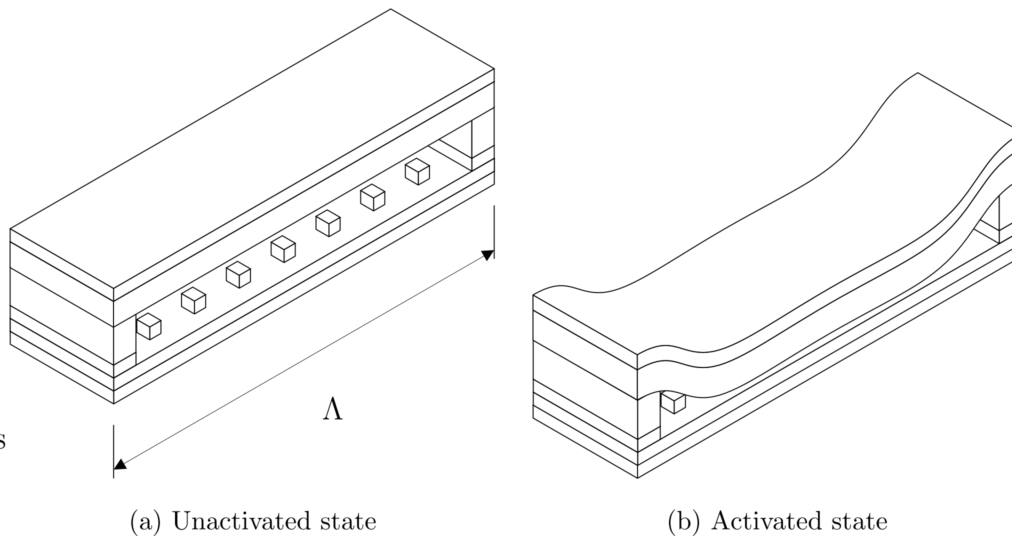

(a) Unactivated state

(b) Activated state

Figure 1.6. Single GEMS ribbon unit

A single GEMS ribbon may consist of an arbitrary number of identical repeating units. Thus, computational efficiencies may be leveraged by modelling only the base repeating unit. If the fluidic or electrostatic interactions between neighbouring units are of interest, single unit models may be coupled to model a larger

portion of the complete system. Hence, the need for a robust modelling framework that allows a variety of dynamic effects to be added as necessary. Figure 1.6 shows a single unit from a GEMS ribbon, in both the unactivated, Figure 1.6(a), and activated, Figure 1.6(b), states with vertical dimensions magnified. This thesis focuses on modelling the dynamics of a single GEMS unit within an integrated framework, allowing interaction simulations to be performed at a later date.

1.4. Modelling approach

There are three common approaches to modelling thin, non-linear structures such as the GEMS device:

1. Reduced order models
2. String models
3. Finite element models

Reduced order modeling is a popular approach often utilising a single parameter model of the structural system and a second parameter for the electrostatic system [Chen and Kang, 2000; Osterberg et al., 1994b; Senturia et al., 1997]. Such models, while excellent for global system simulation where the structure's interaction in a larger system is of interest, negate the distributed nature of the structural system, severely limiting the structural detail available in simulation results.

A second approach at reduced order modelling represents the dynamic deformation of the structure in terms of modal contributions from participating dynamic modes of operation to represent the deformation of the structure. Commonly used in MEMS analysis, and specifically with the ANSYS package, this approach requires the inclusion of an extreme number of modes to accurately capture the dynamics of the GEMS ribbon unit as the structural deformation around the standoffs requires a large number of modeshapes to be accurately captured. Modal analysis methods also assume small deflection linear behaviour and damping models that are modally decoupled, neither of which may be completely realistic for electrostatically actuated ribbons.

Thin structures can also be modelled as string structures [Kowarz et al., 2002] since membrane tensile forces often dominate structural stiffness and the mass of the structure is low due to small thickness. Hence, the structural response is

assumed to be dominated by the membrane forces, so these models include only axial tensile terms ignoring the effects of structural bending contributions. While easy to model using analytical techniques, string idealizations do not allow the modelling of points of zero rotation, making commonly used fixed end conditions difficult to capture. While string models do accurately capture behaviours along the most significant structural dimension, they neglect deformation across the structure, which can be critical.

A finite element approach to modelling the structure allows simple modification of material and geometric parameters without requiring changes in the fundamental solution, as is the case in analytical approaches. A finite element approach also provides distributed structural information and a discretization ready for use in electrostatic force computation. A number of specialised software solutions based on existing finite element solutions currently exist for solving coupled electrostatic structural problems. The most common approach couples the publicly available capacitance solver FastCap [Nabors and White, 1991] with a reputable structural solver, using custom software to act as an intermediary between the separate packages. In most published cases Abaqus is the structural analysis software of choice [Gilbert et al., 1996; He et al., 1998; Osterberg et al., 1994a].

The primary concern when selecting an existing off the shelf package for dynamic simulation of MEMS devices, is that it accurately incorporates all the necessary phenomena into a single cohesive framework. For the GEMS device such a framework must include time varying dynamics, electrostatic loading, structural contact and non-linear material behaviours. No package currently available encompasses all these basic phenomena in a framework sufficient for this study.

A less common approaches to modelling thin non-linear structures uses boundary element models, which are not commonly used in structural mechanics as the displacement solution is required throughout the structure of interest and not just at the boundaries. However, boundary element techniques are commonly used in the computation of electrostatic forces on arbitrary conductors as in FastCap [Nabors and White, 1991]. Furlani et al. [1998] presents a method, and subsequent results, of utilizing an iterative greens function to solve for the static displacement of an electro–statically actuated thin film microbeam, ignoring the dynamics of the system.

The method developed is to utilize a finite element solution to the modelling of thin film non-linear structures. Such an approach requires a robust framework in which future additions can be included, allowing future investigators a basis from which to investigate effects such as inter-facial delamination and optical coupling. A framework based approach also allows the incorporation of novel approaches to the modelling of contact. The approach developed provides distributed structural deformation information, enhancing understanding of the operation of MEMS devices and providing a platform to determine the impact of variations in device design and fabrication, a goal of this thesis.

Chapter 2

Critical Dynamics, Finite Element Formulation and Numerical Solution

This chapter presents the system dynamics, the finite element formulation needed to capture these dynamics and the numerical solution procedure utilized to solve the resulting non-linear system of equations. It also discusses the critical dynamics of contact, electrostatic loading and non-linear bifurcation.

The dynamics of general structural systems under time varying loading may be modelled using the second order linear ordinary differential equation,

$$[M]\{\ddot{v}\} + [C]\{\dot{v}\} + [K]\{v\} = \{p\} \tag{2.1}$$

Where $[M]$, $[C]$ and $[K]$ represent the mass, damping and stiffness matrices of the system respectively, $\{v\}$ is the deflection column vector, the dot notation denotes derivatives with respect to time, and $\{p\}$ is the time varying applied load.

In Equation (2.1) $\{p\}$ represents the applied structural loads. For electrostatically actuated MEMS devices $\{p\}$ is a function of both deflection (v) and time (t), thus, the system described by Equation (2.1) is considered non-linear. The adopted solution strategy maintains electrostatic equlibrium to accurately capture the transient non-linear dynamics of the system.

For MEMS, the dynamics are no different to those of larger structures. Dimensions are many orders of magnitude smaller, and the dominance of different effects may vary, but the same physical laws apply.

2.1. System representation

The system stiffness matrix ($[K]$) utilises Hybrid Stress quadrilateral finite elements [Horrigmoe, 1977, 1978], for both bending (v_z, v_{θ_x}, v_{θ_y}) and membrane (v_x, v_y, v_{θ_z}) contributions. The result is a stiffness model with six degrees of freedom

per node (v_x, v_y, v_z, v_{θ_x}, v_{θ_y}, v_{θ_z}) and uncoupled bending and membrane behaviours. Hybrid stress finite elements provide efficient stiffness representations allowing accurate modelling using coarse meshes, and are commonly found in modern finite element solutions. Figure 2.1, illustrates the six degrees of freedom (DOF) per node and the 24 DOF per element. As illustrated the nodal numbering order is anticlockwise around the circumference of the element. As each

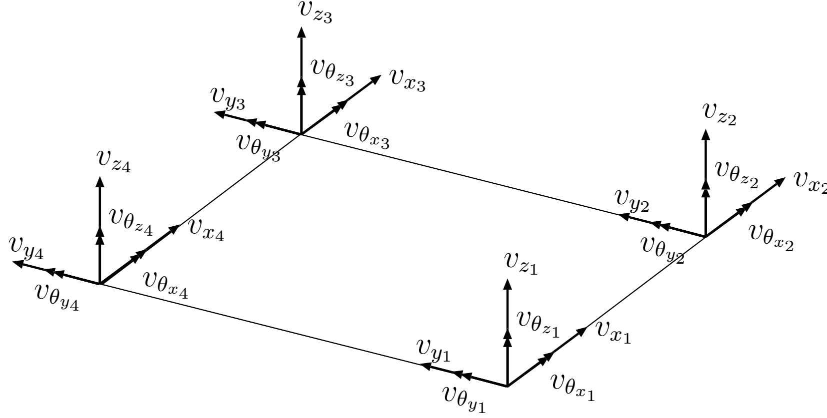

Figure 2.1. Degree of freedom definition

element contains 24 DOF the elemental matrices ($[k]$, $[m]$ and $[c]$) will be 24×24 in size.

2.1.1. Hybrid stress element formulation

The Hybrid Stress finite element formulation is based on a modified complimentary energy functional (Π_{mc_2}). Complimentary energy for a non-linear system is defined as the area between the stress strain curve and the stress axis, as shown in Figure 2.2. Typical energy based finite elements minimize the strain energy in a finite element assemblage. Hybrid elements perform this minimisation on the complimentary energy. Caution is required as Castigliano's theorem is only applicable for linear elasticity. For the hybrid stress finite elements the modification to the complimentary energy functional is the relaxation of stress continuity along the boundaries of adjacent elements. For such elements Π_{mc_2} is defined

$$\Pi_{mc_2} = \sum_n \left\{ \int_{V_n} \frac{1}{2} \{\sigma\}^T [S] \{\sigma\} \, \mathrm{d}V - \int_{\partial V_n} \{\tilde{u}\}^T \{T\} \, \mathrm{d}s \right\} + \sum_n \left\{ \int_{S_{\sigma n}} \{\tilde{u}\}^T \{\bar{T}\} \, \mathrm{d}s \right\} \quad (2.2)$$

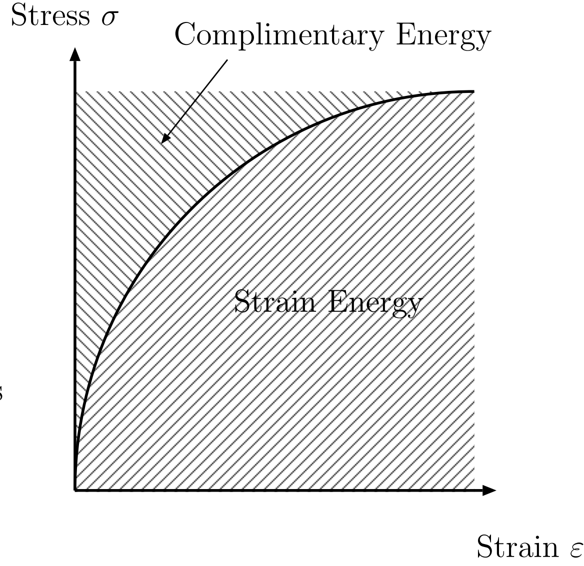

Figure 2.2. Complimentary energy definition

Where $[S]$ is the volume of the element, $\{\tilde{u}\}$ are the boundary displacements, $\{T\}$ the element boundary tractions and $\{\bar{T}\}$ the prescribed surface tractions. The stresses ($\{\sigma\}$) are interpolated in terms of a set of undetermined parameters $\{\beta\}$.

$$\{\sigma\} = [P]\{\beta\} + [P_F]\{\beta_F\} \tag{2.3}$$

Where $[P]$ and $[P_F]$ are interpolation matrices for the homogeneous and particular solution with prescribed body forces and $\{\beta\}$ and $\{\beta_F\}$ are the elemental unknowns. If $[P]$ contains $[P_F]$ then $[P_F]\{\beta_F\}$ can be omitted. If it is included, the term $[P_F]\{\beta_F\}$ resulting from initial body forces, results in extra contributions to the applied load. Omitting initial body forces, Equation (2.3) reduces to Equation (2.4).

$$\{\sigma\} = [P]\{\beta\} \tag{2.4}$$

$$\{T\} = [N]\{\sigma\} \tag{2.5}$$

$$\{\tilde{u}\} = [L]\{v\} \tag{2.6}$$

Where $[N]$ is a matrix of direction cosines and $[L]$ is an interpolation matrix relating edge deflections ($\{\tilde{u}\}$) to nodal deflections ($\{v\}$). The relaxed compatibility requirement of the hybrid stress class of finite elements requires displacement compatibility only between adjacent elements. Therefore, the following can be

defined to simplify the derivation.

$$[H] = \int_{V_n} [P]^T [S] [P] \, \mathrm{d}V \tag{2.7}$$

$$[G] = \int_{\partial V_n} [NP]^T [L] \, \mathrm{d}s \tag{2.8}$$

$$\left\{\bar{Q}_T\right\} = \int_{S_{\sigma n}} [L]^T \left\{\bar{T}\right\} \mathrm{d}s \tag{2.9}$$

Where $\left\{\bar{Q}_T\right\}$ is the consistent load vector. When Equations (2.7)-(2.9) are substituted into Equation (2.2), Π_{mc_2} reduces to:

$$\Pi_{mc_2} = \sum_n \left\{ \frac{1}{2} \{\beta\}^T [H] \{\beta\} - \{\beta\}^T [G] \{v\} + \{v\}^T \left\{\bar{Q}_T\right\} \right\} \tag{2.10}$$

Since stresses ($\{\sigma\}$) are assumed independent within individual elements, the stationary condition of the functional (Π_{mc_2}) with respect to $\{\beta\}$ can be directly obtained for each element.

$$\begin{aligned} [H] \{\beta\} - [G] \{v\} &= \{0\} \\ \{\beta\} &= [H]^{-1} [G] \{v\} \end{aligned} \tag{2.11}$$

Substituting Equation (2.11) into Equation (2.10) leaves:

$$\Pi_{mc_2} = \sum_n \left\{ -\frac{1}{2} \{v\}^T [G]^T [H]^{-1} [G] \{v\} + \{v\}^T \left\{\bar{Q}_T\right\} \right\} \tag{2.12}$$

The elemental stiffness $[k]$ can be defined:

$$[k] = [G]^T [H]^{-1} [G] \tag{2.13}$$

Thus, the stationary condition of the functional (Π_{mc_2}) with respect to deflection ($\{v\}$) is determined to be:

$$\sum_n \left([k] \{v\} - \left\{\bar{Q}_T\right\} \right) = \{0\} \tag{2.14}$$

Equation (2.14) is equivalent to the standard finite element expression,

$$\{p\} = [K] \{v\} \tag{2.15}$$

Where $\{p\}$ are the external applied loads, $[K]$ is the assembled system stiffness matrix and $\{v\}$ the associated deflections. The identical process is then repeated for the membrane degrees of freedom, resulting in an elemental stiffness representation ($[k]$) with six degrees of freedom per node and uncoupled bending and membrane behaviours.

The Adini-Clough-Melosh (ACM) [Adini and Clough, 1960; Melosh, 1961], cartesian polynomial based or the Bogner-Fox-Schmidt (BFS) [Bogner et al., 1965], hermite polynomial based finite elements are used for determining a consistent system mass representation ($[M]$) for the bending degrees of freedom and the membrane geometric contributions to bending stiffness. The ACM and BFS elements are displacement based rectangles. The Hybrid Stress element formulation is based on stress interpolations within individual elements, the displacement basis of the ACM and BFS elements allows simple calculation of geometric effects, which are more complex for the stress-based hybrids.

The contribution of membrane degrees of freedom to system mass was included using an Iso-Parametric Quadrilateral including only the v_x and v_y degrees of freedom. The v_{θ_z} degree of freedom is not included in the Iso–Parametric formulation. The resulting elemental mass matrix ($[m]$) is 24×24, however it contains one zero energy mode per node, due to this exclusion of the “screw” rotation.

The mixing of element formulations has been shown to have no negative impact on the accuracy of solutions obtained [Hinton et al., 1976; Pian, 1972]. However, static condensation is utilized to remove the screw rotation (v_{θ_z}) when computing the undamped frequencies (ω) and mode shapes ($\hat{v}$), as the resulting mass matrix does not contain contributions in this degree of freedom. This approach is commonly used in the field.

In structural mechanics, the specific mechanism causing structural damping is often unknown. However, for structures with characteristic lengths on the order of µm, the mechanism is easily identified as pressure loading due to movement through air [Keating and Ho, 2001; Naik et al., 2002]. For complex structures involving interactions from adjacent elements, determining damping effects is inherently complex requiring a solution to the Naiver Stokes equation. Some thin film structures pump fluid between the movable and stationary elements, causing non-uniform pressure gradients in arrayed configurations. For all its added complexity fluid damping is commonly simplified by modelling the fluidic effects as a lumped parameter system [Furlani, 1999; Vemuri et al., 2000]. Unless

such fluid damping can be shown to have significant impact on the dynamics of the structure of interest, Rayleigh damping can be used. Rayleigh damping is a member of the Caughey, [Caughey, 1960], family of damping models, thus the damping matrix ($[C]$) is determined from $[K]$ and $[M]$.

2.1.2. Initial material stress

Often considered a second order effect in larger structures where initial material stresses are relatively small and subsequently neglected, the contribution of in-plane initial material stresses on micro-device performance must be considered [Solgaard, 1992]. These initial stresses act to stiffen the structure in the out of plane direction [Oden, 1966; Shames and Dym, 1991]. In addition, the characteristic dimensions of MEMS structures are small, so the resulting inherent bending stiffness is also small. Hence, these stresses can dominate the inherent bending stiffness of the structure.

For the commonly used MEMS material Silicon Nitride (Si_3N_4) this initial tensile material stress can be as great as 1440MPa [Lund and Wise, 1994]. Thus, these second order effects become significant and can dominate the resulting structural bending stiffness and response. Neglecting the effect of initial material stress in MEMS devices can result in modal frequencies that are as much as an order of magnitude less than that of the actual structure. Inclusion of the initial material stresses requires two additions to the model to correctly incorporate the effects of initial material stresses on the structure:

- Additional geometric bending stiffness ($[K_g]$), incorporating membrane contribution to bending stiffness
- Initial membrane tensile forces ($\{q\}$) resulting from the initial stress

2.1.2.1. Additional bending stiffness

The additional stiffness introduced by the initial material stress ($[K_g]$) is analogous to increasing the tension on a wire line. As the tensile force increases, additional force is required to achieve a specified deflection. It is not possible to compute the additional stiffness contributions using a hybrid stress element formulation. Either the ACM [Adini and Clough, 1960; Melosh, 1961], or BFS [Bogner et al., 1965], displacement finite element formulations can be used and give very similar results. Displacement based finite elements are ideally suited

for the modelling of geometric effects as the element formulation interpolates the displacement field within the elements using differentiable polynomials. The contributions to system stiffness from the initial material stress can be calculated for each element and assembled using existing techniques.

A constant thickness ACM element has been used to determine the additional stiffness contribution.

$$[K_g] = t \int\int [A]^{-1^{\mathrm{T}}} \left\{ \frac{dw}{dx} \quad \frac{dw}{dy} \right\} \begin{bmatrix} \sigma_{xx} & \tau_{xy} \\ \tau_{yx} & \sigma_{yy} \end{bmatrix} \begin{Bmatrix} \frac{dw}{dx} \\ \frac{dw}{dy} \end{Bmatrix} [A]^{-1} \, dydx \tag{2.16}$$

Where w is the standard ACM interpolation polynomial and $[A]$ the ACM interpolation matrix, as defined on pages 596–598 of Shames and Dym [1991], t is the element thickness, and σ_{xx}, σ_{yy} and τ_{xy} are the initial membrane stress magnitudes. The additional stiffness $[K_g]$ is then included in the equilibrium equation, Equation (2.1), for use in the dynamic simulation of micro-devices.

$$[M]\{\ddot{v}\} + [C]\{\dot{v}\} + ([K] + [K_g])\{v\} = \{p\} \tag{2.17}$$

2.1.2.2. *Initial membrane tensile forces*

Initial stress effects are not included in the standard hybrid element formulation, however it is straight forward to include such effects by redefining the hybrid stress functional to account for the non-zero initial state by replacing Equation (2.4) with Equation (2.3). Completing the derivation results in an additional term (E) in the hybrid stress functional, Equation (2.12),

$$\Pi_{mc_2} = \sum_n \left\{ -\frac{1}{2}\{v\}^T [G]^T [H]^{-1} [G]\{v\} + \{v\}^T [G]^T [H]^{-1} \{E\} + \{v\}^T \{\bar{Q}_T\} \right\} \tag{2.18}$$

Where,

$$\{E\} = \int_{V_n} [P]^T [S] [P_F] \{\beta_F\} \, \mathrm{d}V \tag{2.19}$$

Assuming that the same interpolation is used for the initial forces and internal reaction forces, the nodal forces resulting from the initial material stress are

calculated:

$$\{q\} = [G]^T [H]^{-1} \{E\} \tag{2.20}$$

where $\{q\}$ can be calculated using predefined quantities in the Hybrid Stress formulation and represents the equivalent nodal forces resulting from the initial material stress. These nodal loads are added to the applied nodal loads during each time step.

Due to the lack of coupling between the bending and membrane behaviours of the elemental stiffness matrix ($[k]$), the body forces arising from the initial material stress do not effect the out of plane degrees of freedom until, the system is reassembled to account for large deflection effects. A discussion of large deflection effects can be found in Section 2.4. Both $\{q\}$ and $[K_g]$ are required to incorporate the effects of initial material stresses into the model, $\{q\}$ adds the initial material stresses to the membrane stresses arising from device operation and $[K_g]$ adds the additional stiffness resulting from the initial material stresses.

2.2. Modal analysis

The dynamic modeshapes and corresponding natural frequencies describe a set of basis vectors that can be combined to describe any deformation of the structure. They are a function of both the mass and total stiffness of the structure. The dynamic modes are calculated by assuming undamped free vibration.

$$[M]\{\ddot{v}\} + ([K] + [K_g])\{v\} = 0 \tag{2.21}$$

Solutions to Equation (2.21) are assumed to be of the form:

$$v(t) = \{\hat{v}\} \sin \omega t \tag{2.22}$$

Differentiating Equation (2.22) to obtain, $\dot{v}(t)$ and $\ddot{v}(t)$ and, substituting the results into Equation (2.21) leaves an equation in $\{\hat{v}\}$,

$$\begin{aligned} -\omega^2 [M]\{\hat{v}\} \sin \omega t + ([K] + [K_g])\{\hat{v}\} \sin \omega t &= 0 \\ \left([K] + [K_g] - \omega^2 [M]\right)\{\hat{v}\} &= 0 \end{aligned} \tag{2.23}$$

Equation (2.23) is the standard undamped structural eigen-problem used to obtain the modeshapes ($\{\hat{v}\}$) and corresponding natural frequencies (ω) of the struc-

ture.

2.3. Numerical Integration Method

The Newmark, [Newmark, 1959], family of integration schemes are implicit integration schemes that use a total or incremental form of the equation of equilibrium and assume a variation of acceleration during the time step.

$$\left[[M] + \gamma\Delta t\,[C] + \beta\,(\Delta t)^2\,[K]\right]\{\Delta\ddot{v}\} = \{\Delta p\} - [C]\{\ddot{v}_n\}\,\Delta t - [K]\left\{\{\ddot{v}_n\}\frac{(\Delta t)^2}{2} + \{\dot{v}_n\}\,\Delta t\right\} \quad (2.24)$$

Where $[M]$, $[C]$, $[K]$, $\{v\}$, $\{\dot{v}\}$, $\{\ddot{v}\}$ and $\{p\}$ are as defined in Equation (2.1), Δt is the length of the numerical time step, subscript n indicates the value at the start of the time step, and γ and β are scalar parameters defining the acceleration assumption during the time step. The two most common schemes are the linear ($\gamma = \frac{1}{2}$, $\beta = \frac{1}{6}$) and constant average acceleration ($\gamma = \frac{1}{2}$, $\beta = \frac{1}{4}$). The latter is used due to its unconditionally stable behaviour. The Newmark Constant Average Acceleration (NCAA) is unconditionally stable, but not unconditionally accurate, so as Δt is reduced the error in the resulting acceleration approximation decreases.

The generally accepted method for determining a sufficient value for Δt is to perform a modal analysis on the structure of interest, analyse the expected loading pattern, and select the number of modes that are expected to participate in the dynamic response of the structure. The initial time step size (Δt) is then set to be 10% of the period of the highest contributing mode. For all analysis presented in this work the first ten modes were selected.

$$\Delta t = 0.1 \times T_{10} \quad (2.25)$$

where T_{10} is the natural period of mode 10.

The incremental form of the NCAA is defined, [Carr, 2001; Humar, 1990]:

$$\left(\frac{4}{\Delta t^2}[M] + \frac{2}{\Delta t}[C] + [K]\right)\{\Delta v\} = \{p_{n+1}\} + [M]\left(\frac{4}{\Delta t}\{\dot{v}_n\} + \{\ddot{v}_n\}\right) + [C]\{\dot{v}_n\} - [K]\{v_n\} \quad (2.26)$$

$$\{\Delta\dot{v}\} = \frac{2}{\Delta t}\{\Delta v\} - 2\{\dot{v}_n\} \quad (2.27)$$

$$\{\Delta\ddot{v}\} = \frac{4}{(\Delta t)^2}\{\Delta v\} - \frac{4}{\Delta t}\{\dot{v}_n\} - 2\{\ddot{v}_n\} \quad (2.28)$$

These equations compute the changes in displacement ($\{\Delta v\}$), velocity ($\{\Delta\dot{v}\}$) and acceleration ($\{\Delta\ddot{v}\}$) from the structural state at the start of the time step ($\{v_n\}$, $\{\dot{v}_n\}$, $\{\ddot{v}_n\}$) from the forces at the end of the time step ($\{p_{n+1}\}$). Hence

$$\{v_{n+1}\} = \{v_n\} + \{\Delta v\} \quad (2.29)$$

and similarly for the other response quantity vectors.

2.3.1. Equilibrium

If the properties of a system change causing changes in the stiffness of the system, as is common in systems exhibiting non-linear force deflection relationships, the NCAA will not adequately maintain equilibrium within the system. Thus, external means are required to ensure that equilibrium is maintained at the conclusion of each time step. In the current framework changes in stiffness only occur as a result of configuration updates to account for large deflections.

For linear, or largely linear, elastic systems, applied loads are always resisted by the internal actions. Figure 2.3 displays the response of such a system. However, in the case of non-linear systems where the system stiffness changes as

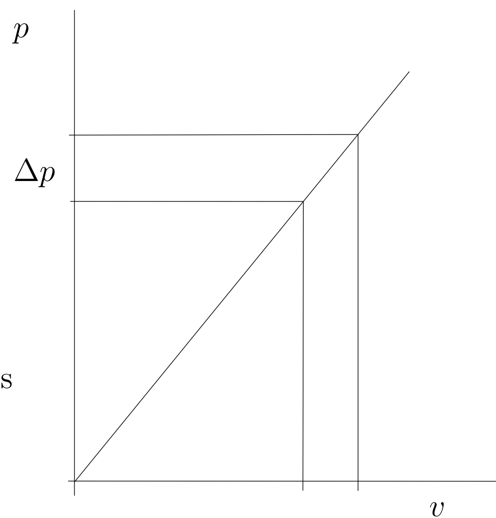

Figure 2.3. Linear system force deflection relationship

the load is applied the tangent stiffness $[K_T]$ is used to represent the instantaneous system stiffness. A reasonable approximation would be to use the average tangent stiffness $\left[\bar{K}_T\right]$, however the change in displacement (Δv) for the current time step is not known at the beginning of the timestep. Thus, it is necessary to iterate during the timestep. Figure 2.4 shows the effect of such iterations for the initial (tangent) stiffness method and the tangent stiffness method.

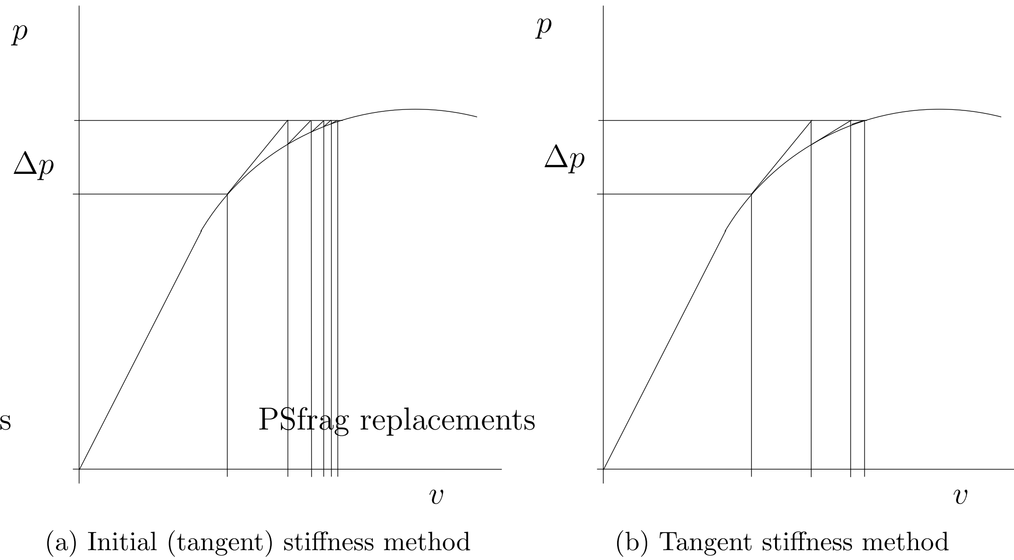

(a) Initial (tangent) stiffness method

(b) Tangent stiffness method

Figure 2.4. Non–linear system force deflection relationship

Zienkiewicz's procedure for maintaining equilibrium in a finite element assemblage utilizes the tangent stiffness at the beginning of the timestep, as the stiffness for all subsequent iterations, however this approach can take a significant number of iterations to achieve equilibrium, as Figures 2.4 (a) & (b) illustrate. Carr [1967] reduced the number of iterations required by recomputing the tangent stiffness at each iteration.

For the GEMS structure the system stiffness assembly procedure is extremely computationally expensive, which is not the case with finite element assemblages containing only beam and column elements. In the interests of solution efficiency, if an equilibrium strategy is required the use of the Zienkiewicz approach is recommended.

Problems can also arise when a system is pushed beyond yield and the system deforms with no additional applied load. This phenomena occurs when the system achieves a state of zero effective stiffness. The determinant of the system stiffness matrix changes sign and the sign changes on the additional load in-

crements. Clearly the Zienkiewicz approach is invalid in such a case, and Carr's approach also poses difficulties, as illustrated by the dashed line in Figure 2.5 (a). For treatment of such systems the reader is encouraged to explore the work of

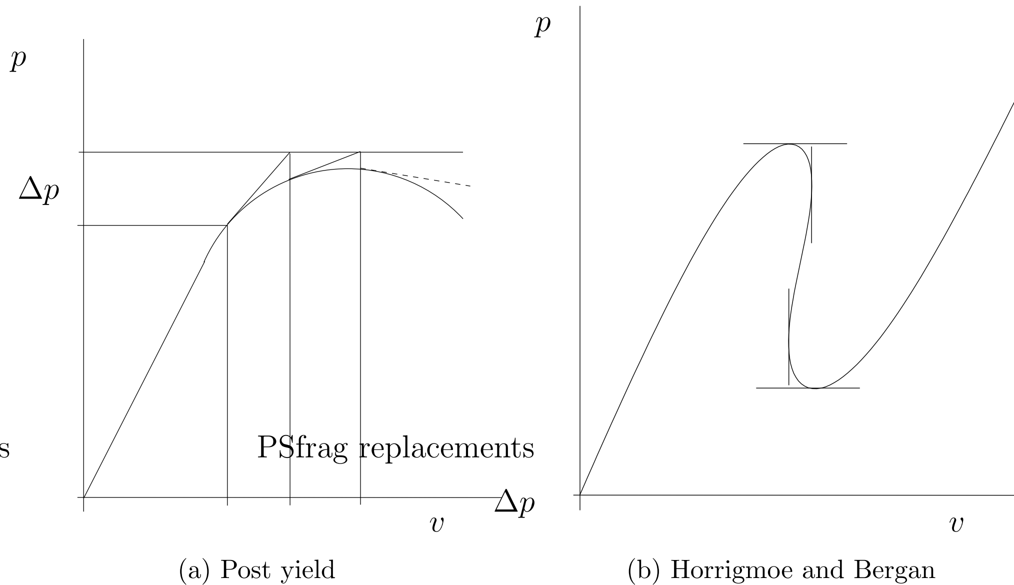

(a) Post yield

(b) Horrigmoe and Bergan

Figure 2.5. Problematic system force deflection relationships

Horrigmoe and Bergan [1978], who modelled the snap through buckling dynamics of curved thin shell structures, covering both the zero and infinite stiffness phenomena. For electro-mechanical MEMS structures the zero stiffness case occurs at well defined points, called bifurcation points, discussed in Section 2.5.

2.4. Large deflection

The deformation of such MEMS structures can typically be characterised as small, with deflections typically on the order of nm and structural dimensions in the µm range. However, as the structure deforms the initial planar system model must be updated to include the effects of the deformation, as the assumed linearity of the finite element method degenerates. Commonly termed large deflection effects, as the structural configuration is significantly different from the original configuration, this update includes reforming and assembly of the three system matrices, $[M]$, $[C]$ and $[K]$.

In this configuration update, the elemental formulation process occurs in the elemental co-ordinate system. Denoted in Figure 2.6 with a prime, this

elemental information must be transformed into the global co-ordinate system to be assembled with the other elements. The form of this transformation is a

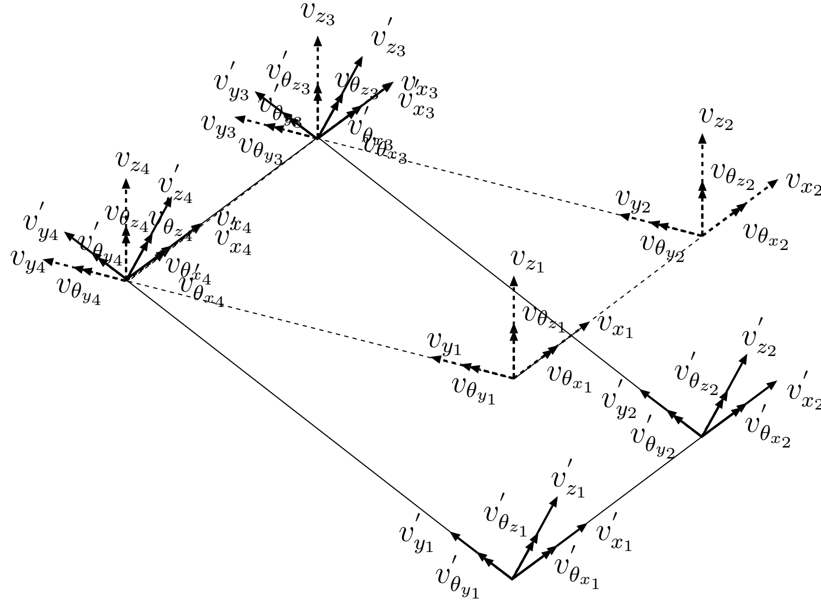

Figure 2.6. Large deflection elemental transformations

rotation, as the elemental properties are a function of element size and not of elemental location in the global system.

For thin film structures two criteria need to be considered, the strain in the structure and the local rotation experienced. The two criteria used to assess the need for a large deflection update are:

- Elemental rotation
- Elemental strain

The values at which such an update should occur are user defined. The technique for updating the system configuration utilises transformations to map the local system properties to the global orientation. This transformation involves rotating the frame of reference for each element, to reflect the deformed position. A treatment of such effects is covered in Rajasekaran and Murray [1973].

2.5. Electrostatic loading

Electrostatic loading is generated by the electric field between the two charged conductors and is non-linearly position dependent. If one of the conductors is

free to move it will move towards or away from the other, depending on the sense of the applied load. Modelling forces on capacitive elements requires the computation of the electric field surrounding the capacitive elements, including the effects of any dielectric materials that may be present. From the electric field the forces on the conductors can be determined.

Computation of electrostatic forces is typically performed using a boundary element formulation in a package such as FastCap [Nabors and White, 1991]. However, this tool requires that the model state be translated to a separate file format and an external program used, deviating from the desire to capture the dynamics in a single cohesive framework. Care must be taken when sizing meshes in a mixed finite and boundary element solution, as the location of nodes, can impinge on solution accuracy.

Adopting a finite element approach to the solution in the electrostatic domain is also difficult as it requires remeshing or mesh adaption for each update to the structural configuration, which is computationally expensive. Furlani et al. [1998] has shown that for simple planar structures utilizing a parallel plate capacitor model is sufficient, particularly when the movable conductor is the active electrode and the substrate acts as earth. As the GEMS device deforms the finite element mesh does not remain planar, however if a sufficiently small mesh size is used the approximation of the forces on the movable structure is adequate.

In this research the existing finite element discretization is utilized as the basis for computing the forces on the movable structural elements. The element discretization describes a series of small parallel plate capacitors, which as the mesh is refined provide an increasingly accurate approximation of the electrostatic forces on the movable electrode. This approach integrates the electrostatic solution within the general model framework. It does not require a detailed description of the fixed electrode, or the expression of the model in a foreign format. The overall result is a simple efficient approach to modelling the electrostatic forces on the movable structure.

The formulation for the specific parallel place capacitor model used, ignores any small discontinuous regions of dielectric between the conductors as 2D finite element modelling has shown that they only act as local concentrators of electric field and have little effect on the total force experienced by the conductors. The specific structures ignored are the standoffs which cover less than 9% of the plan area between electrodes. The governing force relationship for the parallel plate capacitor, shown in Figure 2.7, can be obtained by using the Maxwell Stress

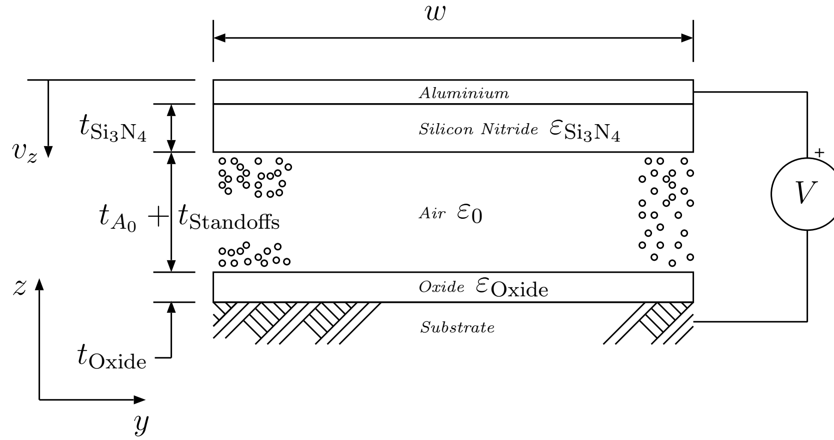

Figure 2.7. Parallel plate capacitor definition

tensor [Davey and Klimpke, 2002] or virtual work approach.

$$p_z = \frac{-\varepsilon_0 V^2 w l}{2\left[t_{\mathrm{Si_3N_4}}\frac{\varepsilon_0}{\varepsilon_{\mathrm{Si_3N_4}}} + t_{\mathrm{Standoffs}} + t_{A_0} + t_{\mathrm{Oxide}}\frac{\varepsilon_0}{\varepsilon_{\mathrm{Oxide}}} - v_z\right]^2} \tag{2.30}$$

Where ε are electric permativities, t, w and l are the structural dimensions, V is the applied voltage, v_z is the vertical deflection of the movable conductor and p_z is the resulting force on the movable electrode. Equation (2.30) states that the force generated between conductors is proportional to the inverse of the square of the electrode deflection. Thus, as the structure deforms the force increases as a function of that displacement, as illustrated in Figure 2.8. Hence, the computation of electrostatic forces requires an iterative approach to determining the structural equilibrium state at the end of each time step.

An iterative approach to the structural solution is also required because the NCAA method requires the forces on the structure at the end of the time step (p_{n+1}) to determine the final structural state from the state at the beginning of the time step (v_n, $\dot{v}_n$, $\ddot{v}_n$). Iteration is required to determine the correct set of structural displacements and electro-static forces during each numerical time step. This iteration is called Self–Consistent–Electro–Mechanics (SCEM) [Osterberg et al., 1994a]. A relaxation algorithm is typically used to determine when electro-mechanical equilibrium has been achieved, but more efficient methods also exist [Cai et al., 1993]. A relaxation method was adopted by comparing the $\mathbf{L_2}$ norms of the vertical deflection of the electrostatic and final ribbon unit positions.

For simple micro-device structures such an iterative algorithm has been shown

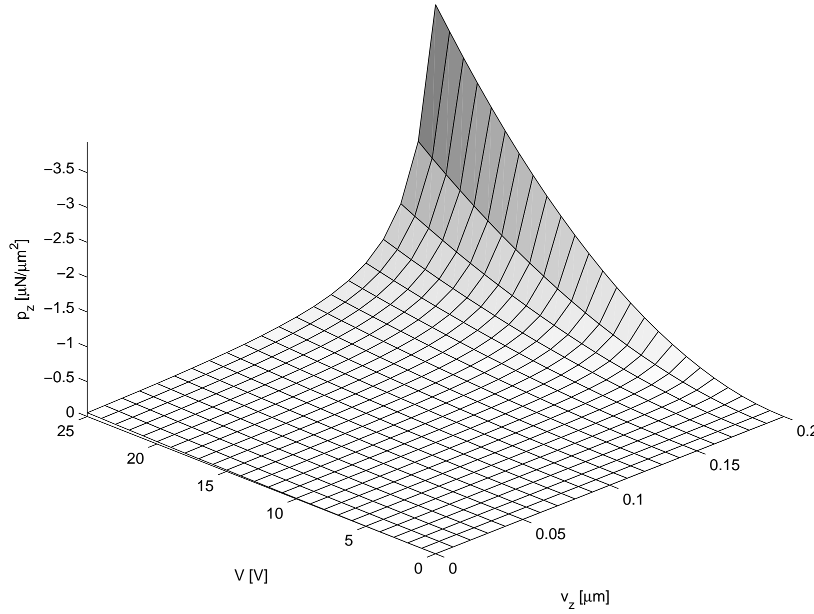

Figure 2.8. Parallel plate force (p_z) variation with applied voltage (V) and electrode deflection (v_z)

to be sufficient, as the additional solution complexity of other methods is not warranted. Finally, integrating more complex procedures with the NCAA is not currently well documented.

2.5.1. Bifurcation

Electrostatically actuated thin structures reach a deflection where the non-linear electrostatic force exceeds the linear restoring forces, causing a bifurcation of state. Bifurcating thin strip structures exhibit two inherently stable states shown schematically in Figure 2.9, and switch in a binary fashion between these two states on the application of sufficient voltage. These two states are the key feature of bifurcating MEMS structures that suits them to switching applications. Figure 2.9 (a) is the natural state of the structure with no load applied ($V = 0$). To change state a voltage greater than the pull down voltage (V_{PD}) is required. The force on the structure increases as an inverse quadratic function of gap between the structure and ground electrode as seen in Equation (2.30). Thus, a set of state variables exist where the applied force exceeds the restoring ability of the structure.

This effect can be shown mathematically by examining Equation (2.17) and

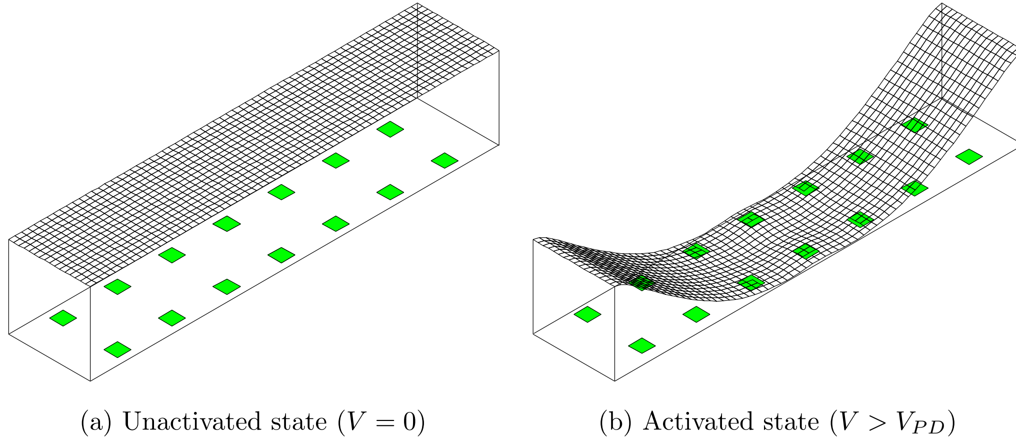

(a) Unactivated state ($V = 0$) (b) Activated state ($V > V_{PD}$)

Figure 2.9. Finite element mesh of stable structural states

recognizing that the applied load (p) is proportional to the inverse of the square of displacement,

$$p \propto \frac{1}{v^2} \tag{2.31}$$

Thus Equation (2.17) reduces to,

$$M\ddot{v} + C\dot{v} + \left(K - \beta\left(\frac{1}{v^3}\right) + K_g\right)v = 0 \tag{2.32}$$

Where $\beta\left(\frac{1}{v^3}\right)$ is a matrix function of $\left(\frac{1}{v^3}\right)$, including a proportionality constant that maps the electrostatic load to the vertical degrees-of-freedom. Thus, for a given velocity and acceleration a voltage and displacement exist such that the system exhibits zero stiffness. Assuming that small deflection theory applies and K does not change, Equation (2.32) resembles a constrained linear buckling problem. At this point, additional voltage only acts to accelerate the structure and for little change in applied voltage, large changes in displacement are realized, The structure bifurcates to the new stable position. The voltage at this bifurcation point is commonly termed the pull down voltage (V_{PD}). Deflection is limited by spacing structures, called standoffs, as shown in Figures 1.5 and 2.9.

When contact with the underlying structural elements occurs the displacement of the contacted portions of the movable structure stop as additional constraint is enforced, changing the behaviour of the system. Additional applied forces are distributed in the new system causing deflection where the structure is least stiff, in the non-contacted regions. This phase of operation is termed zipping

and occurs in an extremely short period of time. Zipping ends when the structures restoring forces exceed the additional applied load. Thus, the second stable state is reached, as shown in Figure 2.9 (b), effectively a new stable structure.

Increasing the voltage above this value typically yields little change in displaced shape, with extreme voltages required to pull the remaining free structure portions into contact with the standoffs. Decreasing the applied voltage reduces the number of points of contact and release ensues, starting with the outermost contact points moving back toward the point of first contact. Eventually, the stiffness of the system becomes positive once more as restoring forces exceed electrostatic forces and the structure releases. At this release voltage (V_{RL}) the structure resorts to the initial stable state. In the deformed state the two electrodes are in close proximity, resulting in large loads on the movable structure. As the voltage is reduced this force reduces but only slowly, due to the quadratic relationship between deflection and applied force. Hence, $V_{RL} < V_{PD}$ and the occurrence of electro-mechanical hysteresis in the response of the structure, as seen in Figure 1.1.

2.6. Contact

Common approaches to numerically modelling contact between structural elements apply pseudo-loads to structural elements, restricting penetration based on a penalty function formulation [Hirota et al., 2001]. Other methods incorporate the mass and stiffness of the surrounding structure or try to approximate the mass and stiffness of the surrounding structure, thus providing an energy sink and removing kinetic energy from the deforming structure.

Including the surrounding structural elements in the model domain, requires care as such an approach can potentially add more degrees of freedom then currently exist in the model. For the GEMS ribbon unit such an approach is infeasible, since beyond the oxide layer nothing is known about the body to which the GEMS device is connected. The ribbon unit also moves very rapidly with large accelerations so a significant portion of the connected structure would be required to remove sufficient energy from the ribbon unit to cause it to come to rest after making contact.

Approximating the mass and stiffness of the surrounding structure, also causes problems. Specifically how to distribute the approximated stationary structure to the one in motion. More specifically, how to achieve this effect

in such a manner as a “hard” surface is presented to the structure in motion.

It was subsequently decided that neither of these approaches were suitable for the GEMS ribbon. An efficient approach to contact must retain the connectivity of the structural system. Disconnecting a node from its surrounding neighbours causes the modified node to feel the effects of contact due to the additional constraint, but the effect does not propagate into the surrounding structural domain. The result is that the non-contacted portions of the structure continue in motion, unaffected by contact, experiencing no loss in energy, resulting in a poor deformation solution surrounding the points of contact.

Contact in dynamic models is complicated due to the lack of prior knowledge as to how the structure will deform during the timestep, how the structure will conform to the other structural elements, and which nodes will be in contact at the end of the time step. In addition, the movable structure must be allowed to break contact given correct application of forces. Thus, the structure must not be deliberately held down between consecutive timesteps to allow an accurate determination of the release voltage (V_{RL}). Ideally, energy must be conserved in the system model during the elastic collision.

In a practical model, conservation of energy gives rise to perfectly elastic collisions, removing no energy from the system. Problems arise as real devices dissipate energy when contact occurs, causing the device to slow down and, locally, come to rest. All numerical approaches to contact must decide how much energy to remove. Thus, it is only possible to determine the actual energy loss by tuning the model with real experimental data, which is infeasible for pre-production simulation of experimental MEMS devices.

The adopted approach is to zero the velocities and accelerations of the node that is in contact. This technique violates elastic conservation of energy and acts as an energy sink, removing energy from the model during the collision. Such an approach prevents energy from being reflected back into the movable structural elements, preventing the unrealistic bounce observed in simulations with perfectly behaviour. From a maximum deflection stand point such an approach is considered conservative as it allows the movable structure to conform to the underlying structural elements in a manner that may exceed that of the real system.

Examination of the equations for the Newmark Constant Average Acceleration (NCAA) scheme, suggests that contact is just a special case, of the general scheme. Assuming the modelling approach can accurately determine the

time of contact, in subsequent timesteps if the node is still in contact in the following timestep the vertical (z) deflection of the contacted node ($\{\Delta v_z\}$) in Equation (2.26) is known a priori as zero. Hence, the change in deflection for the contacted nodes is known, the applied electrostatic force at the end of the timestep $\{p_{n+1}\}$ is known but is of little value as the contact forces are a desired model output. Thus, $\{p_{n+1}\}$ for the contacted nodes is unknown and Equation (2.26) can be augmented, collecting the equations relating to the contacted nodes and those related to the non-contacted or free nodes.

$$\begin{bmatrix} A_{11} & A_{12} \\ A_{21} & A_{22} \end{bmatrix} \begin{Bmatrix} \Delta v_1 \\ \Delta v_2 \end{Bmatrix} = \begin{Bmatrix} p_{n+1_1} \\ p_{n+1_2} \end{Bmatrix} + \begin{Bmatrix} b_1 \\ b_2 \end{Bmatrix} \tag{2.33}$$

Where,

$$[A] = \left[\frac{4}{\Delta t^2} [M] + \frac{2}{\Delta t} [C] + [K] \right] \tag{2.34}$$

$$\{b\} = \left\{ [M] \left(\frac{4}{\Delta t} \{\dot{v}_n\} + \{\ddot{v}_n\} \right) + [C] \{\dot{v}_n\} - [K] \{v_n\} \right\} \tag{2.35}$$

And $\{\Delta v_1\}$ are the unknown changes in deflection, $\{\Delta v_2\}$ are the known changes in deflection for the contacted nodes so $\{\Delta v_2\} = 0$, p_{n+1_1} are the applied nodal loads at the end of the timestep and p_{n+1_2} are the unknown contact forces.

Determining when a model node should experience additional constraint is critical to accurate determination of the pull down and release voltages of the structure. Thus, it is important that at each numerical integration step, additional constraints due to contact be removed from the model and the model be allowed to freely deform. If during this initial step model nodes make contact, additional constraint is applied (or re-applied) and the step repeated to determine the effects of the additional constraint(s).

Accurately modelling contact between movable and stationary structural components requires consideration of the energy transferred between the participants. However, micro-devices are typically assembled to form part of a product that is many orders of magnitude larger, with much larger mass and stiffness than the movable structural element. In this case, consideration must include the extent of the model, as the micro-device is the structure of interest not the system as a whole. Hence, the decision to remove energy through the zeroing of the velocities and accelerations of contacted nodes.

The dynamic time step size (Δt) must also be controlled to determine when

contact between the structure of interest and the surrounding structure first occurs. This control is achieved by allowing a small penetration buffer in the surrounding structural elements. This buffer is easily rationalised due to the variation that occurs in batch fabricated MEMS devices. The adopted buffer size is 0.001nm, much less than 1% of the smallest critical structural dimension, the thickness of the device.

The time step size is reduced as previously free nodes penetrate the underlying structure and the time step restarted with the new, reduced Δt until the penetration is within the buffer limit and the node is deemed to be in contact. For dynamic modelling using the NCAA it is difficult to know when to grow Δt to maintain computational efficiency. This issue is overcome by attempting to constantly grow the time step size, Δt, back to its more efficient base value.

2.7. Opto–mechanical coupling

For planar optical microdevices it is possible to compute the diffractive efficiency using scalar diffraction theory [Bass, 1995]. Kowarz et al. [2002] presents such an analysis for a GEMS device using a quasi-static model, using both square and trapezoidal assumed profiles.

Equation (2.36) allows an arbitrarily deformed ribbon unit profile to be used to compute the diffractive efficiency (η_m).

$$\eta_m = \left| \frac{1}{\Lambda} \int_0^{\Lambda} e^{\frac{-i4\pi z(x)}{\lambda}} e^{\frac{-i2\pi m x}{\Lambda}} dx \right|^2 \tag{2.36}$$

Where Λ is as defined in Figure 1.5 and Figure 1.6 (a), λ is the wavelength of incident light and m is the order of diffracted light collected.

Utilizing the existing finite element discretization for the GEMS ribbon unit, the trapezium rule can be used to numerically evaluate the complex integral in Equation (2.36). Computing the magnitude of the resulting quantity ensures that only the amplitude of the diffracted light is considered not the phase.

Such an approach fails to consider the deformation across the ribbon. A more complex approach similar to the one presented in Kurzweg et al. [2003] must be considered to accurately capture the effect in three dimensions. The adoption of a numerical approach does not effect the accuracy of the result as it exact for the chosen finite element discretization. This research has adopted the simplified approach in the interest time.

Chapter 3

Implementation

Integrating residual stress, electrostatic loading, contact and large deflections into a dynamic finite element framework utilizing the Newmark Constant Average Acceleration scheme to perform numerical integration, results in the decision structure shown in Figure 3.1. The resulting two loops, control the numerical marching procedure and electrostatic equilibrium at each time step. Contact and large deflections are handled using simple branches, although contact can require recursion, to be captured accurately. The complete framework is implemented in the Matlab environment, in a cohesive system designed to handle MEMS devices. No data is passed to any external program.

Simulations are conducted in blocks, allowing partial data to be analysed before simulations reach completion, and allowing simulations to be run that require history data above the capacity of the host system (Table C.1, Appendix C). A restart block mechanism is also present to enable efficient debugging, and faster computation for multiple simulations.

3.1. Multilayer approximation

Idealizing the composite GEMS ribbon of Figure 1.5 as a single layer of material and utilizing a single layer of hybrid stress finite elements to increase computational efficiency, it is necessary to account for the difference in both stiffness and density observed in the two materials (Al, Si_3N_4) present in the physical structure. The GEMS device response is bending dominated, hence the variation in stiffness can be accounted for by calculating an equivalent thickness ($\tilde{t}$) from an equivalent stiffness of the composite ribbon unit. While the variation in density can be expressed using an equivalent density ($\tilde{\rho}$) to obtain a correct mass matrix.

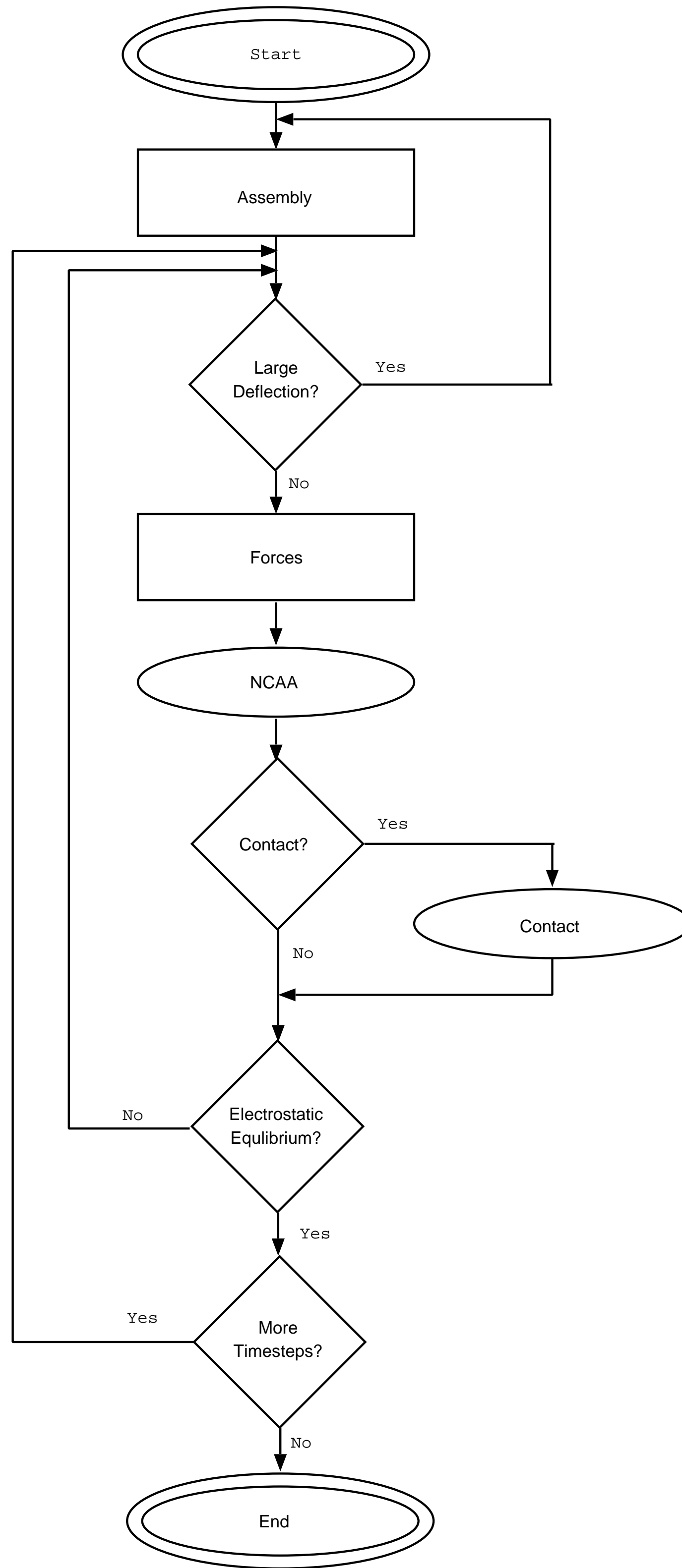

Figure 3.1. Implementation framework

3.1.1. Equivalent thickness

By requiring identical equivalent bending stiffness (EI) for the physical device and model cross sections shown in Figure 3.2, it is possible to calculate an appropriate $\tilde{t}$ for the model. The y axis, in Figure 3.2, is chosen as the axis about which the second moment of area (I) is to be calculated as it is common to both Figures 3.2 (a) and (b) and is independent of $\tilde{t}$.

PSfrag replacements

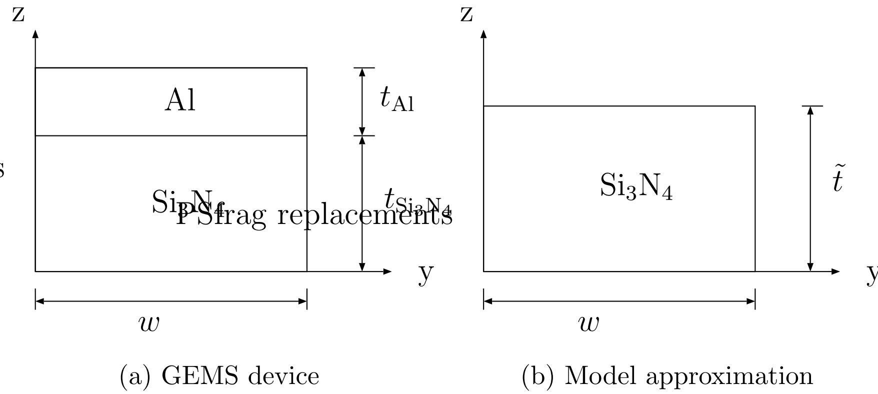

(a) GEMS device (b) Model approximation

Figure 3.2. Structural ribbon cross section approximation (exaggerated vertical scale)

Neither Figures 3.2 (a) or (b)'s neutral axis is located at the y axis, thus it is necessary to use the parallel axis theorem. The calculation of $\tilde{t}$ is derived from established device parameters:

$$\tilde{t} = \sqrt[3]{\frac{\mathrm{E}_{\mathrm{Al}} t_{\mathrm{Al}}^3 + 3\mathrm{E}_{\mathrm{Al}} t_{\mathrm{Al}} t_{\mathrm{Si_3N_4}}^2 + 3\mathrm{E}_{\mathrm{Al}} t_{\mathrm{Al}}^2 t_{\mathrm{Si_3N_4}} + \mathrm{E}_{\mathrm{Si_3N_4}} t_{\mathrm{Si_3N_4}}^3}{\mathrm{E}_{\mathrm{Si_3N_4}}}} \tag{3.1}$$

Where t indicates a thickness and E a modulus of elasticity. For the model device,

$$\begin{aligned} t_{\mathrm{Al}} &= 50\mathrm{nm} \\ t_{\mathrm{Si_3N_4}} &= 100\mathrm{nm} \\ \mathrm{E}_{\mathrm{Al}} &= 70\mathrm{GNm}^{-2} \\ \mathrm{E}_{\mathrm{Si_3N_4}} &= 250\mathrm{GNm}^{-2} \end{aligned}$$

The resulting equivalent thickness $\tilde{t} = 118.52$nm, slightly thicker than the Silicon Nitride of the GEMS device, reflecting the small contribution to stiffness from the Aluminium.

3.1.2. Equivalent density

Using a unit plan area of ribbon unit, the equivalent density ($\tilde{\rho}$) can be calculated.

$$\tilde{\rho} = \frac{t_{\mathrm{Al}}\rho_{\mathrm{Al}} + t_{\mathrm{Si_3N_4}}\rho_{\mathrm{Si_3N_4}}}{\tilde{t}} \tag{3.2}$$

For the model structure,

$$\begin{aligned} \rho_{\mathrm{Al}} &= 2710\mathrm{kgm}^{-3} \\ \rho_{\mathrm{Si_3N_4}} &= 3180\mathrm{kgm}^{-3} \end{aligned}$$

For the model device $\tilde{\rho} = 3826\mathrm{kgm}^{-3}$, greater than both $\rho_{\mathrm{Si_3N_4}}$ and ρ_{Al} but less than the sum of the two, reflecting the additive contribution to device weight from both constituent materials.

3.1.3. Equivalent initial stress

The GEMS device contains both stressed Silicon Nitride and unstressed Aluminium. The simplified model structure consists of a single layer of material, so the whole model cross section is placed in a state of tensile stress. The level of stress in the model needs to reflect both the unstressed aluminium and the equivalent ribbon thickness.

For a string structure, the tensile axial stress can be related directly to the axial force in the structure. Requiring similarity in the axial forces of the manufactured device and the model allows the calculation of an equivalent initial material stress ($\tilde{\sigma}$).

$$\tilde{\sigma} = \frac{t_{\mathrm{Si_3N_4}}}{\tilde{t}}\sigma_n \tag{3.3}$$

Where σ_n is the normal stress present in the Silicon Nitride of a manufactured GEMS device (1100 MPa). Therefore, for the simplified single material model structure, $\tilde{\sigma} = 932\mathrm{MPa}$.

3.2. Symmetric model reduction

Using the principals of symmetry it is possible to significantly reduce the number of degrees of freedom in the dynamic finite element model. The GEMS ribbon

unit is symmetric about two axis; the centerlines in both the x and y directions. By only including the elements in the model in the lower quarter of the ribbon unit it is possible to reduce by 75% the number of degrees of freedom in the model, with obvious gains in computational speed and storage requirements.

Symmetric reduction is achieved by only including one quarter of the ribbon unit in the finite element model and applying appropriate constraints at the lines of symmetry, to stop the structure moving out of plane and enforce rotation compatibility.

The drawback of symmetrical model reduction is removal of the ability to capture the torsional dynamics of the ribbon unit, which a quick comparison of the modeshapes of the normal and reduced structure reveals. However, the applied electrostatic force shares the same planes of symmetry as the structure, and the electroding of the GEMS structure is such that even minor electrostatic attraction to neighbouring ribbon units is not anticipated to occur. Thus, symmetric reduction has been utilised.

Symmetric reduction would not be applicable if the modelling of fluid damping in the system were to include pressure effects, giving the ribbon the ability to pump fluid. In this case a full GEMS ribbon unit would be needed to ensure that the varying pressure distribution beneath the ribbon did not cause torsional excitation. The finite element implementation utilized is such that it is possible with the developed code to model full, half and quarter of the GEMS ribbon unit.

3.3. Stress calculation

The absence of coupling between the bending and membrane characteristics in the mixed finite element formulation developed, requires the superposition of the resulting stress components in order to determine the magnitude of the stresses in the materials of the GEMS ribbon unit. The bending degrees of freedom provide the peak bending stresses in the ribbon unit, maximum at the upper and lower surfaces, consistent with standard notation for bending structures centrally deflected downward. Thus the peak tensile bending stress occurs at the lower surface of the ribbon ($+\sigma_b$) and the peak compressive bending stress occurs at the upper surface of the ribbon ($-\sigma_b$). The membrane stress, the result of the initial material stress, via $\{q\}$ unless reassembly is enabled, is uniform throughout the structure.

Figure 3.3 (a) & (b) illustrate the stress distribution in a generic single layer

bending structure with an applied initial material stress. A tensile stress value is indicated by an arrow in the positive x direction. The dashed lines indicate the

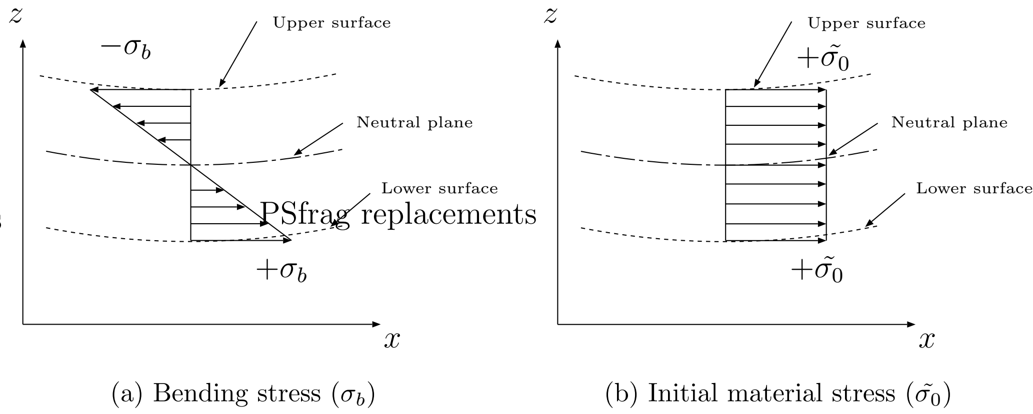

(a) Bending stress (σ_b)

(b) Initial material stress ($\tilde{\sigma_0}$)

Figure 3.3. Single layer structure stress distributions

location of the key planes of the structure and the arrows indicate the direction of the induced stresses.

From Figure 3.3 the maximum compressive stress in the structure is:

$$\sigma_{\text{min}} = -\sigma_b + \tilde{\sigma_0} \tag{3.4}$$

And the maximum tensile stress:

$$\sigma_{\text{min}} = \sigma_b + \tilde{\sigma_0} \tag{3.5}$$

For values of σ_b less then the initial material stress, the effects of the initial material stress dominate the stresses in the structure. Also the high tensile initial material stress reduces the structures propensity to buckle.

For a composite structure the stress distribution differs from that shown in Figure 3.3. As Figure 3.4(a) illustrates the centroidal plane and neutral plane no longer coincide. the centroidal plane remains in the same location as in Figure 3.3 as its location is a function of the cross sectional area of the structure, however due to the differing stresses in the structure the neutral plane is moved. Figure 3.4(b) illustrates the presence of the initial material stress in the Silicon Nitride layer.

Determining the stresses in the composite structure requires information in addition to what is available in the results from the single layer structure. While it is possible to locate the neutral plane of the composite structure and maintain

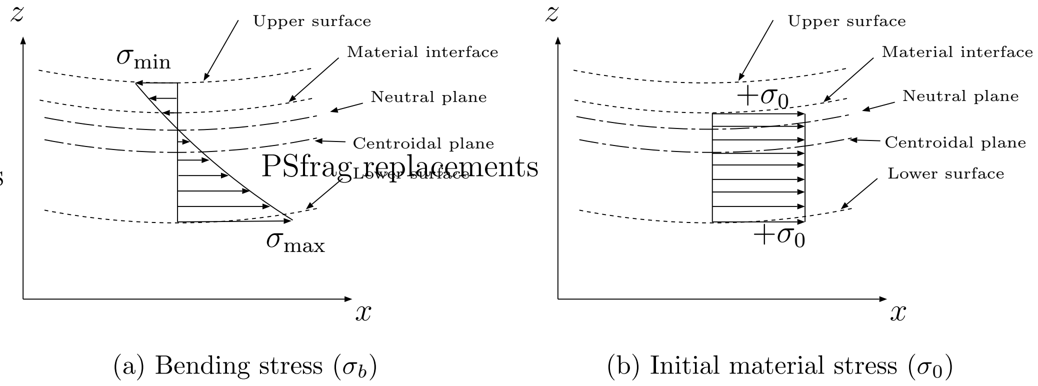

(a) Bending stress (σ_b) (b) Initial material stress (σ_0)

Figure 3.4. Composite structure stress distributions

equivalent areas beneath the stress distributions, the stresses at the upper, lower and interfacial surfaces are unknown, providing no reference from which to derive the remaining stress distribution. Thus the results of a the single layer model can only be used to approximate the stresses in the GEMS ribbon unit.

Combined with a knowledge of the alloy system used in the Aluminium layer it is possible to estimate the service life of the simulated structure, subject to the assumed loading pattern, with respect to stress cycling and high cycle fatigue. From this information the lifetime of the structure and the product in which the device is used may be determined.

Chapter 4

Model Verification

Incrementally verifying the solution technique developed as the framework develops allows the accumulation of functioning code providing verifiable results. This chapter discusses the model implementation and verification. Specifically, the steps in the verification process and what was tested and presents results for the verification test cases.

4.1. Felippa cantilever

To assess the accuracy of the element formulation utilized and determine the functionality of the assembly, solution and visualization routines a structure called the Felippa cantilever [Carr, 1967; Felippa, 1966], with the C1 mesh, was utilized. The results are compared with the structural dynamics package RUAUMOKO, [Carr, 2001], and results presented in the literature.

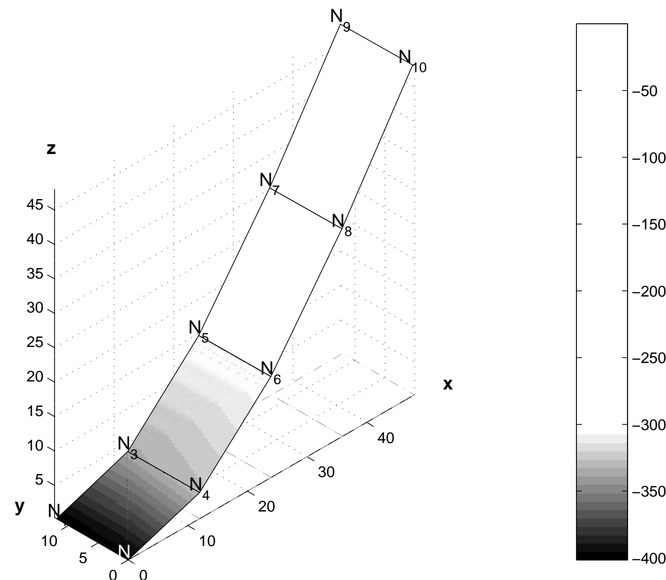

Figure 4.1. Deformed Felippa cantilever, illustrating bending stress contours

As the bending and membrane behaviours are uncoupled it is possible to test the structure in bending and shear simultaneously. Applying a load of 20N in the $+v_y$ and $+v_z$ directions and solving for the deflections of the structure, using $\{p\} = [K]\{v\}$, produces the deformed structure shown in Figure 4.1. As expected, the greatest bending stresses occur at the fixed end of the cantilever.

Table 4.1 lists the deflection results obtained from the Felippa cantilever test and Table 4.2 lists the corresponding results from the RUAUMOKO structural dynamics package. Comparing Table 4.1 and Table 4.2 the agreement obtained

Table 4.1. Fellipa Cantilever test deflection results

Node	v_x	v_y	v_z	v_{θ_x}	v_{θ_y}	v_{θ_z}
N_3	-0.02755	0.03090	3.771	-0.09121	-0.6389	0.004949
N_4	0.02755	0.03090	3.771	0.09121	-0.6389	0.004949
N_5	-0.04710	0.1090	14.59	-0.05738	-1.120	0.008275
N_6	0.04710	0.1090	14.59	0.05738	-1.120	0.008275
N_7	-0.05881	0.2185	30.01	-0.02920	-1.408	0.01024
N_8	0.05881	0.2185	30.01	0.02920	-1.408	0.01024
N_9	-0.06271	0.3435	47.74	0.009367	-1.502	0.01089
N_{10}	0.06271	0.3435	47.74	-0.009367	-1.502	0.01089

Table 4.2. RUAUMOKO Fellipa Cantilever test deflection results

Node	v_x	v_y	v_z	v_{θ_x}	v_{θ_y}	v_{θ_z}
N_3	-0.02755	0.0309	3.771	-0.09121	-0.6389	0.004949
N_4	0.02755	0.0309	3.771	0.09121	-0.6389	0.004949
N_5	-0.0471	0.109	14.59	-0.05738	-1.12	0.008275
N_6	0.0471	0.109	14.59	0.05738	-1.12	0.008275
N_7	-0.05881	0.2185	30.01	-0.0292	-1.408	0.01024
N_8	0.05881	0.2185	30.01	0.0292	-1.408	0.01024
N_9	-0.06271	0.3435	47.74	0.009367	-1.502	0.01089
N_{10}	0.06271	0.3435	47.74	-0.009367	-1.502	0.01089

is exact to the number of significant figures available in the output from RUAUMOKO. The agreement is equally good for the computation of both elemental and average nodal stresses. Thus, the implementation of the hybrid stress finite element was successful and the assembly and static solution routines function as expected.

4.2. Model structure

The initial GEMS model parameters provided by Kodak were used to form the single layer structure described by Table 4.3 and Figure 4.2. The modifications required to achieve the equivalent single layer parameters $\tilde{t}$, $\tilde{\rho}$ and $\tilde{\sigma_0}$ are defined by Equations (3.1)-(3.3).

Table 4.3. Model structure parameters

Parameter	Value	Units
Length (l)	30	µm
Width (w)	6	µm
Thickness ($\tilde{t}$)	0.12	µm
Youngs modulus (E)	250	GNm^{-2}
Poissions ratio (ν)	0.33	
Density ($\tilde{\rho}$)	3826	kgm^{-3}
Initial stress ($\tilde{\sigma_0}$)	928	MNm^{-2}

This structure was used as the basis for the validation and verification of the analysis code, providing both existing experimental and numerical results for comparison. In subsequent tests this basic structure has been used as the basis of the specified test. Where alterations to this base structure are necessary they have been detailed in the individual sections.

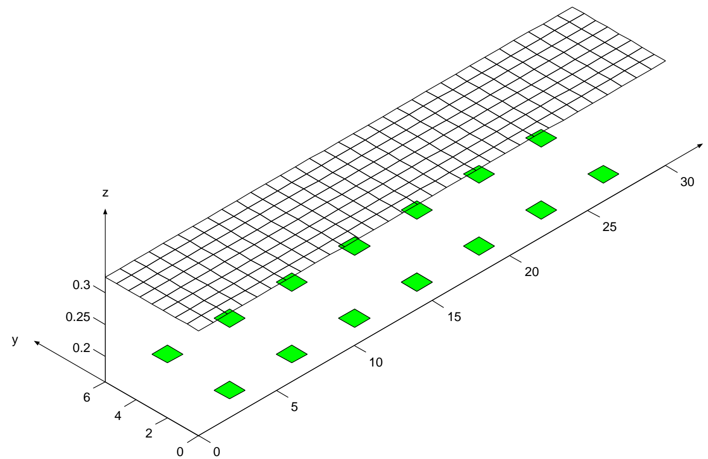

Figure 4.2. Model structure for code verification

4.3. Fixed-fixed beam comparison

Omitting the effects of the initial material stress (σ_0) and setting Poissions ratio (ν) to zero, matching the assumptions of beam theory, results in the structure outlined in Table 4.3 idealized as a fixed-fixed beam. Applying a central point load that will not cause contact, is not a whole number ($p = 8.27$), and is equally distributed among the nodes at the model center line, allows a direct comparison with standard analytical solutions. The analytical beam theory result is:

$$v_z = \frac{pl^3}{16Ewt^3} \tag{4.1}$$

Comparing this solution with the finite element results listed in Table 4.4 and illustrated in Figure 4.3, for different numbers of elements in the finite element model shows very good correlation.

Table 4.4. Fixed-fixed beam deflection results

Elements across (y)	Elements along (x)	v_z edge	v_z center
1	4	5.6425314	-
2	8	5.6030429	5.5823987
4	16	5.5917989	5.5863410
8	32	5.5888316	5.58747445
16	64	5.5880857	5.58774795
32	128	5.5878997	5.58781544
64	256	5.5878537	5.58783265

The fixed-fixed beam model allows the verification of the symmetric reduction of the model and shows the efficiency of the hybrid stress formulation at representing the stiffness of such a structure. The number of degrees of freedom in the finite element model was controlled by altering the number of element divisions across the width and along the length of the beam, as seen in Table 4.4.

The efficiency of the hybrid element formulation is clear in the result for the coarsest mesh, where the discrepancy is less than 2%, much lower than other element types. Such a mesh would not be adequate for capturing the deformation of the GEMS ribbon unit between standoffs, but is adequate for capturing central deflection.

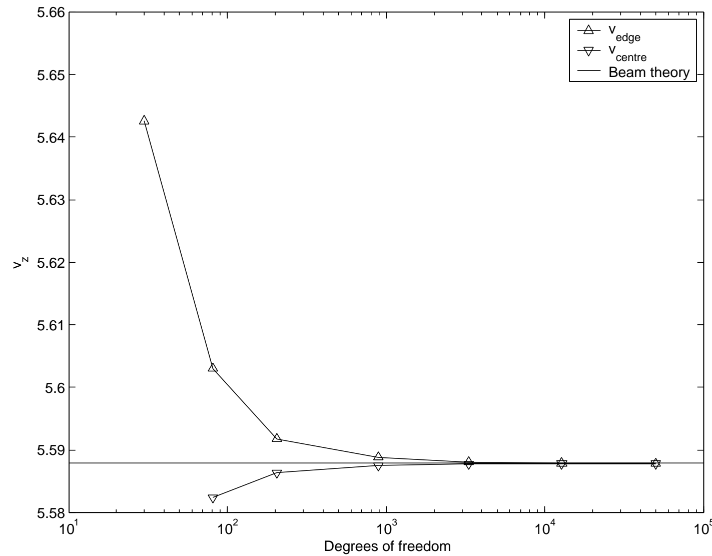

Figure 4.3. Fixed-fixed beam deflection comparison

Figure 4.3 shows that unlike displacement based finite element formulations the hybrid stress formulation does not exhibit the typical upper bound on displacement observed in displacement based elements. Thus, mesh refinement studies are required to determine the accuracy of the solution obtained. As Poissions ratio effects are neglected, the center and edge deflections are expected to be identical if the structure is loaded in a kinematically equivalent manner. Kinematically equivalent loading has not been used in this example as it allows a more conservative evaluation of element efficiency.

4.4. Dynamics comparison

Both the numerical representation of the system and the implementation of the NCAA method were tested to ensure correct operation. These two features were tested against the commercial finite element analysis package ANSYS in both modal and transient dynamic analyses with excellent results obtained. The ANSYS code for running the comparisons can be found in Appendix A.

4.4.1. Modal analysis

Comparing the modeshapes and frequencies of the model structure as computed using Equation (2.23) with the results obtained from ANSYS, verifies the accuracy of the system mass and stiffness representations. The frequencies of the

structure are listed in Table 4.5 and the first eight modeshapes are illustrated in Figure 4.4.

Table 4.5. Model structure and ANSYS natural frequencies

Mode	Model structure (Table 4.3) (MHz)	ANSYS (MHz)	Model structure ($\sigma_0 = 0$) (MHz)
1	8.56	8.56	1.12 (1)
2	9.19	9.16	3.66 (3)
3	17.21	17.22	3.09 (2)
4	18.46	18.42	7.58 (5)
5	26.05	26.07	6.07 (4)
6	27.91	27.87	11.96 (7)
7	31.05	31.14	29.90 (14)
8	35.17	35.23	10.07 (6)
9	36.61	36.62	32.58 (15)
10	37.63	37.60	16.97 (9)

For comparison the the frequencies of the structure in the absence of the initial material stress are also listed in Table 4.5 with their corresponding modeshape listed in parentheses. The dominance of the initial material stress on the structural dynamics is clear, in both the dramatic rise observed in fundamental frequency ($\approx 8\times$) and the changes observed in the order in which modes occur.

4.4.2. Dynamic analysis

Testing the Newmark integration scheme used to capture the linear dynamics of the model structure with the implementation in ANSYS for small deflections and with a Rayleigh damping model, gives the results presented in Figure 4.5. The two lines represent the displacement traces of the center point of the structure. The structure was subjected to a ramped centrally applied point load to a maximum of -5.5×10^{-3}N, which is removed in a single time step, allowing the structure to oscillate. The model was tested without the presence of the initial material stress, as ANSYS was unable to easily apply the initial material stress to a transient dynamic analysis. Note that the two lines in Figure 4.5 are effectively identical, verifying the approach and model.

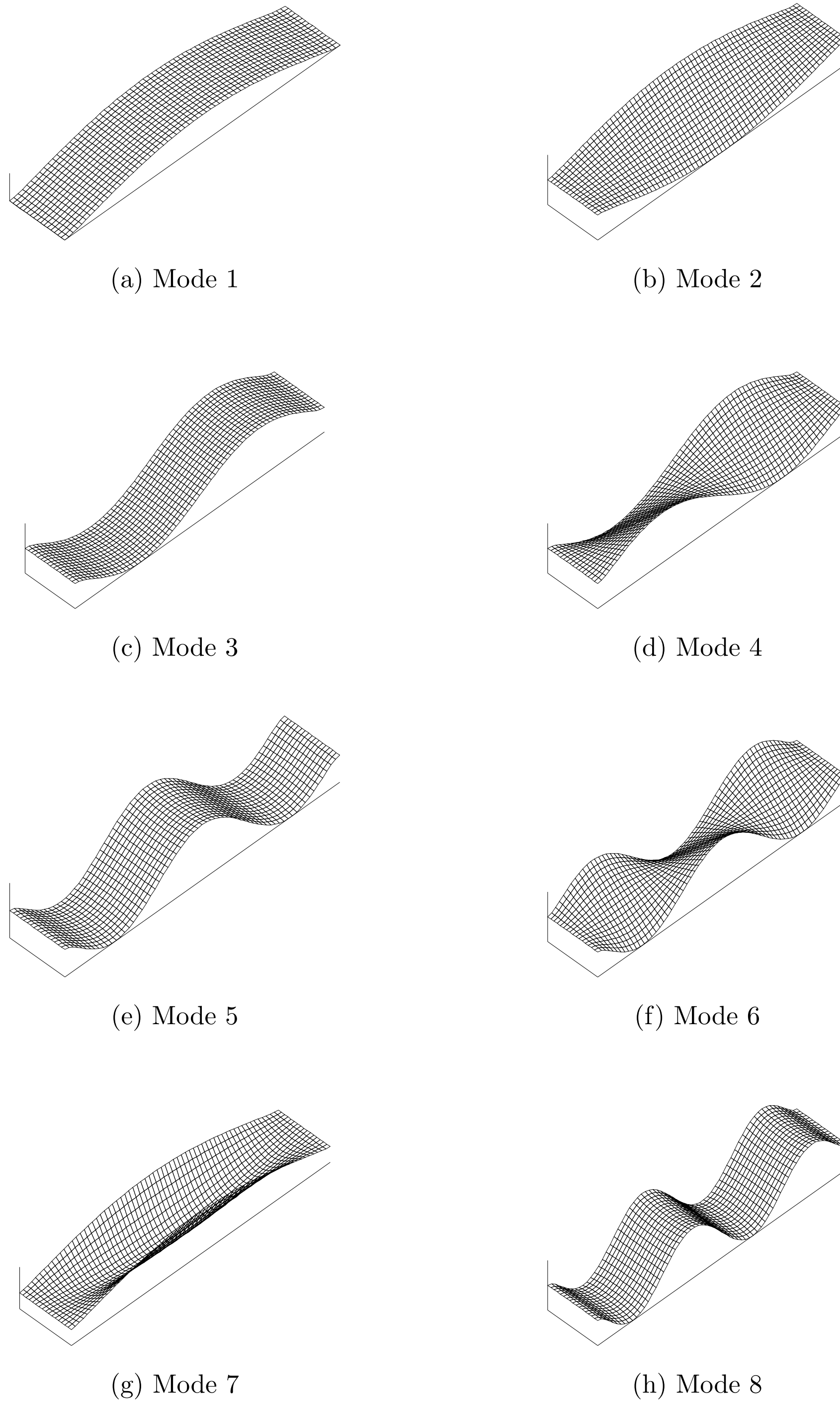

(a) Mode 1 (b) Mode 2

(c) Mode 3 (d) Mode 4

(e) Mode 5 (f) Mode 6

(g) Mode 7 (h) Mode 8

Figure 4.4. Model structure undamped dynamic mode shapes 1–8

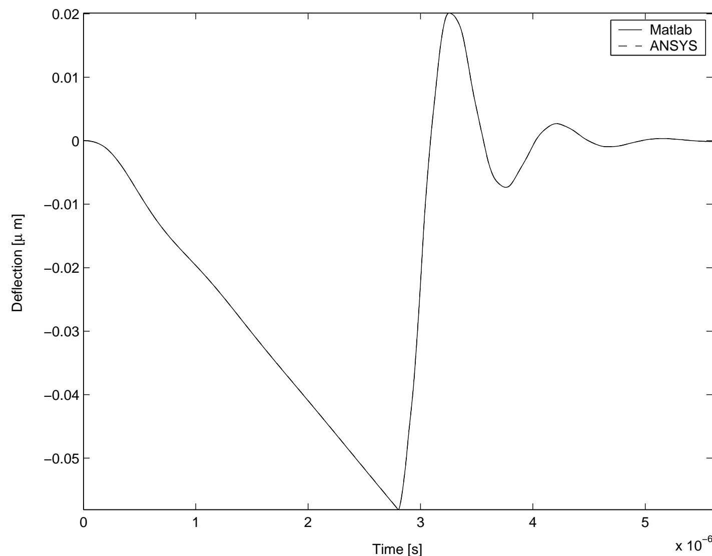

Figure 4.5. Model structure dynamics comparisons ($\sigma_0 = 0$)

4.5. Quasi–static static limit comparison

Lowering the initial material stress in the Silicon Nitride (σ_0) to 850MPa the test structure is subjected to a static limit test, where the applied voltage ramps from $0 \rightarrow 25$V in 25µs followed by a return to 0V in a further 25µs. Examining the centerline profile ($x = 3$µm) of the structure at 16, 18, 20 and 22V under both increasing and decreasing voltages provides the comparisons illustrated in Figure 4.6. The solid lines are centerline profiles from the full dynamic simulation of the test structure and the dashed lines are obtained using information provided by Kowarz et al. [2002] from a quasi-static model. Generally, the agreement is adequate, however the comparison does highlight the deficiencies of the quasi-static model. The quasi-static model is unable to model points of zero rotation, due to the removal of the bending contribution to stiffness. Thus, the quasi-static model does not capture the fixed end conditions or the point of symmetry at mid-span correctly. The differences in contact criteria are also apparent, the quasi-static model expresses the underlying standoffs as a single surface while the full dynamic model possesses discrete structures and allows the ribbon to drape over the standoffs. The test structure does not posses standoffs along the ribbon unit center line, as seen in Figure 4.2, and no contact with the oxide layer occurs during the static limit test.

Electromechanical hysteresis is observed during device operation and in Figure 4.6, Figure 4.7 illustrates the dynamic voltage deflection behaviour of the

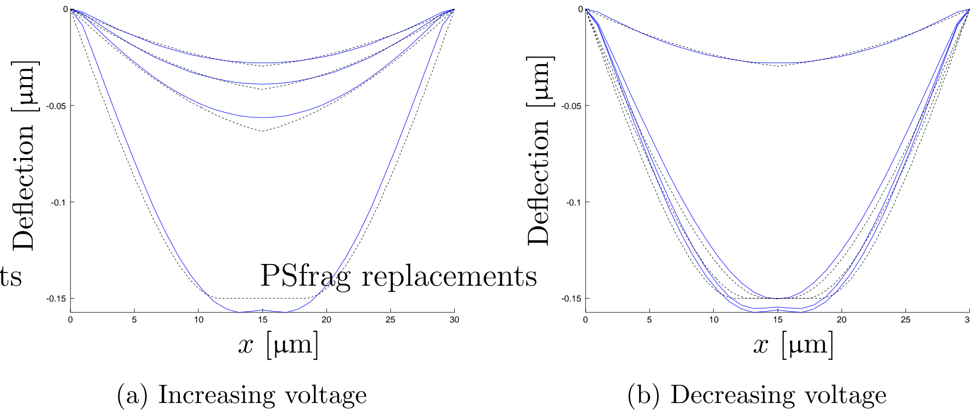

(a) Increasing voltage (b) Decreasing voltage

Figure 4.6. Model structure profile comparisons

center point of the test structure during the static limit simulation. Arrowheads have been added to illustrate the direction of movement around the hysteresis loop as the voltage rises and falls. The quasi-static model also does not capture the ringing observed when the device releases, as it has no dynamics. It is expected that this ringing will significantly impact the device's optical performance in switching applications.

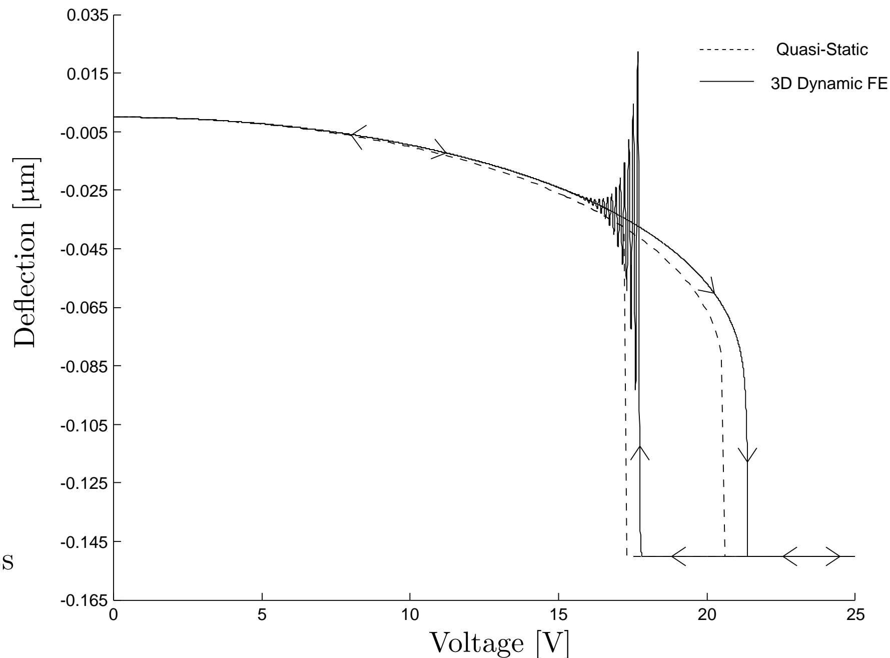

Figure 4.7. Test structure, quasi-static hysteresis comparisons

Comparing the pull down (V_{PD}) and release (V_{RL}) voltages from the two

models, Table 4.6 highlights the efficiency of the string models. With the reported

Table 4.6. Critical voltage comparison

Critical Voltage	Dynamic 3D	Quasi–static 2D
Pull Down (V_{PD})	21.38	21.14
Release (V_{RL})	17.80	17.57
Difference (ΔV)	3.58	3.57

values showing very good agreement. The slightly lower quasi-static values are likely due to the damping and inertia in the dynamic model.

Chapter 5

Trade-off Analyses

Utilizing the modelling approach validated in Chapter 4 the sensitivity of the GEMS ribbon unit to variations in key parameters is assessed. The GEMS ribbon unit design space is bounded by multiple variables exhibiting varying degrees of coupling. Thus, simulating variations in a single parameter from a stated reference configuration is the only computationally feasible approach given the timeframe of this research.

In consultation with Eastman Kodak staff the parameters varied include:

- Slew rate, the rate at which the voltage is applied and removed
- The post-deposition initial material stress in the Silicon Nitride layer (σ_0)
- Thickness, the thickness of the Silicon Nitride layer ($t_{Si_3N_4}$)
- Standoff layout, the distribution of standoffs, spacing in both directions (s_x & s_y, Figure 5.1) and the thickness of the standoff layer ($t_{Standoffs}$), hence the height of the standoffs.

These variables are the parameters most likely to vary significantly across a wafer, between wafers or as a result of driving input signals. Such variations can cause device failure or result in devices with dynamic behaviour outside desired operating limits.

Of interest during these studies are the pull down (V_{PD}) and release (V_{RL}) voltages of the structure, and how they vary with changes in parameters. The design intent of the standoffs in the GEMS ribbon unit is the mitigation of contact between the ribbon and the oxide layer, lessening the probability of stiction and device failure. Thus, the incidence of contact between the ribbon unit and the oxide layer is of interest, as are the stresses in the ribbon during operation.

5.1. Reference ribbon unit configuration

The reference configuration for the GEMS ribbon unit is an $8 \times 30\mu m$ ribbon. Figure 5.1 depicts a full finite element mesh of this reference configuration and identifies the critical dimensions listed in Table 5.1. The mesh represents the location of the ribbon mid plane and the shaded regions beneath the mesh represent the location of the standoffs. When the mesh meets the standoffs or oxide layer, the node at which the meeting occurs is considered in contact. The dashed lines, in Figure 5.1, are construction lines and indicate the vertical (z) location of the underlying standoffs. The position of the upper surface of the standoffs is

g replacements

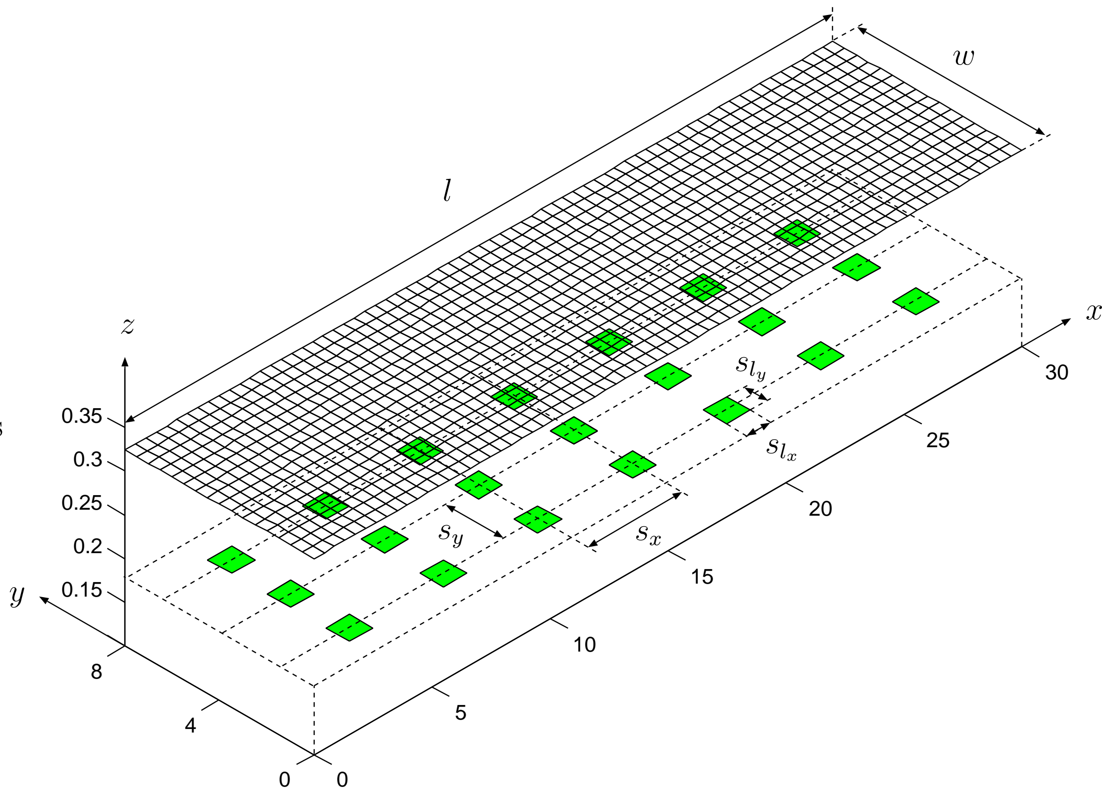

Figure 5.1. Reference ribbon unit layout

the height at which the ribbon makes contact not the actual location. The true location is one half a ribbon thickness below the illustrated position, where the additional half a ribbon thickness accounts for the thickness of the real ribbon structure.

Section 4.3 highlights the efficiency of the hybrid stress element formulation in accounting for the stiffness of structures using coarse meshes. Thus, the suitability of a coarse (8×34) element mesh was evaluated against a fine (16×68)

Table 5.1. Reference ribbon unit parameters

Parameter	Value	Units
Length (l)	30	µm
Width (w)	8	µm
Thickness ($\tilde{t}$, Equation 3.1)	0.12	µm
t_{Al}	0.05	µm
$t_{Si_3N_4}$	0.1	µm
t_{A_0}	0.15	µm
t_{Oxide}	0.05	µm
Youngs modulus (E)	250	GNm^{-2}
E_{Al}	70	GNm^{-2}
$E_{Si_3N_4}$	250	GNm^{-2}
Poissions ratio (ν)	0.33	
Density ($\tilde{\rho}$, Equation 3.2)	3826	kgm^{-3}
ρ_{Al}	2710	kgm^{-3}
$\rho_{Si_3N_4}$	3180	kgm^{-3}
Initial stress ($\tilde{\sigma_0}$, Equation 3.3)	928	MNm^{-2}
$\sigma_{0_{Si_3N_4}}$	1100	MNm^{-2}
$\sigma_{0_{Al}}$	0	MNm^{-2}
Standoffs		
Rows	3	
$t_{Standoffs}$	0.05	µm
s_y	2.5	µm
s_x	4	µm
s_{l_x}	1	µm
s_{l_y}	1	µm

mesh. Recall that Figure 5.1 depicts a full 16×68 finite element mesh. Figure 5.2 illustrates the modelled regions of the the two meshes, when symmetric model reduction considerations are applied. The two meshes presented in Figure 5.2

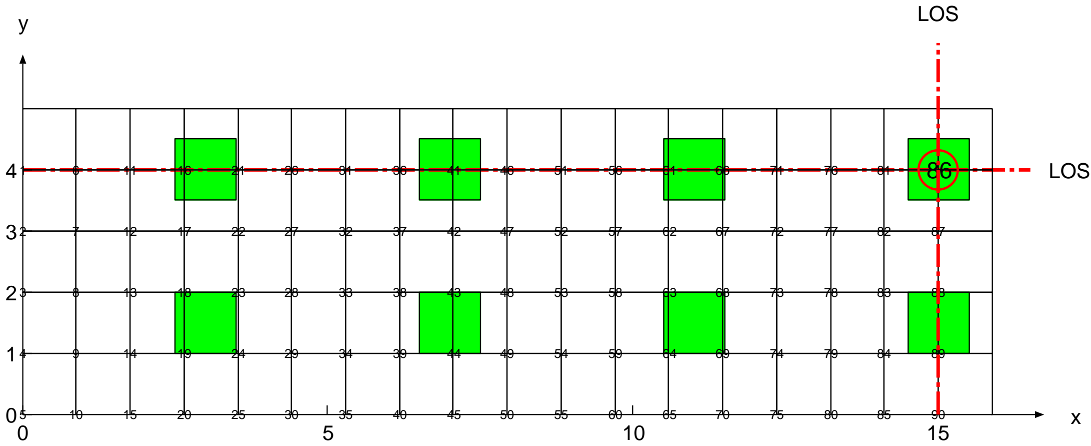

(a) Coarse mesh (08×34 elements)

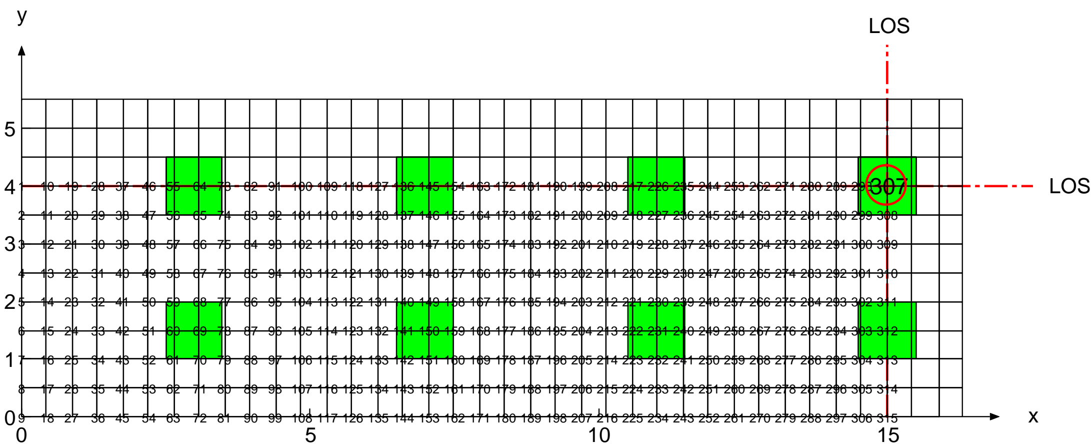

(b) Fine mesh (16×68 elements)

Figure 5.2. GEMS ribbon unit model mesh densities, showing node numbers

show one quarter of the ribbon unit, and the red dashed lines indicate the lines of symmetry (LOS) within the structure. The first eight natural frequencies of the reference structure are listed in Table 5.2, and are identical for the two mesh densities.

Altering σ_0 and $t_{Si_3N_4}$ alter the inherent structural characteristics of the ribbon unit. Thus the mode shapes and frequencies must be computed for each of the simulation cases, in the σ_0 and $t_{Si_3N_4}$ families of simulations, to determine

an efficient base time step. As discussed in Section 2.3 the first ten modes of operation are deemed as significant contributors to device response, so the initial time step size for the reference simulation configuration is 2.8×10^{-9}s.

Table 5.2. Reference structure natural frequencies

Mode	Frequency (MHz)
1	8.56
2	8.92
3	17.22
4	17.93
5	19.18
6	26.02
7	26.06
8	27.12
9	34.70
10	35.18

Using this initial time step size and subjecting the reference ribbon unit configuration to the static limit test, $0 \rightarrow 24 \rightarrow 0$V in 50µs, causes the ribbon unit to bifurcate as expected. The electromechanical hysteresis of the center point of the ribbon unit (Node 86 in Figure 5.2(a) and Node 307 in Figure 5.2(b)), is illustrated in Figure 5.3. The two lines represent the response of the two mesh densities and arrow heads have been added to indicate the traversal of the loop. The agreement obtained is excellent for the two mesh densities. The most pertinent feature of Figure 5.3 is the high frequency oscillation that occurs as the ribbon breaks contact with the standoffs. Also of interest is the small oscillation observed prior to the release bifurcation for the fine (16×68) mesh, circled with a dashed line in Figure 5.3, resulting from the redistribution of the applied load as contact is lost with all standoffs but the center row. The absence of the small pre-release oscillation from the hysteresis response of the coarse element mesh confirms that the coarse mesh does not sufficiently capture the localized dynamics of the GEMS ribbon unit.

Traversing this hysteresis loop the reference ribbon unit is observed to bifurcate between the two characteristic stable states, as discussed in Section 2.5.1. The voltages at which these bifurcation points occur are tabulated in Table 5.3.

The reference configuration static limit simulation yields the runtime profile illustrated in Figure 5.4, where the stepped upper line plotted on the left hand

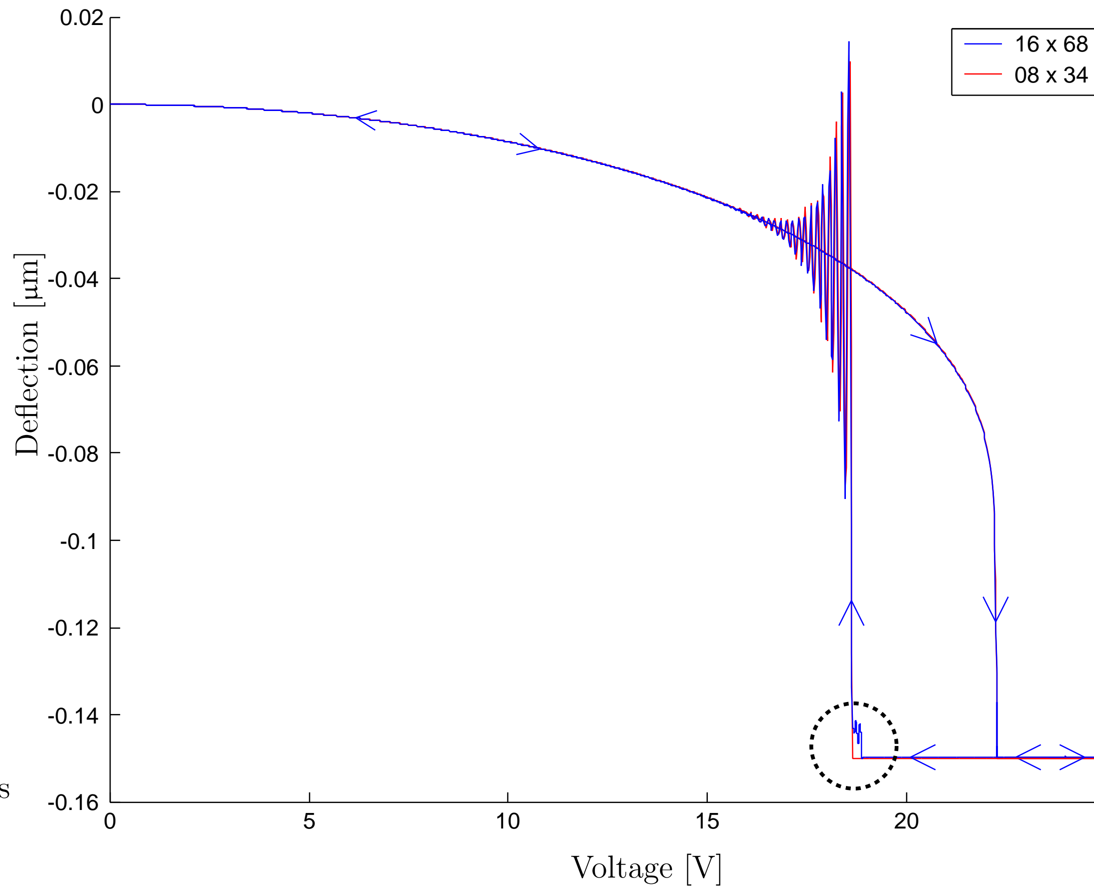

Figure 5.3. Reference simulation electro-mechanical hysteresis trace

Table 5.3. Critical voltages for reference simulation

	V_{PD} [V]	V_{RL} [V]	ΔV [V]
Reference	22.28	18.67	3.61

axis represents the number of nodes that are in contact with either the oxide layer or the standoffs in any given time step. The jagged lower line plotted on the right hand axis is the current time step size in the simulation. The presence of a second dashed line (also plotted on the left hand axis) indicates the number of nodes in contact with the oxide layer during each time step, however for the reference simulation no contact with the oxide layer occurs. The vertical dotted lines indicate simulation block boundaries. As nodes come into contact it is

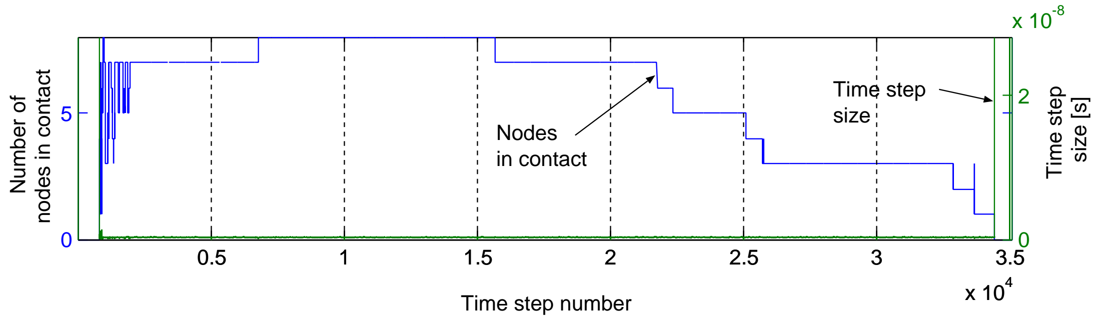

Figure 5.4. Reference simulation runtime profile

anticipated that the time step size decreases to ensure penetration is controlled. As expected the time step size does not reduce until contact first occurs. While in contact the time step size remains small and is barely visible in Figure 5.4.

The runtime profile provides an index to the simulation and highlights areas of interest that require investigation. Figure 5.4 illustrates the “zipping” phenomena, where the ribbon unit makes contact with the first standoffs, at mid span, and quickly “zips” into the second stable structural configuration. The steps in the number of contacted nodes between step 1000 and step 2000 of the simulation indicate the presence of structural oscillations post pull down and it is likely that such oscillations that cause the oscillations in reflected light intensity of Figure 5 Kowarz et al. [2002].

The decreasing steps from step 15000 to 35000 are the the gradual release of the ribbon as the voltage is reduced. The short increasing step before step number 35000 is the ribbon unit redistributing the decreasing load on the edge standoffs causing a momentary increase in contact. This increase causes the center node of the model to release which is manifested in Figure 5.3 as the small pre-release oscillations.

During the static limit simulation the reference ribbon unit is not observed to contact the oxide layer. The minimum separation between the lower surface

of the ribbon and the upper surface of the oxide layer, of 0.040μm, occurs at $x = 12.794\mu m$, $y = 0\mu m$ when the applied voltage is 22.28V. The point that attains this minimum separation is situated between two standoffs where the ribbon unit is least constrained. Table 5.3 indicates that this voltage value is the pull down voltage (V_{PD}). Thus, the ribbon unit comes closest to the oxide layer during "zipping" and not when the structure is subject to the peak voltage of 25V. This result suggests that the inertial dynamics of the structure are more important than the applied voltage for locating contact, invalidating all modelling approaches that do not consider the dynamics of the structure.

While the agreement between the modal analysis and hysteresis results for the two mesh densities is striking, the coarse mesh (8×34) does not fully incorporate the effects of the upper standoff surfaces into the model, as the contact model adopted uses point contact with nodes in the finite element mesh. The absence of nodes overlapping the edges of the standoffs causes the coarse mesh to over predict sagging beneath the standoffs. Subsequently, all ribbon unit parameter variations utilise the fine (16×68 element) mesh. All simulations are modelled using one quarter of the full finite element mesh for the GEMS ribbon unit reducing computational costs with reassembly and initial material stress contributions to applied forces ($\{q\}$) disabled. The computational requirements of the simulations are listed in Table C.1 of Appendix C.

Using Equation (2.36) the diffractive efficiency (η_m) of the reference GEMS ribbon unit configuration may be calculated. Equation (2.36) assumes a planar device, thus the finite element discretization may be used to compare the diffractive efficiency of each row of nodes along the models length. As symmetry has been utilized in the modelling of the GEMS ribbon unit only the rows of nodes at the ribbon unit edge (0), ribbon unit quarter line ($\frac{w}{4}$) and ribbon unit centerline ($\frac{w}{2}$) are illustrated in Figure 5.5. Figure 5.5 illustrates the diffractive efficiency for collected 0th order light for the reference GEMS ribbon, with;

$$\Lambda = 36\mu m$$
$$\lambda = 532nm$$

Figure 5.5 clearly illustrates the influence of the post realease oscillations on optical performance and compares extremely favourably with the experimental data illustrated in Figures 5a and b of Kowarz et al. [2002]. The variation in diffractive efficiencies for collected 0th order light do not vary significantly across the width of the GEMS ribbon unit, $\leq 1\%$, as the order of collected light is

PSfrag replacements

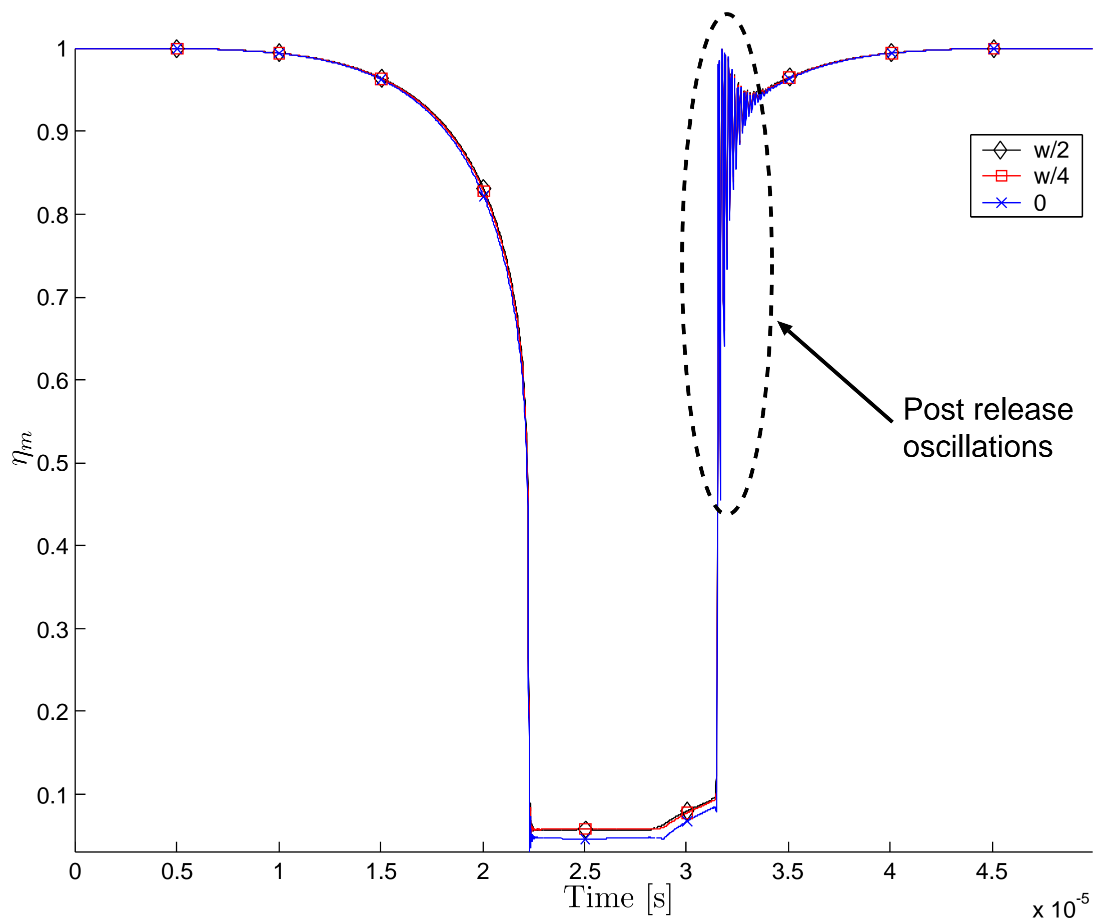

Figure 5.5. Reference simulation diffractive efficiencies

increased the difference becomes more significant, $\approx 5\%$ for second order light.

Unlike Figure 5.3, the diffractive efficiency of the GEMS ribbon illustrates the distributed nature of the deformation of the structure with time. Clearly showing the post-contact oscillations and the pre-release deformation reduction. Figure 5.6 is a magnification of Figure 5.5 illustrating these two behaviours.

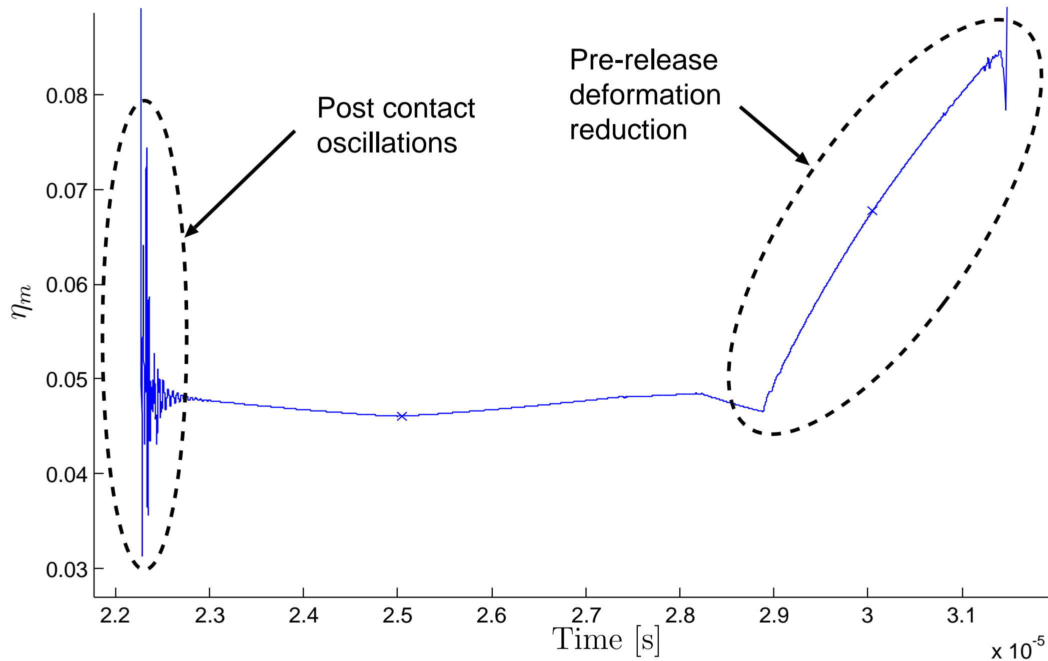

Figure 5.6. Reference simulation diffractive efficiency details

The reference ribbon unit configuration is the standard from which each family of simulations varies a single parameter and catalogues the changes in the operation of the ribbon unit. In the subsequent parameter variations the hysteresis results are compared to the reference configuration, plotted using a dashed line with "x" markers. The reference configuration voltages are tabulated with the results of each family of simulations.

5.2. Slew rate

Varying the time in which the voltage ramp is applied to the structure allows changes in device response to be observed, for different operating profiles. The static limit test applies the voltage ramp slowly (in 25μs). However the slew rate tests aim to test the dynamics of the structure beyond what is currently possible with existing Kodak models, highlighting the ability of this finite element approach to capture the dynamics of the device where current, quasi-static, models fail.

The specification for the slew rate tests requires a modified voltage profile of, $0 \rightarrow 24$V in the specified slewing time. The voltage is then held for a period of 2 μs and then ramped back to zero in the specified slewing time. This approach differs from the static limit test where the voltage is ramped to 25V in 25μs and then back to 0V in a further 25μs. The waiting period is to allow an observation of any transient dynamics present in the ribbon unit's response.

The five slewing times simulated are: 300ns, 200ns, 100ns, 50ns and 20ns. Figure 5.7(a) compares the length of the 300ns slew rate simulation to the static limit test, showing that the slew rate simulations are significantly shorter in duration, and are therefore expected to run in significantly reduced time. These reduced slewing times were chosen in consultation with Eastman Kodak. Figure 5.7(b) outlines the profiles of the different slew rate simulations.

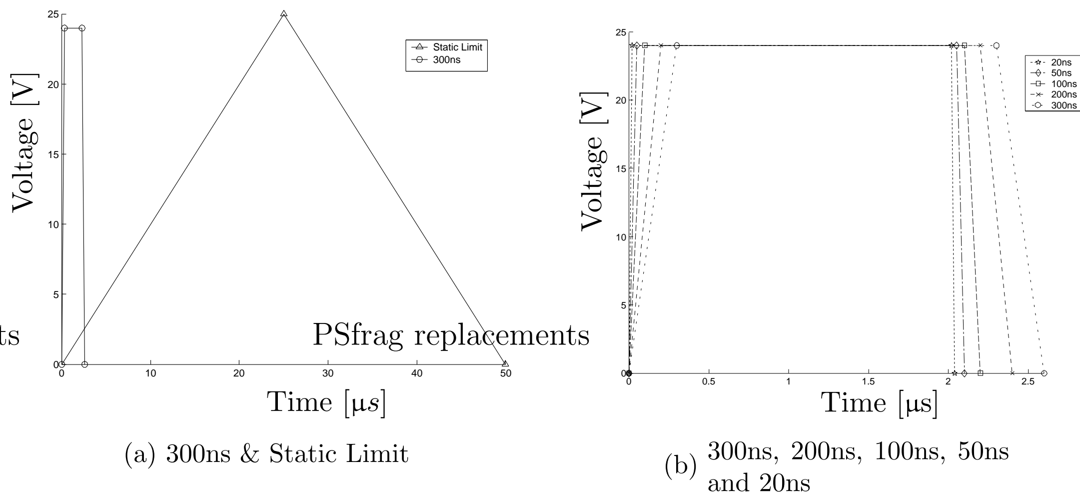

(a) 300ns & Static Limit

(b) 300ns, 200ns, 100ns, 50ns and 20ns

Figure 5.7. Slew rate simulation voltage profiles

Figure 5.8 shows the hysteresis profiles for the slew rate simulations, including

the hysteresis loop of the reference configuration (dashed) for comparison. As the switching speed increases, the slewing time is reduced and the structure has less time to respond. The electro-mechanical hysteresis loop becomes less well formed and the sharp distinction at the bifurcation points is lost. Removing the voltage

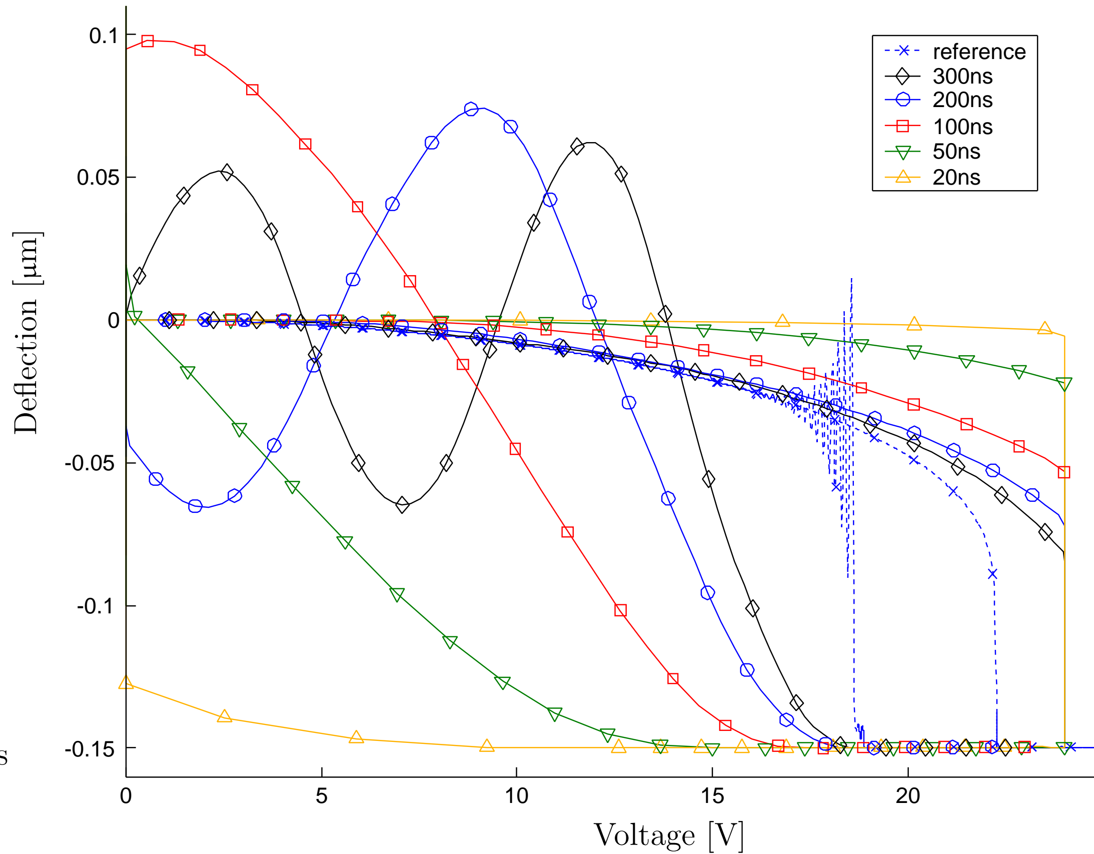

Figure 5.8. Hysteresis curves for slew rate simulations

ramp quickly, removes the ability to control the post release oscillations of the GEMS ribbon unit. Figure 5.8 shows that the unit oscillates in lightly damped free vibration. This result contrasts the results of the static limit simulation where the voltage reduction was managed, allowing maximum control over the magnitude of the post release oscillations. A quasi-static approach to modelling, where the dynamics of the structure are ignored, is unable to capture any such behaviours.

When the voltage reaches zero the ribbon is observed to oscillate in damped free vibration until it comes to rest. In Figure 5.8 this oscillation occurs at 0V and is obscured by the vertical axis. Clearly, the higher the slew rate the greater the initial displacement, and the more time required for the oscillations to damp

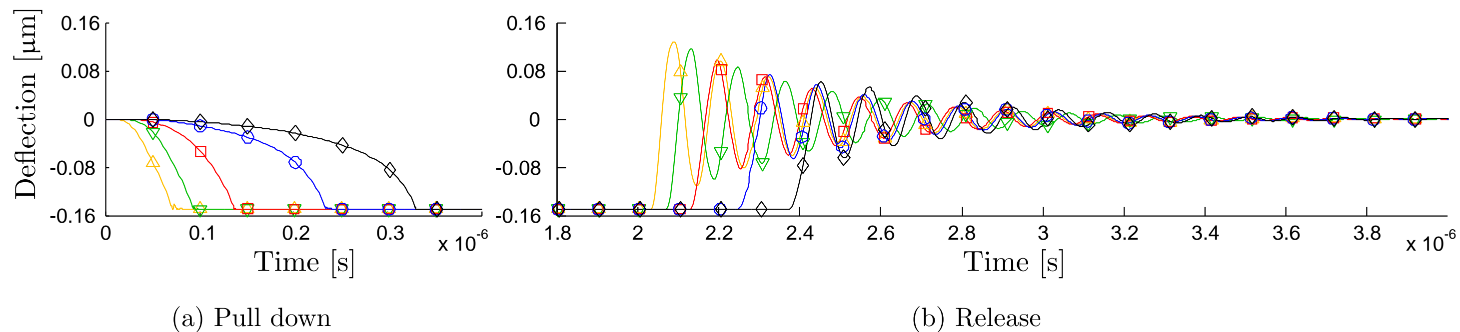

Figure 5.9. Slew rate simulation time deflection profiles (Legend as in Figure 5.8)

out. Figure 5.9 illustrates the time deflection behaviour of the center of the GEMS ribbon unit with time, removing the coupling between applied voltage and time. Figure 5.9(a) illustrates the time dependance of ribbon unit pull down and Figure 5.9(b) illustrates the decay in the post release oscillations as the slew rate is reduced. Figure 5.8 indicates that reducing the slewing time results in increases in the magnitude of the post release oscillations. This observation is reasonable as reducing the slewing time increases the rate at which the applied voltage is removed, diminishing any controling influence experienced by the GEMS ribbon unit.

All simulations utilize a damping model in which 5% of critical damping has been placed in modes one and ten. This is consistent with the exponential decay envelope observed in the post release oscillations in Figure 5.9(b).

As the slew rate is increased, and the switching time reduced, the magnitude of the post release oscillations increase. This result follows as the voltage ramp returning to zero has a lessened effect, as it is removed more quickly. Hence, greater peak amplitude in the oscillations and reduced control.

From Figure 5.8 the critical operating voltages of the structure can be determined and Table 5.4 lists these values. Table 5.4 shows that as the slew rate is

Table 5.4. Critical voltages for slew rate simulations

Case	V_{PD} [V]	V_{RL} [V]	ΔV [V]
Reference	22.28	18.67	3.61
300ns	24	18.27	5.72
200ns	24	18.24	5.76
100ns	24	17.35	6.64
50ns	24	15.01	8.99
20ns	24	12.61	11.39

increased, the GEMS ribbon unit is unable able to respond in sufficient time and the ΔV increases.

Figure 5.10 presents the number of nodes in contact during each time step. In contrast to Figure 5.4 the "zipping" oscillations are more pronounced and the gradual reduction in contact as the ribbon releases is not as pronounced as in Figure 5.4.

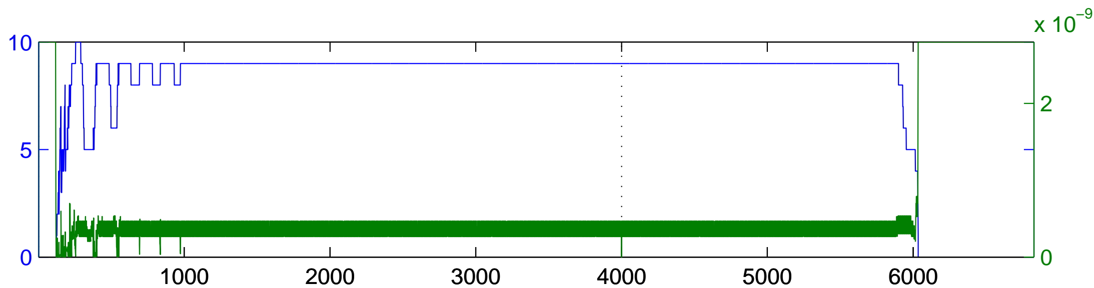

(a) 300ns

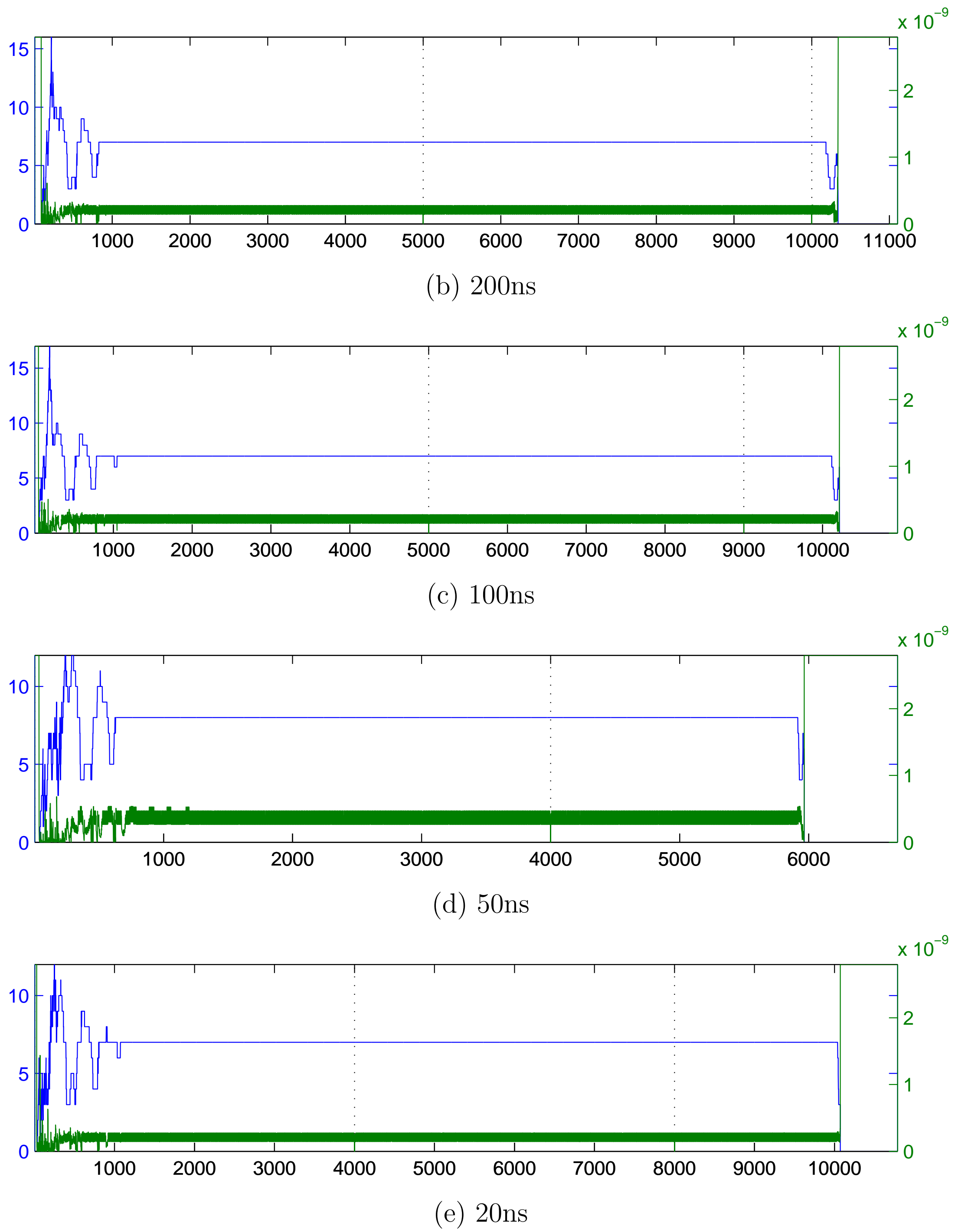

(b) 200ns

(c) 100ns

(d) 50ns

(e) 20ns

Figure 5.10. Slew rate simulation runtime profiles

As the slewing time is reduced release occurs more quickly as observed in the steepening gradient of the release steps and the sharp rise in the time step size.

During the slew rate simulations no contact with the substrate occurs, however as Table 5.5 illustrates, decreasing the slewing time decreases the minimum separation between the bottom of the ribbon and the top of the oxide layer.

Table 5.5. Minimum electrode separations for slew rate simulations

Case	Separation [μm]	Time [s]	Voltage [V]	x [μm]	y [μm]
Reference	0.040	2.23×10^{-5}	22.28	12.79	0
300ns	0.035	3.34×10^{-7}	24	12.79	0
200ns	0.033	2.38×10^{-7}	24	12.79	0
100ns	0.032	1.41×10^{-7}	24	12.79	0
50ns	0.031	9.74×10^{-8}	24	12.79	0
20ns	0.027	7.56×10^{-8}	24	13.24	0

As expected, Table 5.5 shows that decreasing the slewing time reduces the time taken for the ribbon unit to achieve minimum separation. However, as the slew rate test structures respond in a less timely manner than the reference structure the voltage at which minimum separation occurs is always the peak voltage in the test. Removing the slewing time from the time taken to achieve minimum separation reveals that as the slewing time is reduced the time taken to achieve minimum separation while at peak voltage increases, emphasizing more static behaviour.

The slew rate simulations have shown that activation switching speeds place no limit on the voltage at which the ribbon unit bifurcates to the second stable structural state, as the required load is defined by the structural characteristics of the ribbon unit. The slew rate simulations have also shown that there exists an inherent limit in how fast the structure can respond to the applied load. Attempting to activate the ribbon unit more quickly does not result in any performance gain, and in fact V_{PD} increases to an almost constant 24V, a behaviour that can be characterised as static. In contrast, reducing the time taken to remove the voltage results in diminished control over the ribbon units behaviour at release when the ribbon unit oscillates in undamped free vibration. The magnitude and duration of these oscillations have been shown to be a function of the voltage removal rate, because a higher post release voltage more successfully inhibits the post release oscillations.

5.3. Initial material stress

The initial material stress (σ_0) in the Silicon Nitride layer exerts significant influence over the dynamic frequencies of the GEMS ribbon unit and can be controlled by adjusting the stoichiometry in the silicon nitride layer, as suggested by Solgaard [1992]. The presence of the initial material stress is a side-effect of the chosen deposition process and its specific parameters [Madou, 1997]. Adjusting the stoichiometry of the Silicon Nitride layer enables large changes in the natural frequencies of the ribbon unit for little change in structural mass. Thus, tuning the response of the ribbon unit by altering the initial material stress is an appealing approach to changing the performance of the device. It is also an avenue where variations in fabrication can cause undesired variations in dynamic performance.

For the reference GEMS ribbon unit the relationship between the fundamental natural frequency of the structure (ω_1) and the initial material stress is illustrated in Figure 5.11, where the upper triangular markers represent the results of modal analysis results and the solid line the fitted curve. Figure 5.11

PSfrag replacements

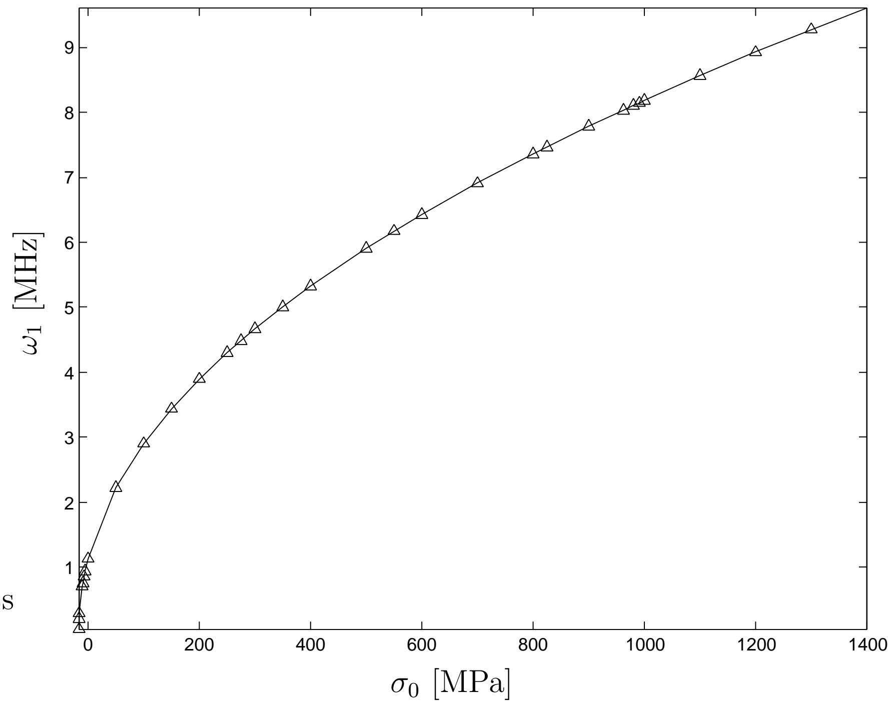

Figure 5.11. Fundamental frequency variation with initial material stress

indicates that assuming a linear variation in fundamental frequency in the region surrounding the Kodak quoted initial material stress value (1100MPa) is ade-

quate for design purposes. However, such an assumption breaks down at lower initial material stresses such as those used for the Grating Light Valve [Bloom et al., 1994].

The negative initial material stress values in Figure 5.11 suggest that a small compressive load (> 16MPa) would cause the GEMS ribbon unit to buckle. A likely cause of such compressive loading is thermal expansion due to heating of the ribbon materials. Thus, investigation of operating temperatures of the device is suggested in order to eliminate this possible failure mechanism. In GEMS devices the compressive thermal stress must first overcome the initial tensile material stress to cause buckling. Therefore, the problems caused by induced compressive loads are most likely in devices with low tensile initial material stresses.

While the effect of the initial material stress on device frequencies is well understood the interaction with V_{PD} and V_{RL} is not intuitive. Figure 5.12 displays the static limit hysteresis curves for GEMS ribbon units with initial material stresses in the Silicon Nitride layer of 1100MPa, 962MPa (87.5%), 825MPa (75%), 550MPa (50%) and 0MPa. The variation in fundamental frequency of the ribbon

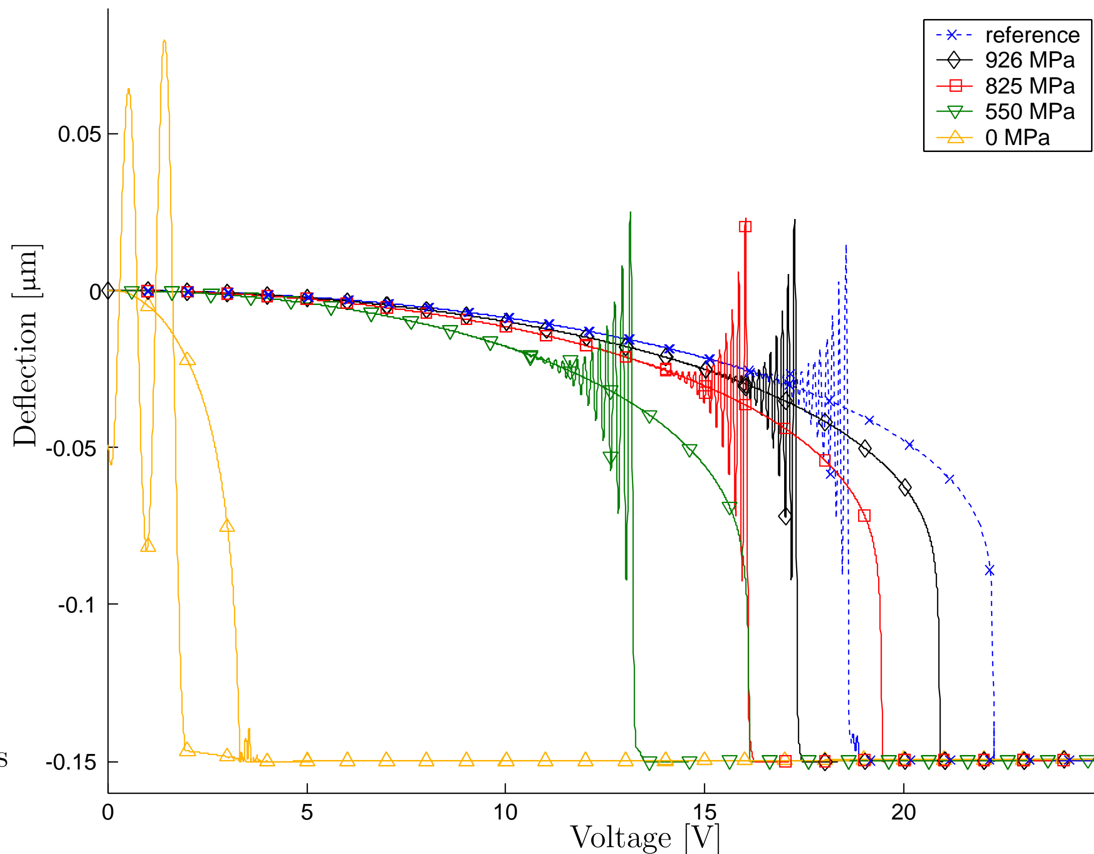

Figure 5.12. Hysteresis curves for initial material stress simulations

unit is apparent in Figure 5.12. As the initial material stress is reduced, the fundamental frequency drops and the frequency of oscillation on release decreases. In Figure 5.12 this result manifests as a frequency decrease in the post release oscillations.

The change in magnitude of the post release oscillations, expected as V_{RL} reduces, is offset by the reduction in stiffness contributed by the initial material stress. Resulting in no changes in the height of the peak post release oscillations in Figure 5.12.

Removing the initial material stress ($\sigma_0 = 0$MPa) the ribbon unit retains the electro-mechanical hysteresis and bifurcating behaviours. However, the resulting drop in fundamental frequency causes the unit to oscillate in damped free vibration beyond the conclusion of the static limit test. The tan line (upper triangular markers) in Figure 5.12 illustrates the hysteresis of the ribbon unit without initial material stress. The reduction in stiffness also significantly advances the location of both the bifurcation points. Therefore, variation across an array will lead to variable dynamic behaviour which can be undesirable if switching occurs over a limited (ΔV) voltage range, as illustrated in Figure 1.1.

The variations in location of the bifurcation points with initial material stress are listed in Table 5.6. The voltages listed in Table 5.6, indicate that reducing

Table 5.6. Critical voltages for initial material stress simulations

Case	ω_1 [MHz]	V_{PD} [V]	V_{RL} [V]	ΔV [V]
Reference	8.56	22.28	18.67	3.61
962	8.03	20.92	17.38	3.54
825	7.47	19.47	16.16	3.31
550	6.17	16.10	13.22	2.88
0	1.13	3.31	1.95	1.36

the initial material stress in the Silicon Nitride layer reduces the operating ΔV of the ribbon unit in addition to advancing the bifurcating points. This reduction results from the effect of initial material stress on the stiffness of the device, where a reduction in stiffness causes earlier bifurcation and retards release due to the reduction in the mechanical restoring ability of the ribbon.

The runtime profiles for the initial material stress simulations are presented in Figure 5.13. The significant stepped increase in the number of nodes in contact as the voltage on the unit is reduced is observed in all simulations, but is most

significant in the simulations with the greater initial material stress. This result is due to the change in ribbon curvature as the number of nodes in contact reduces.

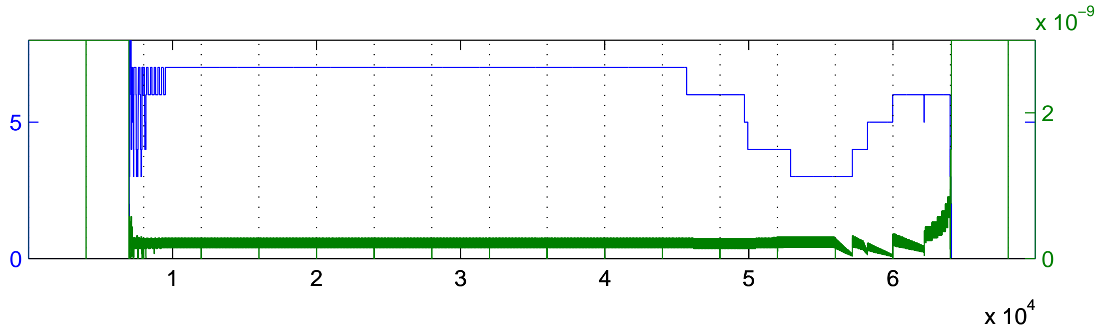

(a) $\sigma_0 = 962\text{MPa}$

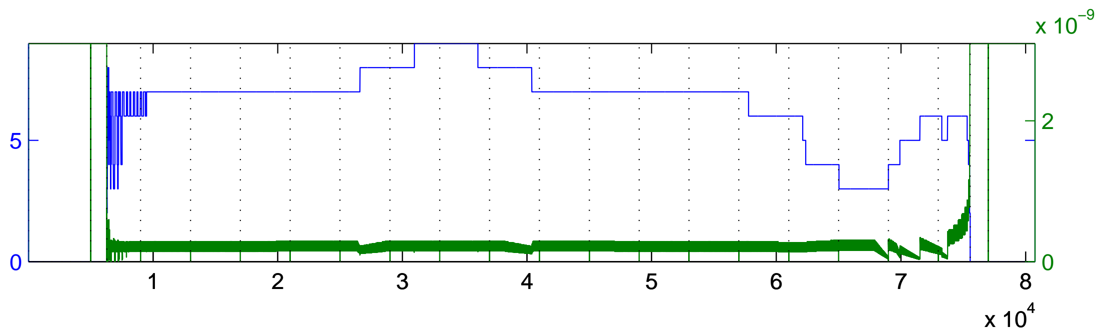

(b) $\sigma_0 = 825\text{MPa}$

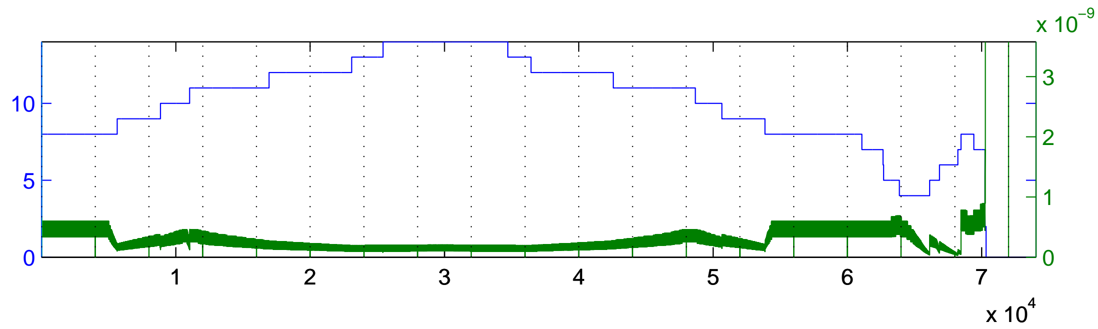

(c) $\sigma_0 = 550\text{MPa}$

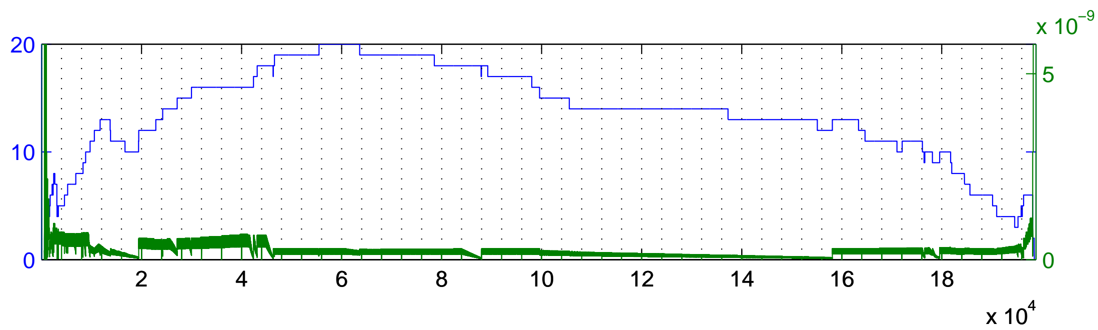

(d) $\sigma_0 = 0\text{MPa}$

Figure 5.13. Initial material stress simulation runtime profiles

Figure 5.13 also highlights the increase in computational requirements as the stiffness of the ribbon unit is reduced. As the stiffness is reduced the number of computational blocks boundaries denoted by vertical dashed lines increases. Thus, the simulations require more computational time to run and occupy more storage space when completed. Table C.1 in Appendix C lists the computational requirements of all completed simulations.

Table 5.7 lists the minimum separation between the lower surface of the ribbon and the oxide layer. As the initial material stress is reduced the minimum separation increases, indicating a possible whip mechanism where the initial material stress causes the ribbon to deform closer to the oxide layer. However as the initial material stress continues to fall the reduced stiffness allows increased deformation and the minimum separation decreases.

Table 5.7. Minimum electrode separations for initial stress simulations

Case	Separation [μm]	Time [s]	Voltage [V]	x [μm]	y [μm]
Reference	0.03967	2.23×10^{-5}	22.28	12.79	0
962 MPa	0.04136	2.09×10^{-5}	20.93	12.79	0
825 MPa	0.04221	1.95×10^{-5}	19.47	12.79	0
550 MPa	0.03898	2.30×10^{-5}	23.00	8.82	0
0 MPa	0.03861	2.50×10^{-5}	25.00	12.79	0

Altering the initial material stress in the Silicon Nitride provides the ability to alter the stiffness of the GEMS ribbon unit without significantly changing the mass. Traditional methods for altering stiffness, require the addition or removal of material, causing large changes in the operating frequencies of the structure. The ability to alter the bifurcation points with less impact on the frequency of the GEMS ribbon unit needs to be assessed.

Reducing the initial material stress results in a decrease in ΔV, as both bifurcation voltages are observed to decrease. However, V_{PD} reduces more rapidly than V_{RL} resulting in the overall decrease. Removing the initial material stress from the GEMS the ribbon unit, with a reference standoff pattern, does not advance the onset of contact with the oxide layer. However, such a significant reduction in unit stiffness advances pull down and release, while decreasing the frequency of oscillation on release, which may be desirable.

5.4. Ribbon thickness

Section 5.3 addresses the variation of initial material stress on the performance of the GEMS ribbon unit and examines the results of varying a single parameter. Varying the thickness of the Silicon Nitride layer ($t_{Si_3N_4}$) of the GEMS ribbon unit has three effects on the structure due to the coupling of the bounding parameters. The complex changes that occur in the ribbon unit as a result of variations in the thickness of the Silicon Nitride layer include:

- Modification of the cross-sectional area of the structure that is subject to the initial material stress, thus reducing the effect of the initial material stress on the bending stiffness of the device
- Altering the "natural" stiffness of the ribbon unit as bending stiffness is dependent on the thickness of the layers
- Changing the initial electrode separation. Because the GEMS device is fabricated in layers changing the thickness of an intermediate layer effects the position of all layers above.

Such variations in thickness can arise due to variation in the thickness across a deposited layer or changes in unit cross section due to variation in the effectiveness of the etchant fabrication steps.

The effect Silicon Nitride layer thickness ($t_{Si_3N_4}$) on the fundamental frequency (ω_1) of the GEMS ribbon unit is illustrated in Figure 5.14. As the GEMS ribbon is a composite structure formed from two layers, gaining significant characteristics from the Silicon Nitride layer, it is inconceivable that this layer be removed entirely from the design. Thus, the minimum modelled value of 5nm was adopted.

Figure 5.15 depicts the variation in static limit test hysteresis that occurs as the thickness of the Silicon Nitride layer is altered. As the thickness of the Silicon Nitride layer is reduced, the ribbon unit becomes more flexible, resulting in a decrease in V_{RL} and an increase in the peak magnitude of the post release oscillations.

From Figure 5.15 50nm thickness for the Silicon Nitride represents an edge of the design space as the ribbon unit does not release in the expected manner due to the significant portions of the ribbon unit in contact with the oxide layer. The resulting inverted "u" profile acts to increase the effective width of the point source formed by the activated GEMS ribbon unit.

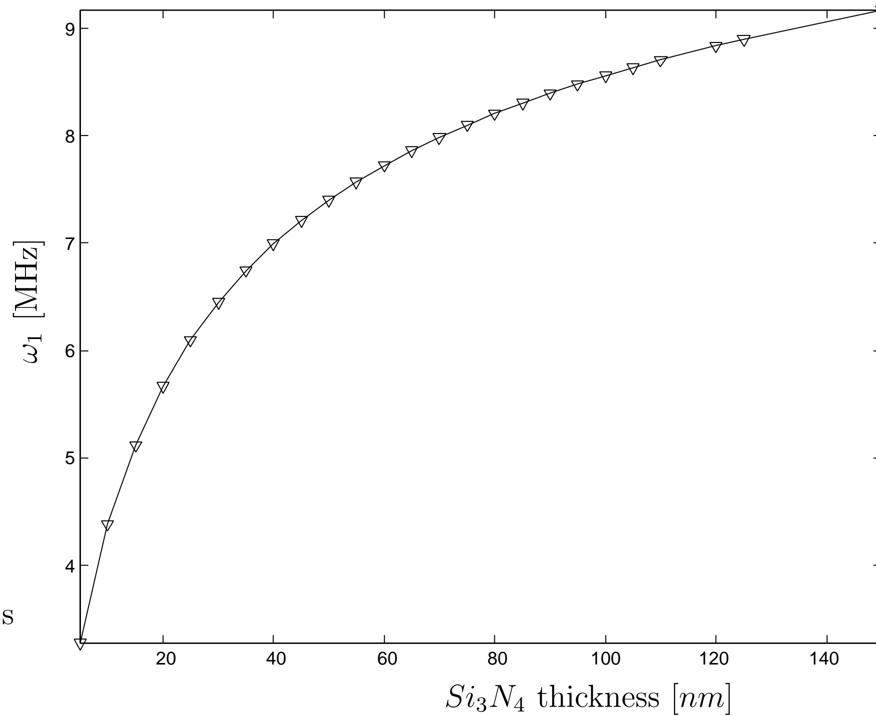

PSfrag replacements

Figure 5.14. Fundamental frequency variation with silicon nitride thickness

The disfigurement of the electro-mechanical hysteresis loop that occurs when the ribbon thickness is reduced significantly is visible in the hysteresis loop for the 50nm case. When reduced to 50nm the thickness of the Silicon Nitride layer is the same as that of the Aluminium layer. Between 50 and 70nm the flexibility of the ribbon in the y direction is such that contact occurs between the outer edges of the ribbon and the underlying oxide layer. Figures 5.16 (a)–(f) illustrate the position of the ribbon at key points through out the 50nm simulation. During the 50nm simulation the ribbon unit makes contact with the standoffs (a) like all previous simulations, then, due to the reduced lateral stiffness, continues to deform in the least stiff direction, across the ribbon (b). The ribbon continues to deform across the width until contact occurs with the oxide layer (c) at the free extremities. Peak voltage is achieved, and as the voltage subsides the regions of the ribbon furthest from the substrate experience the greatest decrease in applied load (d). The ribbon regions over the standoffs release (e), causing the minor release oscillations seen in the green line (upside down triangular markers) in Figure 5.15 at 16V. The applied voltage is reduced below the release voltage and the ribbon releases (e).

The critical voltages for the thickness simulations are listed in Table 5.8. As

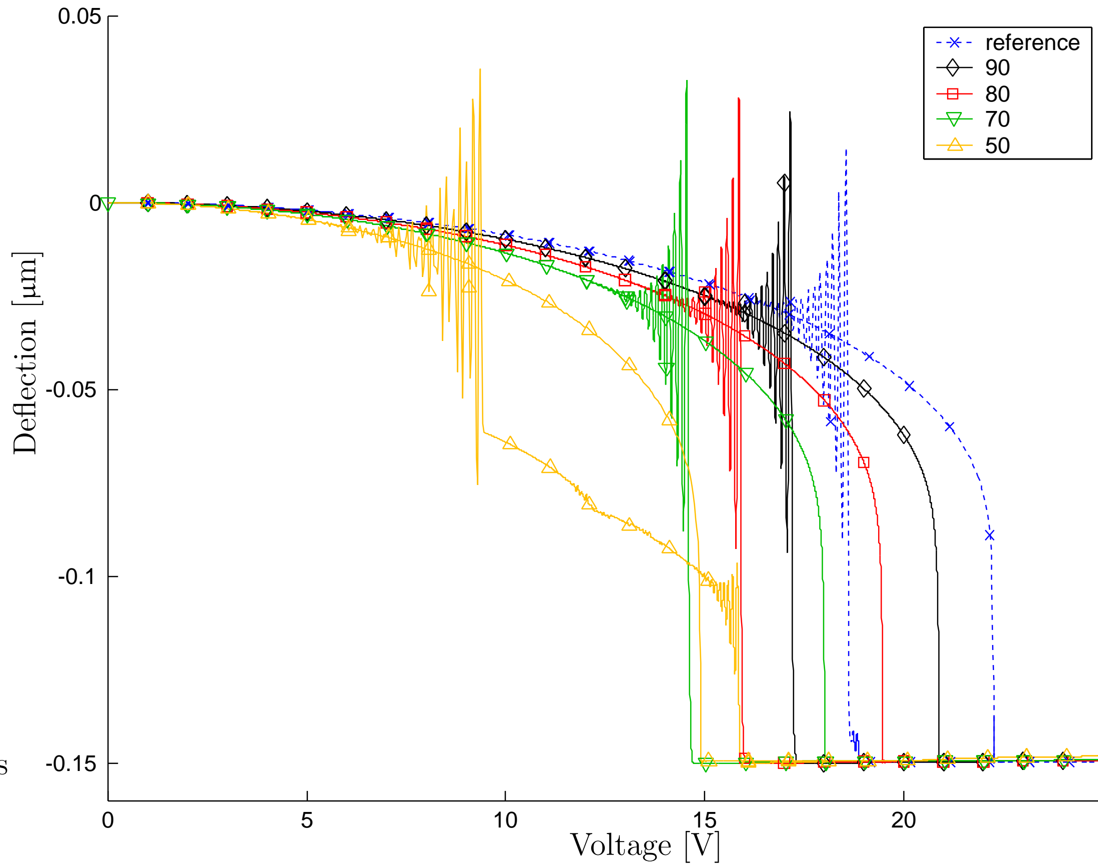

Figure 5.15. Hysteresis curves for thickness simulations

Table 5.8. Critical voltages for thickness simulations

Case	ω_1 [MHz]	V_{PD} [V]	V_{RL} [V]	ΔV [V]
Reference	8.56	22.28	18.67	3.61
90nm	8.40	20.90	17.26	3.64
80nm	8.21	19.49	15.97	3.51
70nm	7.99	18.03	14.65	3.37
50nm	7.41	14.91	9.47	5.44

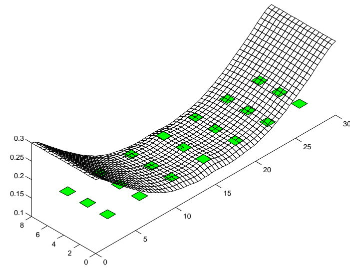

(a) Step 4000

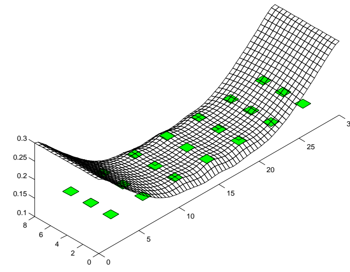

(b) Step 12000

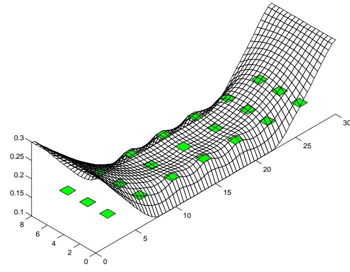

(c) Step 16000

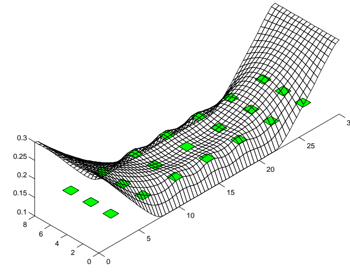

(d) Step 72000

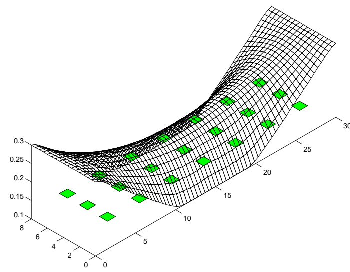

(e) Step 88000

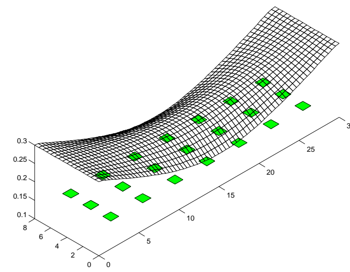

(f) Step 95930

Figure 5.16. 50nm Silicon Nitride thickness simulation ribbon unit positions showing substrate contact

the thickness of the Silicon Nitride layer decreases the ΔV varies slightly, until the ribbon unit makes contact with the oxide layer and the hysteresis behaviour changes, causing an increase in ΔV. The increase in ΔV arises as significant portions of the ribbon unit become positioned below the top of the standoffs. Electrode separation is diminished for the regions below the level of the standoffs and the electrostatic force on these regions of the ribbon is higher, resulting in delayed release, delaying global release of the ribbon unit and reducing V_{RL}.

The simulation runtime profiles show much the same behaviour as that observed in the initial material stress simulations (Figure 5.13). However, the 50nm case, Figure 5.17 (c), exhibits a large increase in the number of nodes in contact near step 13000. This large increase is attributable to the nodes that make contact with the oxide layer at the ribbon extremities ($y = 0$μm and $y = 8$μm). The dashed line in Figure 5.17(d) illustrates the number of nodes in contact with the oxide layer during the $t_{Si_3N_4} = 50$nm simulation.

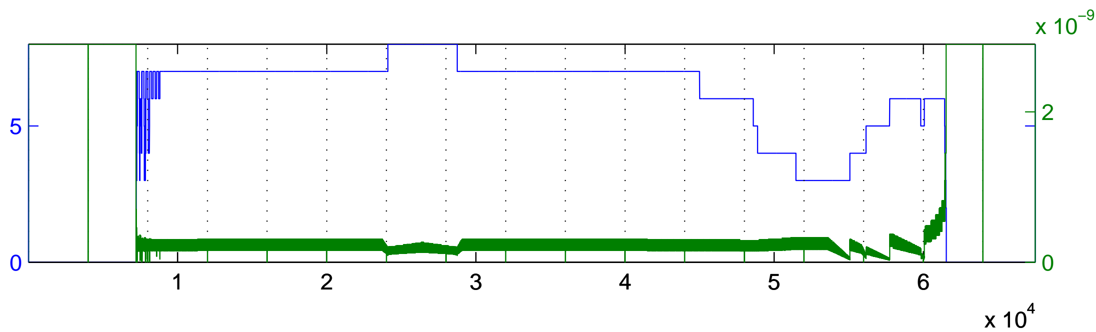

(a) 90nm

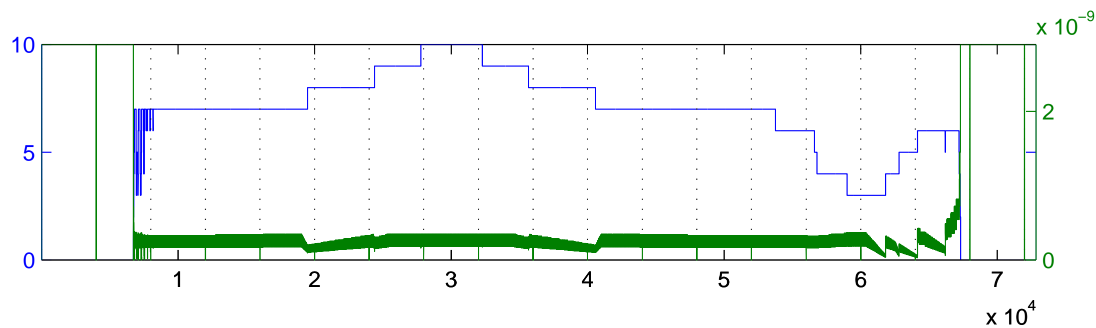

(b) 80nm

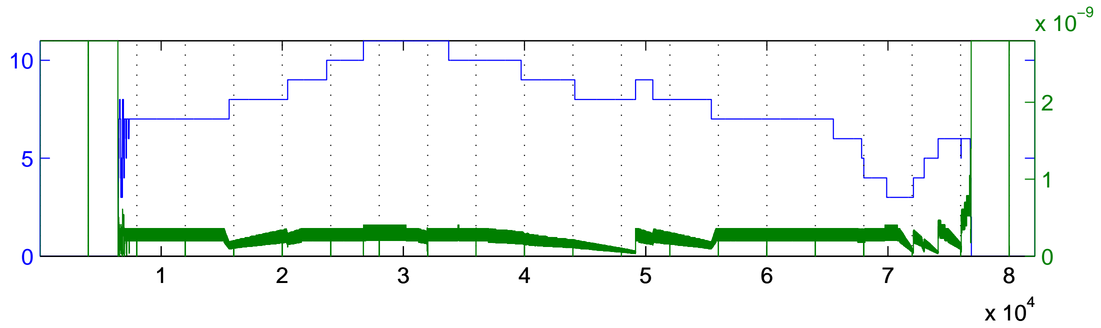

(c) 70nm

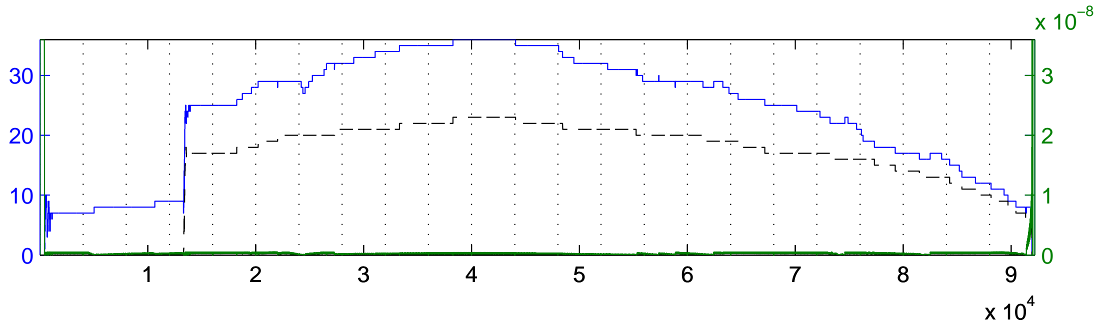

(d) 50nm

Figure 5.17. Silicon nitride thickness runtime profiles

The ribbon configuration from the $t_{Si_3N_4} = 50$nm simulation, step 40000, is illustrated in Figure 5.18. Contact between the ribbon and the oxide layer is visible as flat segments along the free edges of the ribbon. As the thickness of the ribbon unit is reduced the ribbon becomes more flexible, resulting in contact with the oxide layer at the extremities and draping between the standoffs.

As the thickness of the Silicon Nitride layer is reduced the stiffness of the ribbon unit decreases as does the minimum separation between the ribbon and the oxide layer, as illustrated in Table 5.9. The bold row in Table 5.9 highlights the fact that for the $t_{Si_3N_4} = 50$nm simulation case the ribbon makes contact with the oxide layer.

The difference in voltage at which minimum separation occurs for the 70nm and 50nm case suggest that the ribbon behaves in a static manner before contact with the substrate occurs. This last result illustrates the importance of the structural properties of the Silicon Nitride.

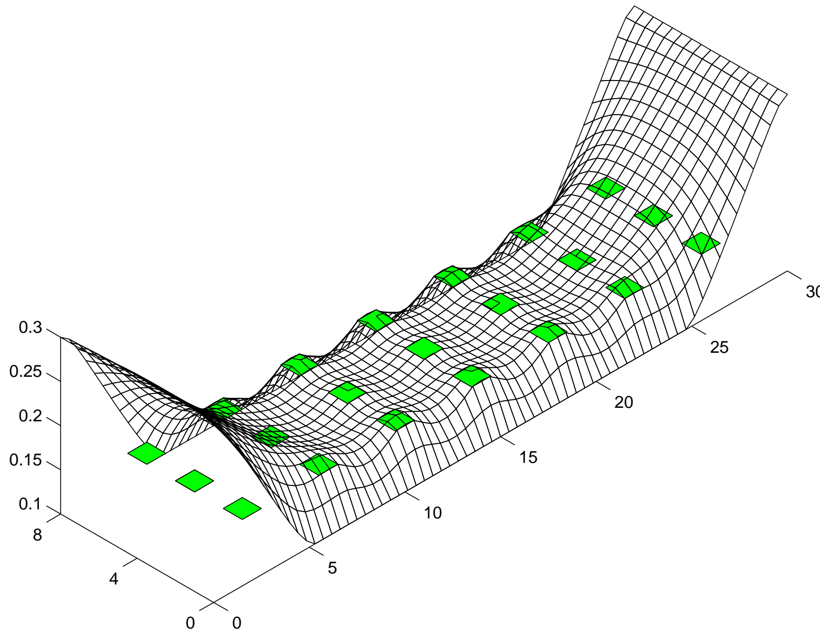

Figure 5.18. $t_{Si_3N_4} = 50$nm ribbon unit showing oxide contact

Table 5.9. Minimum electrode separations for thickness simulations

Case	Separation [μm]	Time [s]	Voltage [V]	x [μm]	y [μm]
Reference	0.03967	2.23×10^{-5}	22.28	12.79	0
90nm	0.03896	2.09×10^{-5}	20.91	12.79	0
80nm	0.03624	2.50×10^{-5}	25.00	13.24	0
70nm	0.02503	2.50×10^{-5}	25.00	13.24	0
50nm	**0**	$\mathbf{1.80 \times 10^{-5}}$	**17.96**	**13.24**	**0**

5.5. Standoff design

The design intent of the standoff structures is to prevent the ribbon from making contact with the oxide layer. While contact is to be avoided, it is undesirable to introduce excessive space between the conductors as it reduces the rate at which the electrostatic force will induce pull down.

The size and pattern of the underlying structural elements does not alter the fundamental characteristics of the GEMS ribbon unit, thus the natural frequencies of the device remain unaltered. However, varying the distribution and height of the underlying structural elements controls the quality of the reflector formed by the upper ribbon surface, and also defines the maximum permissible ribbon unit deflection. V_{PD} and V_{RL} also change as the standoff distribution alters V_{PD} by dictating where across the width of the ribbon unit contact first occurs, and V_{RL} changes as the proportion of the ribbon below the standoffs, experiencing higher forces, is controlled by the location of the standoffs. The parameters in standoff design geometry for which simulations were conducted are; standoff layer thickness ($t_{Standoff}$), standoff spacing along (x) the ribbon (s_x) and the standoff spacing across (y) the ribbon (s_y). These parameters are illustrated in Figure 5.1.

5.5.1. Standoff layout

The distribution of standoffs beneath the ribbon controls the quality of the planar reflective surface formed by the ribbon unit, and stipulates the minimum separation between electrodes. The minimum electrode separation is therefore also a function of ribbon unit stiffness and the thickness of the intermediate layers. Intuition suggests that the ribbon unit is most flexible along it center lines, both of which have been used as planes of symmetry, thus, all standoff designs posses a row of standoffs at the lines of symmetry. Varying the inter-standoff spacing in the x (s_x) and y (s_y) directions is anticipated to cause differing contact scenarios as the initial material stress, the key contributor to device stiffness, acts only in the x coordinate direction.

5.5.1.1. Variation across the ribbon width (s_y)

The reference ribbon unit configuration (Table 5.1) has three rows of underlying standoffs. As was observed in the thickness simulations the GEMS ribbon unit is most flexible in the direction perpendicular to the initial material stress. Thus

varying the standoff spacing in the y coordinate direction will cause contact with the oxide layer where the outer extremities of the ribbon ($y = 0\mu m$ and $y = 8\mu m$) curve downwards and touch the oxide layer.

Some practical limits are implied for the variation in standoff spacing across the ribbon. Firstly Kodak indicate that the standoffs must be concealed beneath the ribbon structure [Kowarz, 2001] preventing degradation of reflected light intensity. Thus, s_y cannot exceed 3.5μm if $s_{l_x} = s_{l_y} = 1\mu m$. Decreasing s_y below 1μm results in a single row of standoffs, which is not anticipated to prevent contact between the ribbon and the oxide layer from occurring.

Figure 5.19 illustrates the effect on the deformed ribbon cross section of varying s_y. For clarity, only the positions of the center ($x = 15\mu m$) row of nodes have been plotted. As s_y is increased the profile transitions, first, from a convex reflector ($s_y < 2\mu m$) to a flat reflector ($s_y = 2.5\mu m$) with feathered edges, and then to a concave reflector. Clearly, as the reflective surface formed becomes more convex reflected light becomes more diffuse and difficult to control. Marginally

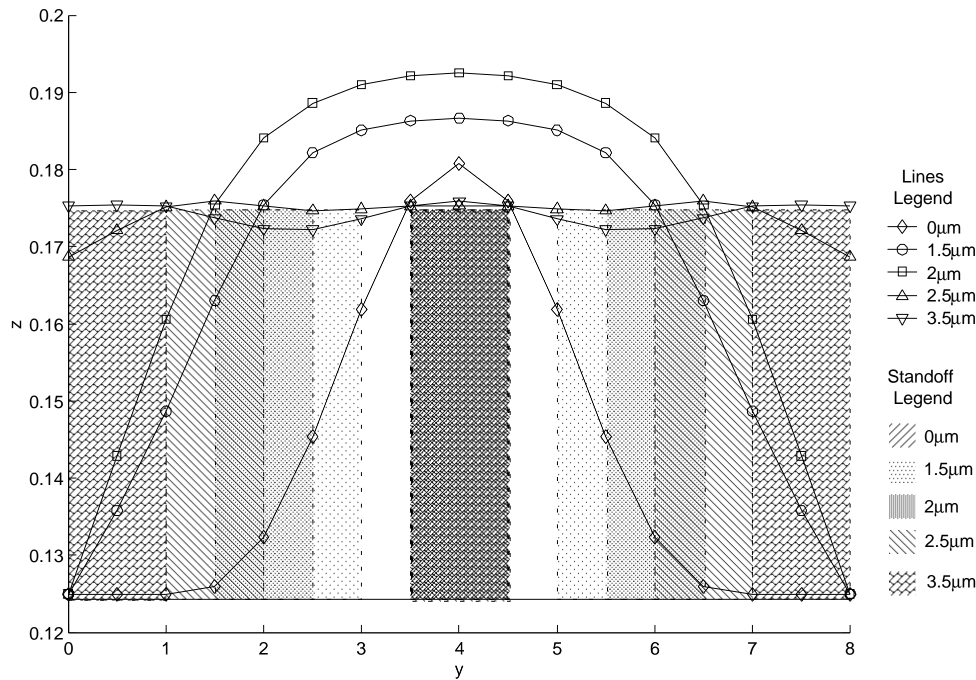

Figure 5.19. Ribbon profiles ($x = 15\mu m$) for s_y simulations

($-0.5\mu m$) decreasing s_y below the reference value of 2.5μm results in the ribbon making contact with the oxide layer at the outer extremities. The results in Figure 5.19 are unobtainable using a string representation for the GEMS ribbon unit and highlight the necessity of a distributed solution to the structural problem.

Particularly in the case of the GEMS ribbon where optical performance is the desired end result.

Figure 5.20 illustrates the electro-mechanical hysteresis of the center of the ribbon unit. Altering the standoff spacing does not change the ribbon character-

PSfrag replacements

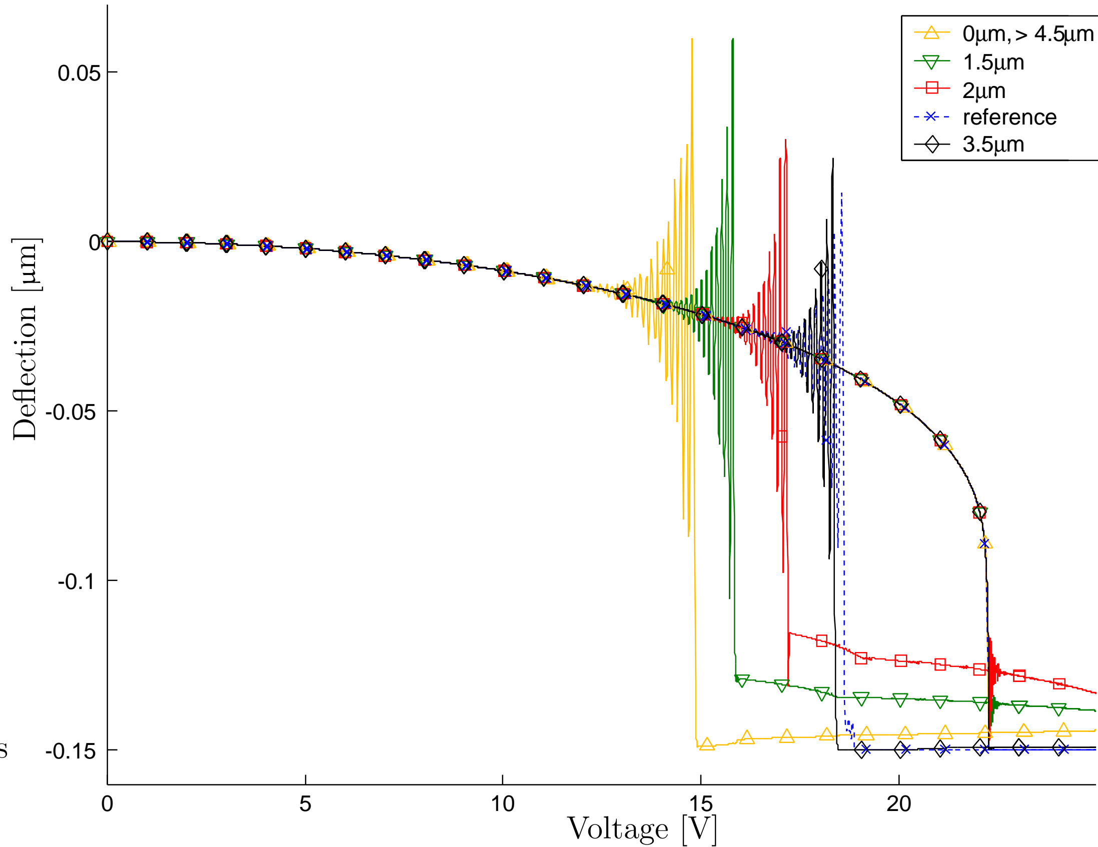

Figure 5.20. Hysteresis curves for s_y simulations

istics, as Figure 5.20 highlights the pull down bifurcation for all s_y simulations occurs at approximately 22.28V. The small variation in V_{PD} is due to the movement of the standoffs with which the ribbon first makes contact. In all simulations the outer standoffs are contacted first, due to the effects of Poisson's ratio on the cross-section of the ribbon unit, thus moving the outer standoffs marginally alters the voltage at which contact first occurs.

In Figure 5.20 for voltages between V_{PD} and V_{RL}, and s_y less than 2.5µm the center point of the ribbon unit does not remain in contact with the center standoff. This result is attributable to the outer extremities of the ribbon making contact with the oxide layer and the center point breaking contact with the center node. The final position of the center point is then controlled by the ribbon stiffness.

The same effect is evident in Figure 5.19, where the ribbon center point is not in contact with the center standoff when the applied voltage is 25V.

Table 5.10 lists the critical voltages for the s_y simulations. The effect of al-

Table 5.10. Critical voltages for s_y simulations

Case	V_{PD} [V]	V_{RL} [V]	ΔV [V]
0µm, > 4.5µm	22.27	14.86	7.41
1.5µm	22.29	15.88	6.40
2µm	22.29	17.23	5.05
2.5µm (Reference)	22.28	18.67	3.61
3.5µm	22.28	18.43	3.86

tering the location of the standoffs only significantly effects the voltage at which the ribbon releases (V_{RL}) as the standoff distribution controls the minimum separation between the movable and stationary electrodes. The more the ribbon is allowed to deform below the standoffs, the more V_{RL} decreases. As V_{RL} decreases the amplitude of the post-release oscillations is observed to increase, as the ribbon unit is subject to lower voltages post-release.

Figure 5.21 illustrates the simulation runtime profiles for the s_y simulations.

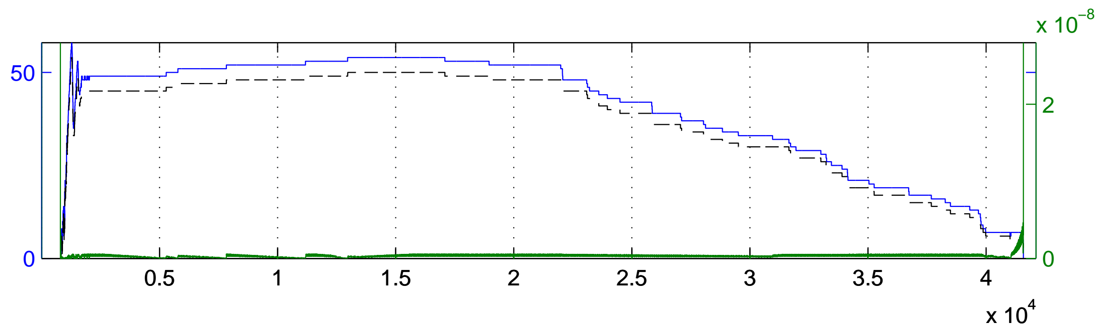

(a) $s_y = 0$µm or $s_y > 4.5$µm

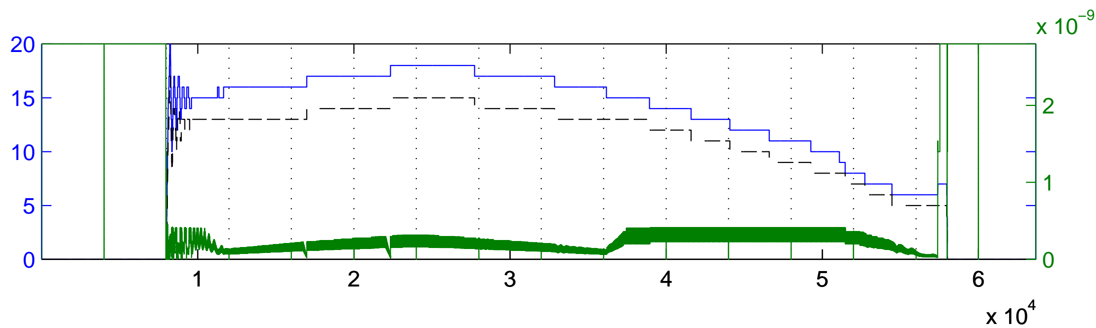

(b) $s_y = 1.5$µm

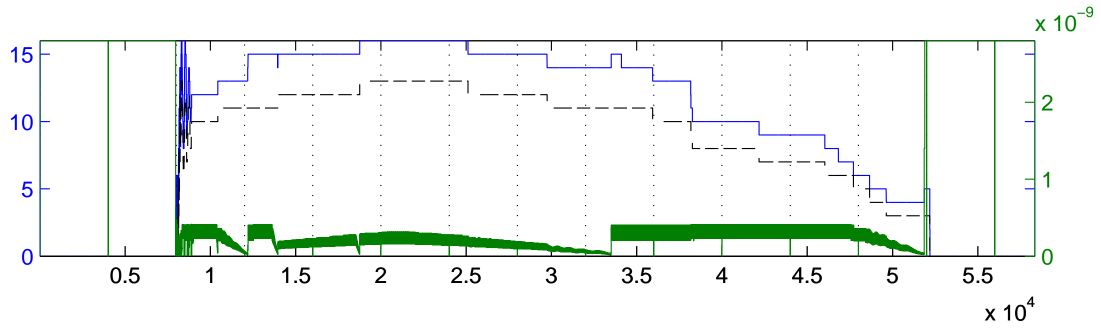

(c) $s_y = 2\mu\text{m}$

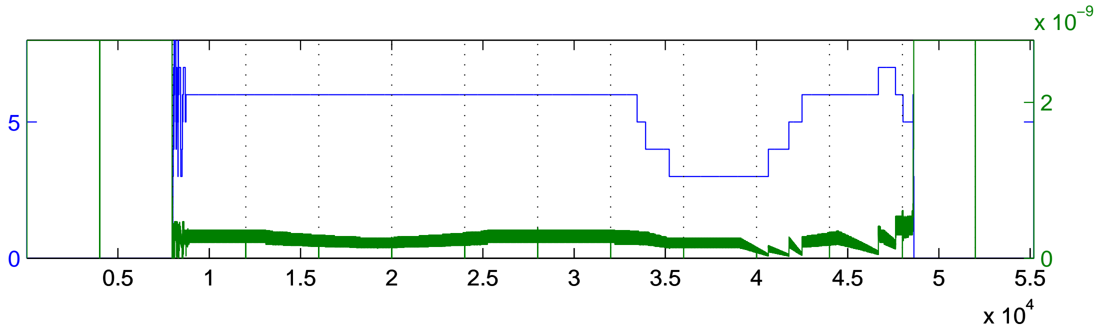

(d) $s_y = 3.5\mu\text{m}$

Figure 5.21. Standoff layout (s_y) simulation runtime profiles

The large number of contacted nodes observed in Figure 5.21(a) are the direct result of contact between the ribbon and the oxide layer. The lower dashed (black) line, plotted on the left hand axis in Figure 5.21(a)-(c) indicates the number of nodes in contact with the oxide layer in each time step. As Figure 5.21(a) indicates, most of the contacted nodes in the $s_y = 0\mu\text{m}$ simulation come into contact with the oxide layer as the structure drapes over the standoffs. Figure 5.22 depicts the $s_y = 0\mu\text{m}$ simulation case at step 15000. The standoffs (shaded, raised regions) only contact a small number of nodes. The bulk of the contacted nodes meet the oxide surface. This figure also highlights the capability of the analysis method developed to capture complex structural interaction dynamics.

Table 5.11 lists the minimum separation between the lower ribbon surface and the oxide layer. The 0µm, 1.5µm and 2µm cases make contact with the substrate, indicating that any small decrease from the stated reference standoff configuration will cause contact to occur with the oxide layer. Therefore, the reference standoff configuration is pretty close to optimal for variation in s_y.

Decreasing s_y from the reference value of 2.5µm results in a decrease in ΔV as the minimum separation between the ribbon unit extremities and the oxide

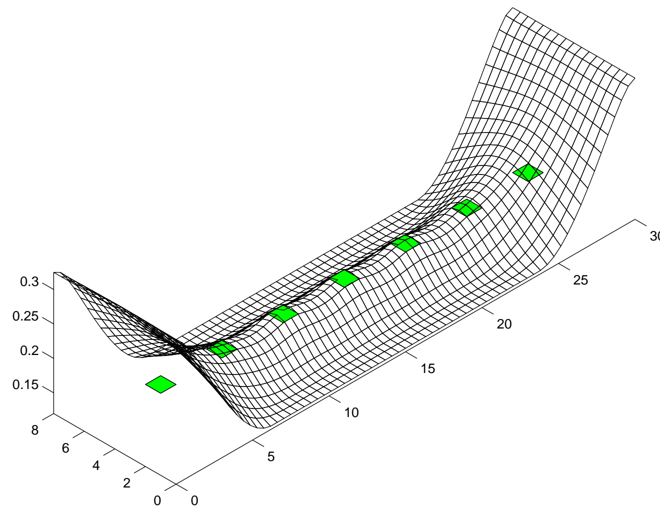

Figure 5.22. $s_y = 0\mu\text{m}$ ribbon unit showing oxide contact

Table 5.11. Minimum electrode separations for s_y simulations

Case	Separation [μm]	Time [s]	Voltage [V]	x [μm]	y [μm]
0μm	**0**	$\mathbf{2.23 \times 10^{-5}}$	**22.28**	**15**	**0**
1.5μm	**0**	$\mathbf{2.23 \times 10^{-5}}$	**22.29**	**15**	**0**
2μm	**0**	$\mathbf{2.23 \times 10^{-5}}$	**22.30**	**14.56**	**0**
Reference (2.5μm)	0.03967	2.23×10^{-5}	22.28	12.79	0
3.5μm	0.04322	2.23×10^{-5}	22.29	12.79	0

layer reduces. A reduction in minimum separation results in higher forces on the ribbon unit, hence the delay in release.

The deformed cross-sectional profile of the GEMS ribbon unit controls whether it reflects light as a diffuse or concentrating reflector. The results obtained for the s_y simulations indicate that for values of s_y below 2.5μm the ribbon unit acts a diffuse reflector, increasing the width of the "point source" created by the ribbon. Altering s_y allows control over the shape of the reflector formed, thus increasing s_y to the maximum permissible value of 3.5μm is recommended as this prevents the ribbon unit from acting as a diffuse reflector.

5.5.1.2. Variation along the ribbon length (s_x)

This section examines increasing the inter standoff spacing along the length of the ribbon (s_x), parallel to the initial material stress, until contact with the oxide layer occurs. The type of contact anticipated is unique to this family of simulations in that as the length of ribbon between the standoffs increases, the regions between standoffs are expected to behave like short span replicas of the ribbon unit and make contact half way between adjacent standoffs. Decreasing s_x was not considered as the ribbon is fixed perpendicular to the x axis and it is not possible for the ribbon to sag at the fixed ends.

As the standoff spacing in the x direction is increased, the ribbon droops between adjacent standoffs, coming closer to the oxide layer, as illustrated in Figure 5.23. In Figure 5.23 the solid line at $z = 0.125$μm indicates the upper surface of the oxide layer and the dashed line segments with upper surfaces at $z = 0.175$μm indicate location of the standoffs. As s_x is increased the flexural deformation at the ribbon extremities is observed to increase, as depicted in Figure 5.23 by the increase in number of nodes visible.

Figure 5.24 displays the electro-mechanical hysteresis behaviours of the ribbon units when $s_x = 4$μm, 6μm and 8μm. As the standoff spacing (s_x) is increased the electrode separation in the activated state is reduced. Thus, the release voltage (V_{RL}) is reduced. The changes in operating voltages for the s_x simulations are listed in Table 5.12.

In contrast to the s_y simulation V_{PD} does not change, as a result of the center row of standoffs remaining unmoved throughout the family of simulations. The runtime profiles in Figure 5.25 for the s_x simulations show the substrate contact that occurs during each simulation. When $s_x = 8$μm the majority of nodes make

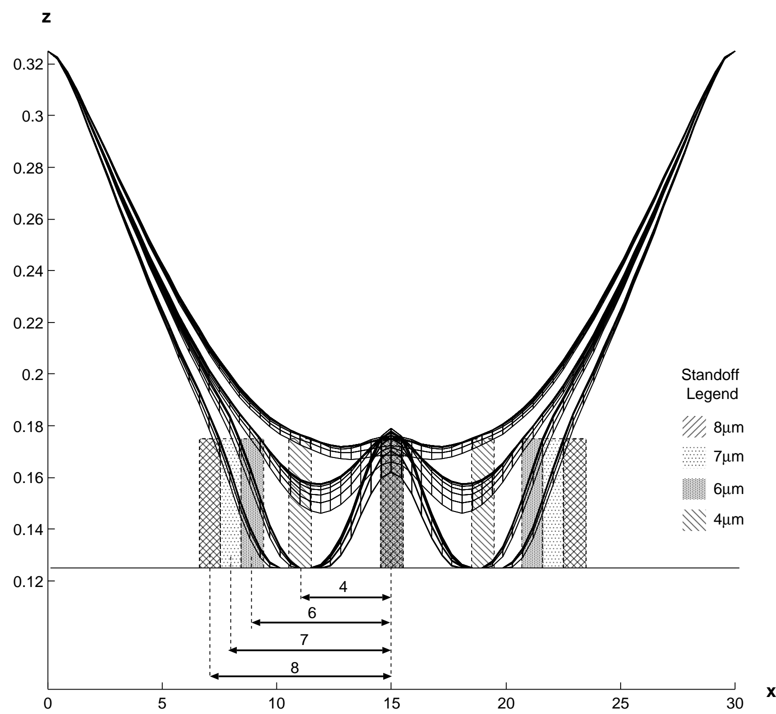

Figure 5.23. Ribbon profiles ($y = 4\mu m$) for s_x simulations

Table 5.12. Critical voltages for s_x simulations

Case	V_{PD} [V]	V_{RL} [V]	ΔV [V]
4μm (Reference)	22.28	18.67	3.61
6μm	22.28	18.53	3.75
8μm	22.28	16.36	5.92

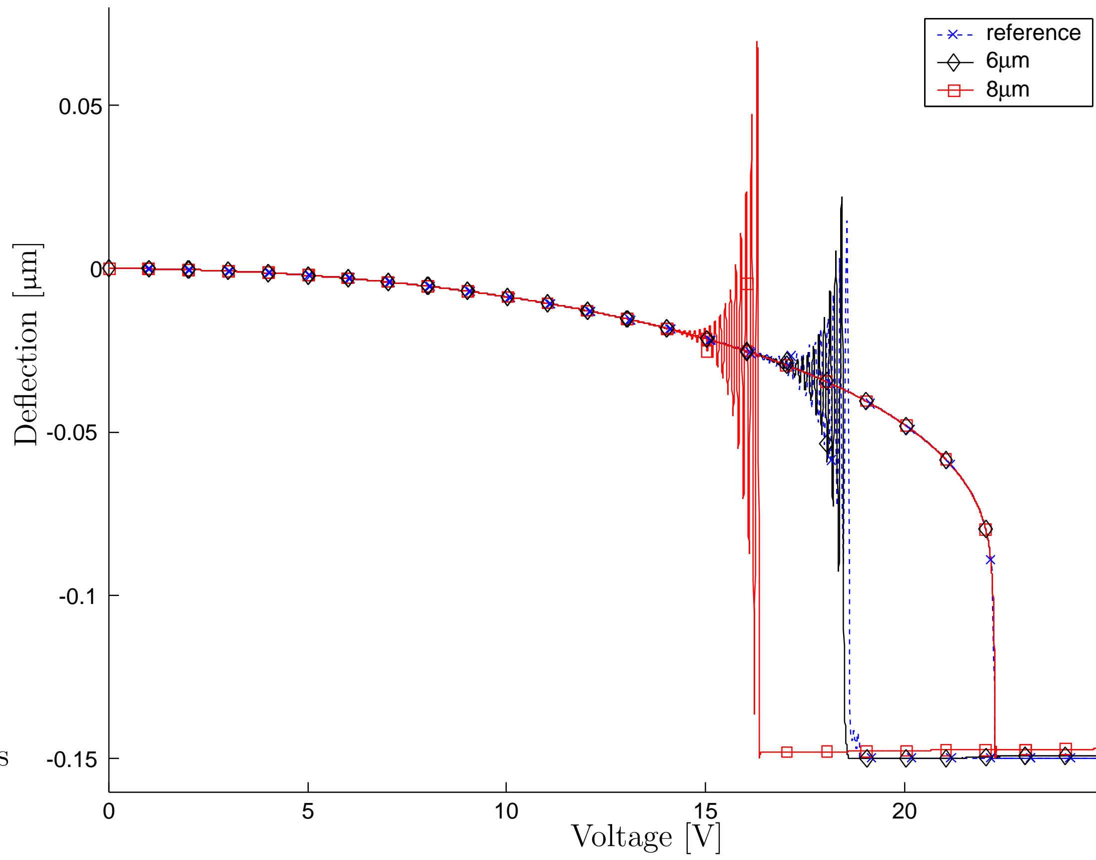

Figure 5.24. Hysteresis curves for s_x simulations

contact with the oxide layer.

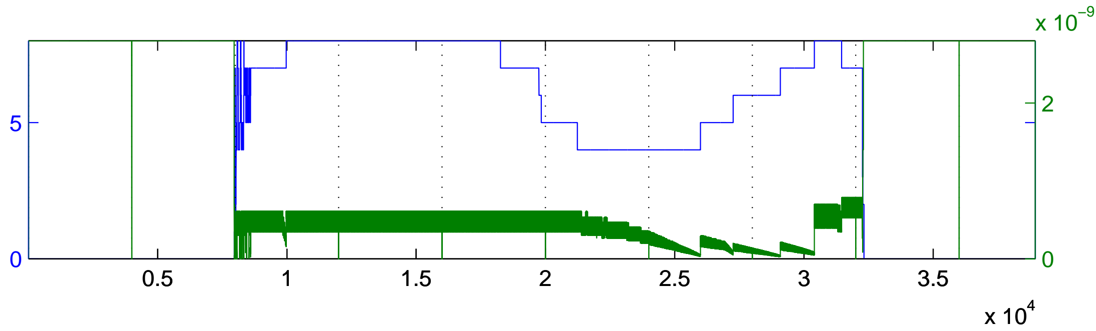

(a) $s_x = 6\mu m$

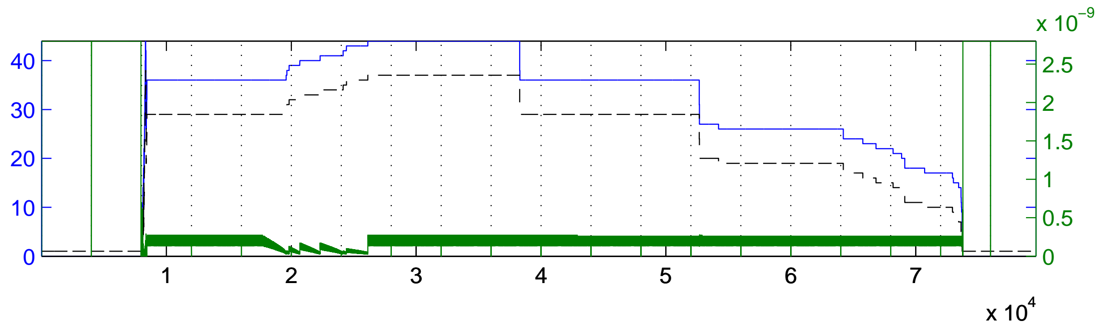

(b) $s_x = 8\mu\text{m}$

Figure 5.25. Standoff layout (s_x) simulation runtime profiles

Finally, Figure 5.26 illustrates the contact scenario that arises when s_x is too large. The regions of the ribbon unit suspended between the standoffs become short span replicas of the ribbon unit and sag contacting the oxide layer.

As the spacing between standoffs increases the minimum separation between the ribbon unit and the oxide layer decreases until contact occurs. Table 5.13 lists the minimum separation values modelled.

Table 5.13. Minimum electrode separations for s_x simulations

Case	Separation [µm]	Time [s]	Voltage [V]	x [µm]	y [µm]
Reference	0.03967	2.23×10^{-5}	22.28	12.79	0
6µm	0.02118	2.50×10^{-5}	24.99	11.91	0
8µm	**0**	$\mathbf{2.23 \times 10^{-5}}$	**22.31**	**11.47**	**0**

As s_x is increased from the reference value of 4µm the sagging between neighbouring standoffs increases, resulting in a drop in the minimum separation between ribbon unit and oxide layer. The increase in s_x results in no change in V_{PD},

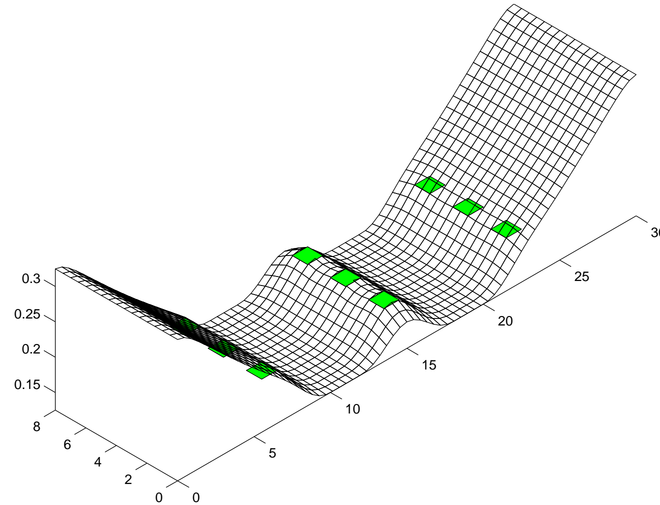

Figure 5.26. $s_x = 8\mu$m deformed ribbon unit showing oxide layer contact, simulation step 32000

as the center row of standoffs is not moved, but a drop in V_{RL} and subsequent rise in ΔV are observed, as more of the ribbon deforms below the level of the standoffs. The decrease in V_{RL} also results in larger peak magnitudes of the post release oscillations. The results obtained suggest that s_x not be increased above 6μm to prevent contact with the oxide layer.

The analysis presented emphasises that the location of the standoffs beneath the ribbon unit be accurate and uniform, as small deviations in location can promote the onset of contact with the oxide layer.

5.5.2. Standoff height

Varying the thickness of the standoff layer ($t_{Standoffs}$) alters height of the standoffs and the initial electrode separation. Decreases in initial electrode separation result in greater forces on the ribbon unit, advancing the pull down bifurcation. However, the resulting decreased separation in the contacted state delays the release bifurcation, increasing ΔV. The second effect of reducing the height of the standoff layer is the increased potential for substrate contact, as less "sagging" between standoffs is tolerated before contact with the oxide layer occurs.

Figure 5.27 illustrates the electro-mechanical hysteresis behaviour of the ribbon unit with variations in standoff height. The peak deflection for all simulated cases is identical as the initial air gap (t_{A_0}) between the top of the standoffs and the lower surface of the ribbon remains unchanged. However, as the initial

separation of the electrodes reduces with the thickness of the standoff layer, the pull down bifurcation is occurs at a reduced voltage. The reduced electrode sep-

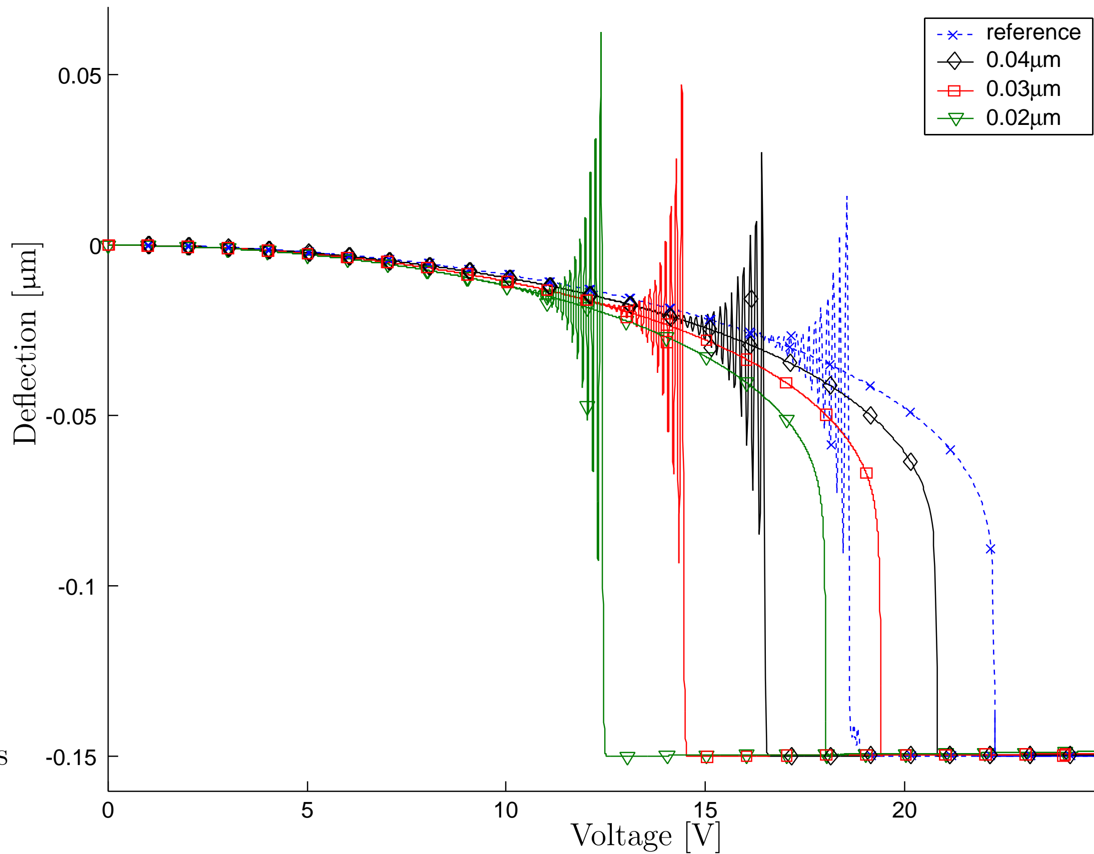

Figure 5.27. Hysteresis curves for standoff height simulations

aration in the contacted configuration delays release as the forces on the ribbon unit remain higher until lower voltages. The release at lower voltages is also manifest in the amplitude of the post release oscillations, which increase as the standoff height is reduced due to the smaller applied voltage post-release. From Figure 5.27 the location of the pull down and release bifurcation points can be established and Table 5.14 lists these values, which illustrate the increase in ΔV with the decrease in standoff height as well as the decrease in V_{PD} and V_{RL}.

Figure 5.28 illustrates the runtime profiles for the standoff height simulations. Figure 5.28(c) illustrates the runtime profile for a simulation in which the ribbon makes contact with the substrate. The lower dashed line in Figure 5.28(c) is the number of nodes in contact with the oxide layer during the simulation.

Table 5.14. Critical voltages for standoff height simulations

Case	V_{PD} [V]	V_{RL} [V]	ΔV [V]
Reference	22.28	18.67	3.61
0.04µm (80%)	20.83	16.54	4.28
0.03µm (60%)	19.42	14.50	4.92
0.02µm (40%)	18.04	12.46	5.58

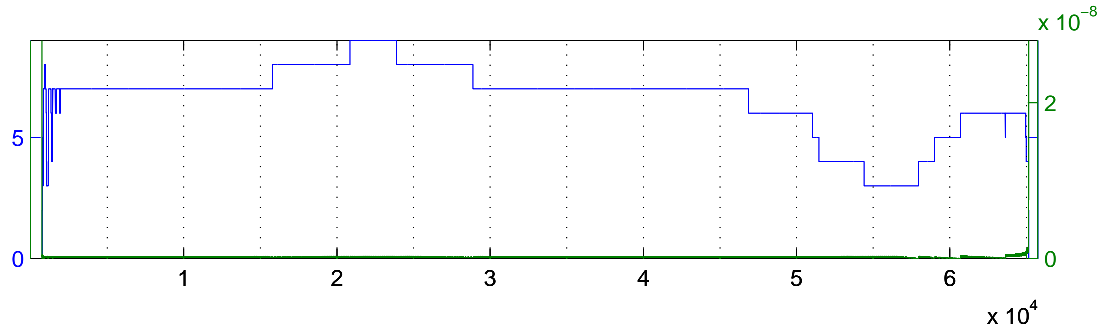

(a) $t_{Standoffs} = 0.04\mu m$ (80%)

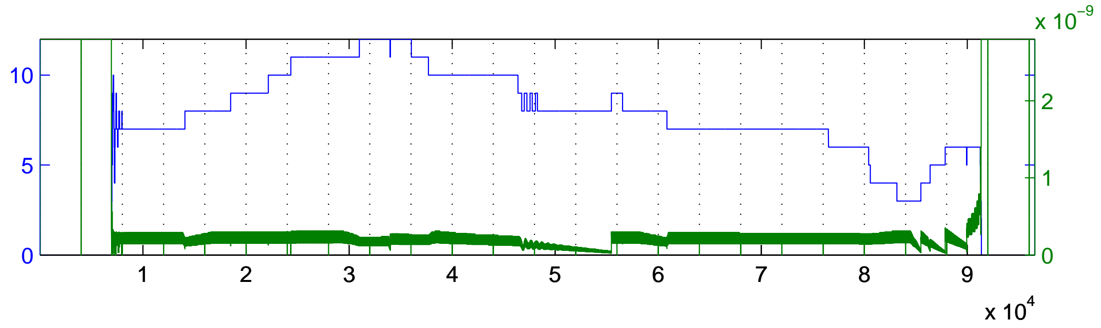

(b) $t_{Standoffs} = 0.03\mu m$ (60%)

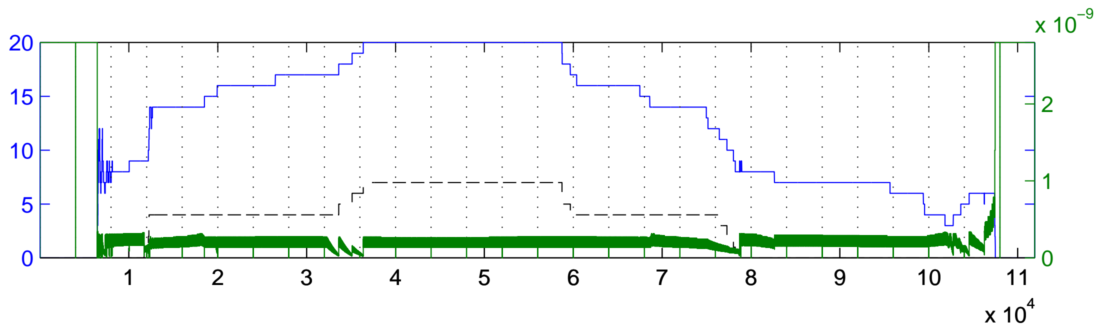

(c) $t_{Standoffs} = 0.02\mu m$ (40%)

Figure 5.28. Standoff height simulation runtime profiles

Figure 5.29 illustrates the deformed ribbon unit state at step 44000, where the edges of the ribbon unit between the standoffs have drooped and made contact with the oxide layer. As expected, reducing the height of the standoff layer

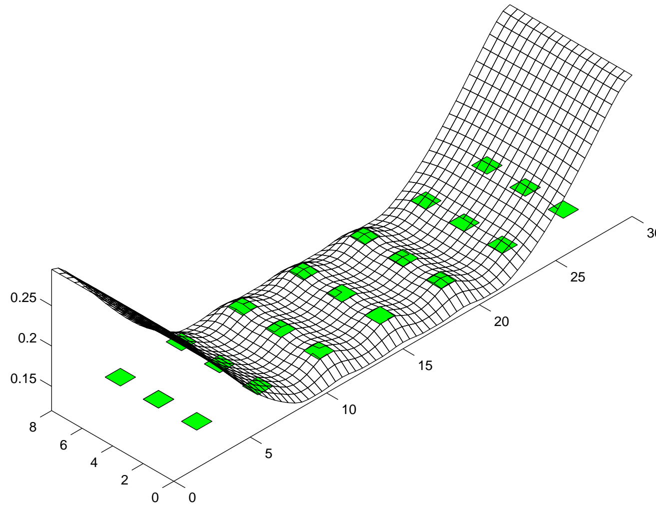

Figure 5.29. $t_{Standoffs} = 0.02\mu\text{m}(40\%)$ deformed ribbon showing oxide layer contact, simulation step 44000

affords the ribbon unit less "sagging" before contact with the oxide layer occurs. Table 5.15 lists the minimum separation characteristics of the standoff thickness simulations.

Table 5.15. Minimum electrode separations for standoff height simulations

Case	Separation [μm]	Time [s]	Voltage [V]	x [μm]	y [μm]
Reference	0.03967	2.23×10^{-5}	22.28	12.79	0
0.04μm (80%)	0.02719	2.08×10^{-5}	20.83	12.79	0
0.03μm (60%)	0.00878	2.30×10^{-5}	23.01	8.82	0
0.02μm (40%)	**0**	$\mathbf{1.80 \times 10^{-5}}$	**18.04**	**12.79**	**0**

Reducing the thickness of the standoff layer alters the initial electrode separation advancing V_{PD}, without altering the stiffness of the GEMS ribbon unit. A reduction in the thickness of the standoff layer also reduces the height of the standoffs, reducing the devices tolerance to "sagging" before contact occurs.

The simulations conducted have shown that minimum electrode separation occurs during the"zipping" of the GEMS ribbon unit, indicating that the dynamics of the device exert more influence than the peak voltage applied. Therefore,

it is suggested that the standoff height simulations be run under dynamic conditions, such as those used in Section 5.2. Allowing an assessment of the minimum dynamic separation, ensuring that reducing the thickness of the standoff layer does not cause contact during dynamic operation.

Chapter 6

Conclusions

In the course of this research program, a robust numerical solution framework for the dynamic analysis of thin film MEMS devices has been developed, implemented, tested and utilized to examine the design space for Eastman Kodak's GEMS device. The framework is generalizable to the dynamics of all structures, but the salient phenomena included apply specifically to electrostatically actuated thin film bifurcating structures.

The adopted implementation utilizes a mixture of hybrid stress and displacement finite elements in a iterative numerical marching procdure. Electrostatic equlibrium is attained by enforcing a tolerance on the difference between the $\mathbf{L_2}$ norm of the deformed structural configuration and the configuration used to calculate applied electrostatic forces. Structural contact is modelled by enforcing zero additional deflection on model node known to be in contact with adjacent structural elements.

The current implementation provides a platform for the simulation of variations in key device parameters, enabling the diagnosis of fabrication problems, the delaying of prototype fabrication until the characterisation of the device design space is complete, and an understanding of the effects of fabrication variability on device dynamics. It also provides a platform for the future addition of additional physical phenomena, allowing more complex models to be created from the validated code base. Such additions could include the modelling of fluid movement surrounding devices, interfacial delaination and interactions between devices in an array.

The results generated highlight the complexity of the dynamic analysis of MEMS structures, revealing that accurately capturing the transverse deformation, across the width, of such structures is pivotal to correctly understanding their operation. For the GEMS structure transverse deformation is the most common cause of contact with the oxide layer, and the single largest contributor to the quality of the reflector formed by the deformed ribbon unit. This discovery

invalidates modelling such structures using solutions based on beam theory and string models, as the omission of Poissions ratio results in uniform deformation across the structures width.

The differences between the dynamic and quasi-static modelling of such structures has been illustrated and shown to be significant, particularly when attempting to assess the minimum separation between movable and stationary structural elements. It has been shown that the dynamics of MEMS structures and not the peak applied voltage are often the cause this minimum separation. Quasi-static models fail to capture dynamic behaviours in the response of MEMS structures. The oscillations observed in the post release behaviour of the GEMS device are an excellent example that impacts on the devices optical performance. The omission of such significant phenomena can confuse MEMS product designers when trying to understand the results of prototype experiments.

Simulating the changes in response of the GEMS device to perturbations in key parameters clearly illustrates that the design space surrounding the structure is complex, with coupling present between a number of parameters. A consequence of this result is that perturbations were limited to a single parameter per family of simulations. Results from these simulations suggest that the reference configuration of the GEMS ribbon unit is close to the edges of the design space, particularly those relating to standoff distribution and shape. Other results show the current solution in a far more stable region of the design space.

Varying the rate at which the voltage on the structure is altered suggests that the GEMS device is capable of bifurcating to the activated configuration very quickly ($<$ 20 ns). However, to effectively control the duration of the post release oscillations the gradient of the release ramp must occur in more than 300ns but less than the 25µs of the static limit test. It is currently not known what the gradient of the release voltage ramp is for experimental devices. It may also be possible to further control release oscillations using an active control technique to modulate the applied voltage post realease.

This research reiterates the dominance of the initial material stress on the fundamental dynamic characteristics of the GEMS device. However, it also shows that in the absence of the initial material stress the GEMS device is still observed to bifurcate at two distinct points. However, the resulting oscillation at the fundamental natural frequency of the structure makes the post release oscillations impossible to control in a timely manner, resulting in a device with excellent pull down characteristics (low V_{PD}, ΔV $<$ 5V) but excessive post release oscillations.

Results obtained also suggest that under a small compressive load the GEMS ribbon unit buckles, suggesting that an investigation of the operating temperatures of the device is required to negate this possible failure mode.

Thinning the Silicon Nitride layer of the GEMS device results in a disfigurement of the hysteresis behaviour of the structure. As the natural and initial material stress contributions to the stiffness of the device decrease, the structural flexibility in the transverse direction increases rapidly due to the remaining initial material stress contributions along the device. Contact between the ribbon unit edges and the oxide layer occur if the thickness is reduced below 70nm. Due to the high forces experienced by these contacted regions, the center of the ribbon unit releases at 16V but the extremities remain in contact until 9.5V. Capturing this partial release phenomena highlights the power of the chosen modelling techniques.

Reducing the spacing between the standoffs in the transverse (y) direction by 0.5μm causes the ribbon unit to make contact with the substrate at its extreme ($y = 0$μm & $y = 8$μm) edges. A change in standoff spacing may arise from the removal of sacrificial material as the ribbon unit is released, when excessive etchant application results in the removal of standoff material, resulting in tapered instead of cuboid standoffs. The ribbon unit is less sensitive to variations in the standoff spacing in the x direction, where the inter-standoff spacing has to be increased by more than 2μm before contact with the oxide layer occurs. Reducing the standoff spacing in the x direction increases the number of standoffs with which the ribbon unit makes contact, increasing the likelyhood of a frictional failure. Reducing the thickness of the standoff layer, hence the standoffs, causes the ribbon to pull down at earlier, as the initial electrode separation is reduced, but increases the operating ΔV of the device as the ribbon unit remains in the deformed configuration until significant voltage reduction occurs.

6.1. Future work

Given additional resources it is the opinion of the author that future research conducted should investigate:

1. Simulate $t_{\mathrm{Si}_3 4_4} = 60$nm to confirm the trend observed in the thickness simulation results.

2. Determine maximum release slew rate for effective post release oscillation control.

3. Determine the critical temperature change required to induce sufficient compressive stress in the ribbon to cause buckling due to self weight. It is anticipated to be large as the initial material stress in the Silicon Nitride is significant.

4. Assess the performance of the chosen materials once detailed compositions are known. Evaluate the susceptibility of the chosen Aluminium alloy system to strain hardening and other materials related failure mechanisms.

5. Tune the voltage model and assess in detail the validity of the parallel plate capacitor approximation. More specifically experimental data and 3D numerical techniques are required, as the current assumptions are based only on 2D models. Reassess the validity of assuming the upper conductor is located at the neutral axis of the structure.

6. Refactor code to not include membrane degrees of freedom when initial stress force effects ($\{q\}$) are disabled, saving computational time, and storage space. Or move the history arrays to sparce matrices allowing the Matlab pack command to remove unused space.

7. Model the interactions of a dual layer device, doubling the number of finite elements in the system. It is recommended that this task is done after refactoring. This model would provide the ability to model delamination and crack propagation at the Aluminium-Silicon Nitride interface.

8. Generalize the damping model by incorporating fluidic effects and remove the 5% damping assumption.

9. Model the fluidic pressure effects on neighbouring GEMS ribbons in the arrayed configuration to quantify the fluidic cross-talk.

10. Implement more efficient timestep reduction techniques, allowing for earlier sustained growth. Add Bisection or Newton Rhapson control to step size algorithm.

11. Investigate the sensitivity of solution runtime to variations in control parameters.

References

Adini, A., Clough, R. W., 1960. Analysis of plate bending by the finite element method. NSF report for grant G-7337 .

Apte, R. B., 1994. Grating Light Valves for High Resolution Displays. Ph.D. thesis, Stanford University.

Artz, B. E., Cathey, L. W., 1992. A Finite Element Method for Determining Structural Displacements Resulting from Electrostatic Forces .

Bass, M., 1995. Handbook of Optics, 2nd Edition. Vol. II. Mc Graw Hill.

Bloom, D. M., Sandejas, F. S. A., Solgaard, O., 1994. Method and Apparatus for Modulating a Light Beam. US 5,311,360.

Bogner, F. K., Fox, R. L., Schmit, L. A. J., 1965. The Generation of Inter–Element Stiffness and Mass Matrices by the Use of Interpolation Formulas .

Cai, X., Yie, H., Osterberg, P., Gilbert, J., Senturia, S., White, J., 1993. A Relaxation/Multipole-Accelerated Scheme for Self-Consistent Electromechanical Analysis of Complex 3-D Microelectromechanical Structures. pp. 283–286.

Carr, A. J., 1967. A Refined Finite Element Analysis of Thin Shell Structures Including Dynamic Loadings. Ph.D. thesis, Structures and Materials Research, Department of Civil Engineering, University of California, Berkley.

Carr, A. J., 2001. RUAUMOKO, The Maori God of Volcanoes and Earthquakes. Department of Civil Engineering, University of Canterbury.

Caughey, T. K., 1960. Classical Normal Modes in Damped Linear Systems. J. Appl. Mech 27, 269–271.

Chen, J., Kang, S. M., 2000. An Algorithm for Automatic Model-Order Reduction of Nonlinear MEMS Devices. IEEE International Symposium on Circuits and Systems .

Davey, K., Klimpke, B., 2002. Computing Forces on Conductors in the Presence of Dielectric Materials. IEEE Transactions on Education 45 (1), 95–97.

Douglass, M. R., 2003. DMD reliability : a MEMS success story. Proceedings of Society of Photo-Optical Instrumentation Engineers 4980, 1–11.

Felippa, C. A., 1966. Refined Finite Element Analysis of Linear and Nonlinear Two-Dimensional Structures. Ph.D. thesis, Structures and Materials Research, Department of Civil Engineering, University of California, Berkley.

Furlani, E. P., 1999. Theory and simulation of viscous damped reflection phase gratings. Journal of Physics D: Applied Physics 32 (4), 412–416.

Furlani, E. P., Lee, E. H., Luo, H., 1998. Analysis of grating light valves with partial surface electrodes. Journal of Applied Physics 83 (2), 629–634.

Gilbert, J. R., Ananthasuresh, G. K., Senturia, S. D., 1996. 3D Modeling of Contact Problems and Hysteresis in Coupled Electro-Mechanics. Proceedings of the IEEE Micro Electro Mechanical Systems , 127–132.

He, Y., Marchetti, J., Gallegos, C., 1998. General Contact and Hysteresis Analysis of Multi-Dielectric MEMS Devices Under Thermal and Electrostatic Actuation. American Society of Mechanical Engineers, Dynamic Systems and Control Division (Publication) DSC 66, 323–328.

Hinton, E., Rock, T., Zienkiewicz, O. C., 1976. A Note on Mass Lumping and Related Processes in the Finite Element Method. Earthquake Engineering and Structural Dynamics 4, 145–249.

Hirota, G., Fisher, S., State, A., Lee, C., Fuchs, H., 2001. An Implicit Finite Element Method for Elastic Solids in Contact. pp. 136–146.

Horrigmoe, G., 1977. Finite Element Instability of Free-Form Shells. Ph.D. thesis, The University of Trondheim, Norway, Division of Structural Mechanics, The Norwegian Institute of Technology.

Horrigmoe, G., 1978. Hybrid Stress Finite Element Model for Non-Linear Shell Problems. International Journal for Numerical Methods in Engineering 12, 1819–1839.

Horrigmoe, G., Bergan, P. G., 1978. Nonlinear Analysis of Free-Form Shells by Flat Finite Elements. Computer Methods in Applied Mechanics and Engineering 16, 11–35.

Humar, J. L., 1990. Dynamics of Structures. Series in Civil and Engineering Mechanics. Prentice Hall International.

Jech, J. J., Lebens, J. A., Brazas, J. C. J., Kowarz, M. W., 2001. Method for producing optically planar surfaces for micro-electromechanical system devices. United States Patent US 6,426,237 B2.

Keating, D. J., Ho, L., 2001. Effects of Squeezed Film Damping on Dynamic Finite Element Analyses of MEMS. Proceedings of the SPIE 4408, 226–236.

Kowarz, M. W., 2001. Spatial light modulator with conformal grating device. United States Patent US 6,307,663.

Kowarz, M. W., Brazas, J. C. J., Phalen, J. G., 2002. Conformal Grating Electromechanical System (GEMS) for High-Speed Digital Light Modulation. IEEE 15th International Conference on Micro Electro Mechanical Systems Digest , 568–573.

Kurzweg, T. P., Martinez, J. A., Levitan, S. P., Davare, A. J., Kahrs, M., Chiarulli, D. M., 2003. System Simulation of a GLV Projection System. Vol. 4985 of MOEMS Display and Imaging Systems. SPIE, pp. 160–171.

Lund, J. L., Wise, K. D., 1994. Chip-Level Encapsulation of Implantable CMOS Microelectrode Arrays. Technical Digest Solid-State Sensor and Actuator Workshop , 29–32.

Madou, M., 1997. Fundamentals of Microfabrication. CRC Press LLC.

Meier, R. E., 1998. DMD Pixel Mechanics Simulation. Texas Instruments Technical Journal , 64–74.

Melosh, R. J., 1961. A stiffness matrix for the analysis of thin plates in bending. Journal of Aeronautical Sciences 38, 34–42.

Nabors, K., White, J., 1991. FastCap: A Multipole Accelerated 3-D Capacitance Extraction Program. IEEE Transactions on Computer Aided Design 10 (11), 1447–1459.

Naik, T., Longmire, E. K., Mantell, S. C., 2002. Dynamic response of a cantilever near a solid wall. Sensors and Actuators .

Newmark, N. M., 1959. A Method of Computation for Structural Dynamics. American Society of Civil Engineers Journal of Engineering Mechanics 85 (EM3), 67–94.

Oden, J. T., 1966. Calculation of Geometric Stiffness Matrices for Complex Structures. AIAA Journal 4 (8), 1480–1482.

Osterberg, P., Yie, H., Cai, J., White, J., Senturia, S., 1994a. Self-Consistent Simulation and Modeling of Electrostatically Deformed Diaphragms. Proceedings of the IEEE Micro Electro Mechanical Systems , 28–32.

Osterberg, P. M., Gupta, R. K., Gilbert, J. R., Senturia, S. D., 1994b. Quantative Models for the Measurement of Residual Stress, Poisson Ratio and Young's Modulus Using Electrostatic Pull-in of Beams and Diaphragms. Technical Digest Solid State Sensor and Actuator Workshop , 184–188.

Pian, T. H. H., 1972. Finite Element Methods by Variational Principles with Relaxed Continuity Requirement.

Rajasekaran, S., Murray, D. W., 1973. Incremental Finite Element Matrices. Journal of the Structural Division 99 (12), 2423–2438.

Senturia, S. D., Aluru, N., White, J., 1997. Simulating the Behaviour of MEMS Devices: Computational Methods and Needs. IEEE Computational Science and Engineering 1997 4 (1), 30–43.

Shames, I. H., Dym, C. L., 1991. Energy and Finite Element Methods in Structural Mechanics. Taylor & Francis.

Solgaard, O., 1992. Integrated Semiconductor Light Modulators for Fiber-Optic and Display Applications. Ph.D. thesis, Stanford University Electrical Engineering, Stanford CA94305.

Solgaard, O., Sandejas, F. S. A., Bloom, D. M., 1992. Deformable Grating Optical Modulator. Optics Letters 17 (9), 688–690.

Vemuri, S., Fedder, G. K., Mukherjee, T., 2000. Low-Order Squeeze Film Model for Simulation of MEMS Devices. Technical Proceedings of the MSM 2000 International Conference on Modeling and Simulation of Microsystems .

Younse, J. M., 1993. Mirrors on a chip. IEEE Spectrum 30 (11), 27–31.

Appendix A

ANSYS validation code

The appendix lists the ANSYS scripts used to run the modal and dynamic analysis verification tests.

A.1. Modeshapes and frequencies

```
!* ANSYS Modal analysis script
!* ANSYS V7.0
!* author : mark carey
!* date : 09/07/2003
!*
!* Preprocessor
/PREP7
!*
ET,1,shell181
!*
!*
R,1,0.11852357593195,0.11852357593195,0.11852357593195,0.11852357593195, , ,
RMORE, , , ,
RMORE
RMORE, ,
!*
!*
MPTEMP,,,,,,,,
MPTEMP,1,0
MPDATA,EX,1,,250000
MPDATA,PRXY,1,,0.33
MPTEMP,,,,,,,,
MPTEMP,1,0
MPDATA,DENS,1,,3.826242976843501E-15
BLC4,0,0,30,6
```

```
!* Specify the mesh density
!* 16 elements on the short edges of the model
LESIZE, 4, , ,16, , , , ,1
LESIZE, 2, , ,16, , , , ,1
!*
!* 64 elements on the long edges of the model
LESIZE, 1, , ,64, , , , ,1
LESIZE, 3, , ,64, , , , ,1
MSHAPE,0,2D
MSHKEY,0
AMESH, ALL
/UI,MESH,OFF
FINISH
/SOLU
!*
!* Constrain the ends of the model
!* select lines 2 and 4
LSEL,S,LINE,,2
LSEL,A,LINE,,4
!* select the nodes attached to the
!* selected lines
NSLL,S,1
!* fix the nodes we have selected
D,ALL,ALL,0
NSEL,ALL
!* apply the initial stress
PSTRESS,ON
ISTRESS,928.0853968087873,0,0,0,0,0,1
EMATWRITE,YES ! add this too
SOLVE
FINISH
!* this next part is straight out of the manual section
!* 3.12. Prestressed Modal Analysis of a Large Deflection Solution
/SOLU
ANTYPE,MODAL   !* Modal analysis
UPCOORD,1.0,ON !* Display mode shapes relative to deformed geometry
               !* in the postprocessor.
PSTRES,ON      !* Prestress effects ON
MODOPT,LANB,10 !* Select eigensolver
```

```
MXPAND,10      !* Specify the number of modes to expand, if desired.
PSOLVE, TRIANG !* Necessary for creating a proper .FULL file. See note
               !* below.
PSOLVE,EIGLANB !* Calculate the eigenvalues and eigenvectors.
               !* Use EIGLANB, EIGFULL, EIGUNSYM, or EIGDAMP to
               !* match MODOPT command.
FINISH
/SOLU          !Additional solution step for expansion.
EXPASS,ON
PSOLVE,EIGEXP  ! Expand the eigenvector solution. (Required if you
               ! want to review mode shapes in the postprocessor.)
FINISH
```

A.2. Dynamics

```
!* ANSYS Dynamic analysis script
!* ANSYS V7.0
!* author : mark carey
!* date : 09/07/2003
!*
!* Preprocessor
/CONFIG,NRES,2500
/PREP7
!*
ET,1,shell181        !* specify element type, SHELL181
!*
!* specify the nodal thicknesses for the SHELL181 element
R,1,0.11852357593195,0.11852357593195,0.11852357593195,0.11852357593195, , ,
RMORE, , , ,
RMORE
RMORE, ,
!*
!* specify the material properties, youngs modulus E, poisisons ratio nu and
!* density
MPTEMP,,,,,,,,
MPTEMP,1,0
MPDATA,EX,1,,250000
MPDATA,PRXY,1,,0.33
MPTEMP,,,,,,,,
```

```
MPTEMP,1,0
MPDATA,DENS,1,,3.826242976843501E-15
!*
!*
!* Draw a rectangular area representing the ribbon
BLC4,0,0,15,3   !* quarter model
!*
!* Specify the mesh density
!* 16 elements on the short edges of the model
LESIZE, 4, , , 8, , , , ,1
LESIZE, 2, , , 8, , , , ,1
!*
!* 64 elements on the long edges of the model
LESIZE, 1, , ,32, , , , ,1
LESIZE, 3, , ,32, , , , ,1
!*
!* Mesh the area
MSHAPE,0,2D
MSHKEY,0
AMESH, ALL
/UI,MESH,OFF
FINISH
!*
/SOLU !* enter the solution step
!*
!* Constrain the ends of the model
LSEL,S,LINE,,4
NSLL,S,1
D,ALL,ALL,0
!* Apply symmetry constraints
LSEL,S,LINE,,3
NSLL,S,1
D,ALL,UY,0
D,ALL,ROTX,0
!* Mid point
LSEL,S,LINE,,2
NSLL,S,1
D,ALL,UX,0
D,ALL,ROTY,0
```

```
!* select all nodes
NSEL,ALL
!*
/SOLUTION
ANTYPE,4
!*
!* Full Transient Analysis
TRNOPT,FULL
!* No Mass lumping
LUMPM,0
!*
DELTIM,2.8E-9,0,0  !* Initial timestep
OUTRES,ALL,ALL
AUTOTS,0           !* Disable auto timestepping
!*
!* rayleigh damping parameters
ALPHAD,4.333175700254638E6   !* alpha
BETAD,3.637686431429612E-10  !* beta
!*
TIMINT,OFF         !* time integration off
TIME,0             !* start the solution
LSWRITE            !* write step one
!*
!*
TIMINT,ON          !* Enable time integration
KBC,0              !* Interpolated loads (Ramp)
TINTP,'',0.25,0.5  !* Newmark control parameters, constant average acceleration
!*
!* Apply loads, to the centerline nodes
NSEL,S,LOC,X,15,15   !* select nodes at the structure centerline
NSEL,R,LOC,Y,0,2.99  !* exclude the y center line node
F,ALL,FZ,-0.00275
NSEL,S,LOC,X,15,15
NSEL,R,LOC,Y,2.99,3
F,ALL,FZ,-0.001375
NSEL,ALL
!*
TIME,2.8E-6     !* 1000 time steps after the start of the simulation
LSWRITE         !* write step 2
```

```
!*
NSEL,S,LOC,X,15,15   !* select nodes at the structure centerline (x = 15)
F,ALL,FZ,0           !* set applied force to zero removing the applied load
NSEL,ALL
TIME,2.8028E-6
LSWRITE              !* write step 3
!*
TIME, 5.6028E-6
LSWRITE              !* write step 4
!* Solve transient analyis from load step files
LSSOLVE,1,4,1,
```

Appendix B

Simulation Process

B.1. Simulation process

B.1.1. Running a simulation

Running a simulation requires a setup (`setup_sim_base.m`) file describing the simulation in terms of the internal data structures for the analysis code. A simulation file is then required (`base_sim.m`) which uses the data structures and starts the numerical marching procedure.

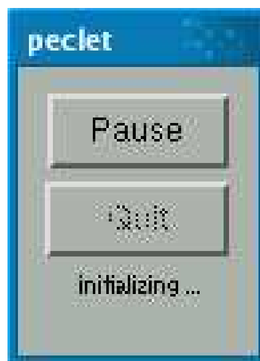

Figure B.1. Simulation control dialog

A small simulation control dialog will appear (Figure B.1), depressing the pause button, pauses the simulation and allows the computer to be used for another task, releasing the pause button and typing `‘‘return’’` in the matlab command window resumes the simulation. The dialog is designed to function in an X11 environment, where a single x-server displays output from multiple x-clients, thus the titlebar of the dialog displays the hostname of the x-client on which the simulation is running, “peclet” in Figure B.1. If matlab has to be closed, pausing the simulation will enable the exit button allowing matlab to be shutdown. The simulation can be resumed at a later date using the `iterate.m`

function.

If a simulation should ever fail to attain electrostatic equilibrium, the single most probable cause is the base time step is too great. Reducing the base time step size (`struct_step.root_size`) and restarting the analysis should allow the solution to complete.

B.2. Analysing results

Using the results files from completed simulations to produce usable output

B.2.1. Information

To extract the bifurcation voltages, times and step information from a simulation the function `mbw_vpd_and_vrl.m` is used. `mbw_find_substrate_contact.m` calculates the number of nodes that come into contact with the oxide layer during a given simulation, the output from this function can be used to gather the data required for plotting the number of oxide layer contacted nodes, i.e. the black dashed line in Figure 5.28(c).

B.2.2. Plots

Plotting the electromechanical hysteresis behaviour of the GEMS ribbon unit (Figures 5.3, 5.8, 5.12, 5.15, 5.20, 5.24 and 5.27) is achieved using the function `mbw_hysteresis.m`, where the names and paths of a number of simulation block files are supplied with a point of interest.

Plotting the mesh configuration (Figures 5.2, 5.16, 5.18 and 5.22) is achieved using the form of `plot_ribbon_and_standoffs.m` in which a deformed mesh configuration is supplied. `plot_node_numbering.m` can be used to append node numbering information to a plot of the deformed ribbon unit as in Figure 5.2.

B.2.3. Movies

Movies are created using `mbw_animate_ribbon.m` which produces a directory (*ppmmovie*) full of portable pixmap files (*.ppm*) files. Using the unix utility `mpeg_encode` the *.ppm* files can be converted to an MPEG format movie. Compression of the movie is achieved using `mencoder`, part of the `mplayer` family of tools.

Appendix C

Simulation runtimes

The simulations in Chapter 5 were run on intel hardware running a variety of operating systems in various versions of Matlab. Operating systems used GNU/Linux - RedHat 8.0 & 7.1, Microsoft Windows - 2000 & XP.

All machines contained a minimum of 512MB of physical memory (RAM), and excessive amounts of free disk space. This memory limit restricted the maximum number of steps that could be stored in a block without the running out of system memory, in the simulations where more than 4000 steps per block were used the machine had more physical memory available. Note that the simulation process in not memory intensive, the function `simulate.m` only requires information about the current and previous step in order to operate. A block size of two steps is possible, but suboptimal.

Table C.1 lists the computational requirements of all simulations successfully completed. The total size of the data set is 105GB and required 76 days of computer time to produce.

Table C.1. Simulation computational requirements

Case	Mesh	Number of Blocks	Disk (GB)	Time (HH:MM)
Reference				
	16x68	8	2.53	49:12
	08x34	1	0.07	00:41
Slew Rate				
300ns	16x68	2	0.49	08:08
200ns	16x68	3	0.8	18:43
100ns	16x68	3	0.79	12:56
50ns	16x68	2	0.48	19:57
20ns	16x68	3	0.78	12:50
Initial Material Stress (σ_0)				
962 (87.5%)	16x68	18	5.05	79:00
825 (75%)	16x68	20	5.84	93:20
550 (50%)	16x68	21	5.93	163:06
0 (0%)	16x68	50	14.39	243:07
Thickness ($t_{Si_3N_4}$)				
0.90µm (90%)	16x68	17	4.88	123:55
0.80µm (80%)	16x68	19	5.26	85:36
0.70µm (70%)	16x68	21	5.94	98:19
0.50µm (50%)	16x68	24	6.67	123:21
Standoff Layout (s_y)				
0µm or $>$ 4.5µm	16x68	9	3.04	58:14
1.5µm	16x68	16	4.6	56:43
2µm	16x68	15	4.22	51:57
3.5µm	16x68	14	3.99	56:40
Standoff Layout (s_x)				
6µm	16x68	10	2.81	40:01
8µm	16x68	20	5.76	95:50
Standoff Height ($t_{Standoff}$)				
0.04µm (80%)	16x68	14	4.75	116:08
0.03µm (60%)	16x68	25	6.98	111:12
0.02µm (40%)	16x68	28	8.09	105:56
Totals			104.15	1824:53